STUDIES ON CAVITATION EROSION RESISTANCE OF REACTOR MATERIALS

By

B.K. SREEDHAR

Enrollment Number ENGG02200904004

Indira Gandhi Centre for Atomic Research, Kalpakkam

A thesis submitted to the

Board of Studies in Engineering Sciences

In partial fulfillment of requirements

for the Degree of

DOCTOR OF PHILOSOPHY

of

HOMI BHABHA NATIONAL INSTITUTE

August, 2016

Homi Bhabha National Institute

Recommendations of the Viva Voce Committee

As members of the Viva Voce Committee, we certify that we have read the dissertation prepared by B.K. SREEDHAR entitled "STUDIES ON CAVITATION EROSION RESISTANCE OF REACTOR MATERIALS" and recommend that it may be accepted as fulfilling the thesis requirement for the award of Degree of Doctor of Philosophy.

Chairman - Dr. U. Kamachi Mudali	**Date:** 30/3/17
Guide / Convener - Dr. Shaju K. Albert	**Date:** 30/3/17
Co-guide - Prof. A.B. Pandit	**Date:** 30/3/2017
Examiner - Prof. Satish Vasu Kailas	**Date:** 30/03/17
Member 1- Dr. A.K. Bhaduri	**Date:** 30/3/2017
Member 2- Dr. Saroja Saibaba	**Date:** 30/03/2017

Final approval and acceptance of this thesis is contingent upon the candidate's submission of the final copies of the thesis to HBNI.

I/We hereby certify that I/we have read this thesis prepared under my/our direction and recommend that it may be accepted as fulfilling the thesis requirement.

Date: 30/3/17 **Place:** Kalpakkam

<Signature> **Co-guide** (if applicable)

<Signature> **Guide**

STATEMENT BY AUTHOR

This dissertation has been submitted in partial fulfillment of requirements for an advanced degree at Homi Bhabha National Institute (HBNI) and is deposited in the Library to be made available to borrowers under rules of the HBNI.

Brief quotations from this dissertation are allowable without special permission, provided that accurate acknowledgement of source is made. Requests for permission for extended quotation from or reproduction of this manuscript in whole or in part may be granted by the Competent Authority of HBNI when in his or her judgment the proposed use of the material is in the interests of scholarship. In all other instances, however, permission must be obtained from the author.

B.K. SREEDHAR

DECLARATION

I, hereby declare that the investigation presented in the thesis has been carried out by me. The work is original and has not been submitted earlier as a whole or in part for a degree / diploma at this or any other Institution / University.

B.K. SREEDHAR

List of Publications arising from the thesis

Journal

1. B.K Sreedhar, S.K. Albert and A.B Pandit, Cavitation Erosion Testing of Austenitic Stainless Steel (316L) in Liquid Sodium, Wear 328-329 (2015) 436-442.
2. B.K Sreedhar, S.K. Albert and A.B Pandit, Improving Cavitation Erosion Resistance of Austenitic Stainless Steel in Liquid Sodium By Hardfacing – Comparison of Ni and Co Based Deposits, Wear 342-343 (2015) 92-99.
3. B.K Sreedhar, S.K. Albert and A.B Pandit, Cavitation Damage : Theory and Measurements – A Review, Wear 372-373 (2017) 177-196
4. B.K Sreedhar, Shaju K. Albert, A.B Pandit, Computation of erosion potential of cavitation bubble in an ultrasonic pressure field, submitted to Journal of Pure & Applied Ultrasonics.
5. B.K Sreedhar, N. Chakraborty, Shaju K Albert, A.B Pandit, Design and analysis of ultrasonic horn for cavitation generation in liquid sodium, submitted to Journal of Pure & Applied Ultrasonics.

Conference

1. B.K Sreedhar, Shaju K. Albert, A.B Pandit, Computation of erosion potential of cavitation bubble in an ultrasonic pressure field, XXIst National Symposium on Ultrasonics (NSU 2016), S. N. Bose National Centre for Basic Sciences, Kolkata, 08-10 November, 2016.
2. B.K Sreedhar, N. Chakraborty, Shaju K Albert, A.B Pandit, Design and analysis of ultrasonic horn for cavitation generation in liquid sodium, XXIst National Symposium on Ultrasonics (NSU 2016), S. N. Bose National Centre for Basic Sciences, Kolkata, 08-10 November, 2016.

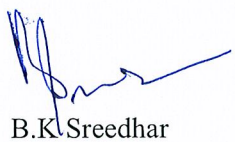

B.K Sreedhar

To the memory of my parents

We dance round in a ring and suppose,
But the Secret sits in the middle and knows.
(Robert Frost, The Secret Sits)

ACKNOWLEDGEMENTS

This thesis would have remained a mirage without the unstinted support and encouragement of my guide Dr. Shaju K. Albert, Head, Materials Technology Division (MTD), Materials and Metallurgy Group, IGCAR. He helped me in a myriad different ways, right from making available the hard faced raw material to extending the examination facilities with him for my use. He was always available for technical discussions albeit his busy schedule and during the preparation of the thesis he spent many late hours poring over the multiple drafts with the discerning eye of a professional copy editor. I place on record my profound sense of gratitude to him.

I also thank my co-guide Prof. A.B Pandit, Dept. of Chemical Engineering, Institute of Chemical Technology (ICT), Mumbai, for his insightful comments and constructive feedback during the course of the work.

I thank Dr. U. Kamachi Mudali, Chairman, Doctoral Committee and the members of the committee, Dr. A.K Bhaduri and Dr. Saroja Saibaba, for their thoughtful suggestions during the progress reviews.

I am grateful to Dr. G. Vaidyanathan and Dr. P. Kalyanasundaram, former directors of Fast Reactor Technology Group (FRTG), for granting permission for the work. Dr. P. Kalyanasundaram provided ungrudging support to establish the cavitation erosion test facility and for this I am indebted to him. I thank Dr. K.K Rajan, former director of FRTG, and Shri. P. Selvaraj, present Director, FRTG, for providing support for the work.

I thank Shri. G. Padmakumar, Head, Sodium Experiments and Hydraulic Division, for his support during the course of the work.

I express my gratitude to my section colleagues, S.Shri. P. Madan Kumar, N. Chakraborty, S.I Sundarraj, Anant kumar, Rakesh Mourya, R. Nirmal kumar, A. Kolanjiappan and to Shri. S.P Ruhela, Chemical Technology Division, for their support and assistance in the course of the work.

I thank Shri P. Chandramouli, Head, Rig Operation Section, and his colleagues S.Shri C. Adikesavan (retd.), R. Shanmugam (retd.), M.T Janakiraman (retd.) and C. Rajappan for their assistance during the experiments; Shri. G. Vijayakumar, Head, Electrical Services Section, and his colleagues S.Shri. R. Rajendra Prasad and R. Iyappan for electrical systems support; and Smt. J.I Sylvia, Head, Rig Instrumentation Section, and her colleagues S.Shri. P. Vijayamohana Rao and V. Krishnamurthy for instrumentation systems support

I also thank Smt. N. Sreevidya, MTD, for her assistance in the SEM analysis and Shri. Utpal Borah, Head, Metal Forming and Tribology Section, MTD, and his colleague Shri. Arvinth Davinci for their assistance in roughness measurements.

Last but not the least I thank my brother for his motivation throughout the work.

SYNOPSIS

Cavitation is a phenomenon which occurs in liquid systems when the static pressure at any point in the system falls below the vapor pressure at constant system temperature. It is therefore the process of boiling in the liquid due to pressure reduction rather than heat addition. In a flowing system the pressure reduction can occur due to hydrodynamic effect and the resultant two phase flow is known as cavitating flow. The vapor bubbles thus formed, in the regions of minimum pressure, are carried by the flowing liquid to eventually collapse in regions where the pressure recovers and exceeds the vapor pressure. The collapse can result in noise and vibrations and can lead to severe damage of the metal surface if the collapse occurs adjacent to the metal surface. In hydraulic machinery this results in performance degradation and component damage. It is therefore the goal of every designer to avoid cavitation during the expected range of operation of the equipment. However, in the case of complex and capital intensive engineering systems like a nuclear reactor it is not always possible to avoid cavitation altogether during normal operation from economic considerations.

This work is devoted to the study of cavitation erosion produced in reactor materials in liquid sodium environment with specific reference to austenitic stainless steel SS 316L and its hard faced variants, viz. hard faced with Stellite6 and Colmonoy5.

The thesis is divided into five chapters. The first chapter begins with an introduction to the phenomenon of cavitation in liquids, its insidious effects and the challenge posed in avoiding cavitation altogether. This is followed by a brief

description of a fast reactor where liquid sodium is used as the primary and secondary coolant. The major materials used in the hot and cold legs of fast reactors worldwide are then discussed The cavitation susceptible regions in a fast reactor with examples of damage caused due to cavitation are highlighted and the need for a detailed study of cavitation damage in liquid sodium is justified. This is followed by a discussion on cavitation damage observed in various fast reactors. The chapter concludes with a discussion on methods (related to materials) by which cavitation damage can be mitigated, such as hard facing (using Co based alloys (eg. Stellite) and Ni based alloys (Colmonoy)) and surface treatment methods such as thermal spray coating.

Chapter 2 is an exhaustive literature survey on work done in the area of cavitation damage. The chapter reviews the work done in the area of theoretical and experimental estimation of bubble collapse pressure, the liquid and material parameters influencing cavitation damage, the work done in the area of cavitation damage modeling and the experimental methods & facilities available for cavitation damage measurement. The chapter begins with a discussion on the basic theory of bubble collapse and covers the various governing equations of single bubble collapse and their limitations, the liquid properties affecting cavitation damage and the theoretical and experimental work done in the estimation of single bubble collapse pressure. The chapter also discusses the laboratory techniques for cavitation damage measurement, the facilities available for measurement of cavitation damage in liquid metals (sodium) and the instrumentation employed in water and sodium for measurement of bubble collapse pressure. The section on predicting cavitation damage from material properties covers the various models used for damage

estimation. The chapter concludes with a review of cavitation damage studies done so far in liquid metals.

Chapter 3 covers the numerical estimation of single bubble collapse pressure. The chapter begins with a quick derivation of the Rayleigh Plesset Noltingk Neppiras Poritsky (RPNNP), discusses the limitations of the equation and then moves on to the Gilmore equation which is capable of handling liquid compressibility experienced in the final stages of bubble collapse. Both RPNNP and Gilmore equations are solved using the 4^{th} order Runge Kutta (RK) method and the results verified using benchmark problems. A comparison is made between the results of RPNNP equation (incompressible liquid) and Gilmore equation (taking into account the effect of compressibility) as well as between the magnitudes of single bubble collapse pressure in water and in sodium. There is a large difference between the jet velocities produced at the end of collapse in water and in sodium resulting in an appreciable difference between the water hammer pressures resulting from the impingement of the jet with the surface. This large difference between the water hammer pressures underlines the need for tests in sodium, rather than in water, to determine the damage resistance of materials.

Chapter 4 discusses the vibratory cavitation sodium test facility installed in Hall III, FRTG. A detailed description of the test facility and its components, the preheating system, and the instrumentation employed is provided. Design of the mechanical components and the cooling arrangement for the top flange portion of the vessel are also discussed. Also provided are details of the test specimens (eg. chemical composition, dimensions, hardness etc.), preparation of specimens (eg. surface finish achieved before start of experiment, weight etc.), hard facing procedure

and details of purity of sodium in the loop. The experimental procedure including that for cleaning and inspection of the sample, pre-commissioning tests and various methods used for inspection of the specimens after testing are also discussed

Chapter 5 begins with the estimation of the overall error in the experiments. The raw data (eg. temperature of sodium, test duration, test pressure, weight of sample before and after experiment etc.) are provided in Annexure 1. The results of weight loss experiments (cumulative weight loss vs time and cumulative weight loss rate vs time) with SS316L, Colmonoy5 and Stellite6, in sodium at various temperatures (200°C, 250°C, 300°C and 400°C) are compared and explained in terms of material fracture toughness and stacking fault energy. Visual and SEM images of the three types of specimens are also discussed. The results of roughness measurements on selected samples of each of the types tested are also discussed.

Chapter 6 concludes the thesis with a summary of the results obtained and directions for further work in this area.

LIST OF FIGURES

CHAPTER 5

LIST OF TABLES

APPENDIX 2

NOMENCLATURE

A	Area of specimen face, mm^2
A_o	Membrane surface area of a reference sensor, mm^2
a_c	Projected radius, mm
B	Bulk modulus, N/m^2
B_{eff}	Dimensionless
b	Fatigue strength exponent
C	Velocity of sound, m/s / Local velocity of sound in the liquid, m/s
C_0	Absolute velocity of sound in the liquid, m/s
C_1, C_2, C_3, C_4	Material dependant constants
c_L	Specific heat of the liquid, J/kg-K (BTU/lbm-$^\circ$F)
D	pit diameter, μ
D*	Characteristic pit equivalent diameter
D	Diameter of the cavitation pit, μ
d	mean depth of erosion (MDE)
E	Elasticity modulus, N/m^2
ETT	Erosion threshold time, s
F	Material factor = $HV_{\text{after erosion test}} / HV_{\text{before erosion test}}$
H	Liquid enthalpy, J/kg / depth of the sample, μ
HV	Vicker's hardness
h	Depth of the cavitation pit, μ / depth of strain hardening, μ / enthalpy difference between the liquid at pressure P and the liquid at pressure P_∞

h_{max}	maximum depth of the pit, μ.
Δh_f	enthalpy increase corresponding to a reduction in pressure below saturation conditions, J/kg (BTU/lbm)
I	Intensity of cavitation
J	density of energy flux delivered to the material by the collapsing bubbles
Kc	Fracture toughness of the material, MPa √ m
k_L	Thermal conductivity of the liquid, J/s-m-K (BTU/hr-ft-°F)
K_L	Thermal diffusivity of the liquid m^2/s (ft^2/hr)
k	Shape factor of the Weibull curve
L	Latent heat of vaporization of the liquid, J/kg (BTU/lbm)
L	Depth of work hardening / maximum thickness of the hardened layer, μ
l	Depth of the hardened layer
MDE	Mean depth of erosion, μm
MDPR	Mean depth of penetration rate, μm/hr
N	Number of pits of diameter D per unit area per sec
N	Total number of pulses
N^*	Characteristic number of pits per unit area per sec / Normalizing parameter for the cumulative number of peaks
N(p)	Cumulative number of peaks with peak height larger than pressure P
2N	Number of load reversals to failure
NPSHA	Net positive suction head available, m
$NPSHR_{3\%}$	Net positive suction head required for 3% head drop, m
n_i	Number of pressure pulses of peak value p_i in unit time

n	Coefficient of work hardening
P	Pressure at infinity driving collapse, N/m^2
P’	Instantaneous pressure on solid surface, N/m^2
P*	Normalizing parameter for peak height
P_a	Acoustic amplitude, N/m^2
P_{atm}	Atmospheric ressure, N/m^2
P_{vp}	Vapor pressure, N/m^2
P_∞	Pressure at infinity driving collapse, N/m^2
P_{g0}	Initial pressure inside the bubble, N/m^2
P_g	Pressure of vapor and gas inside the bubble, N/m^2
P_L	Pressure in the liquid, N/m^2
p_1	Jet upstream pressure
ΔP	Reduction in pressure, N/m^2 (lb/ft^2)
Q	Initial pressure inside the bubble, N/m^2
R	Bubble radius, mm / Radius of cavitation pit, μ / Pit radius, μ / End radius of spherical tip, mm
R_0	Initial bubble radius, mm
r_e	Radius of plastic zone, μ
SE	Strain energy, N/m^2
ΔT	Reduction in temperature in liquid film due to vaporization, K (°F)
t	Time, s / exposure time, s
t_{inc}	Incubation time, s
t_{vmax}	time at which maximum volume loss rate occurs

U	Bubble wall velocity = $\frac{dR}{dt}$ / local liquid velocity, m/s
UR	Ultimate resilience, N/m^2
UTS	Ultimate tensile strength, N/m^2
u	volume loss rate, mm^3/h
V_L	Volume of liquid, m^3
V_V	Volume of vapor, m^3
v_L	Specific volume of liquid, kg/m^3
v_V	Specific volume of vapor, kg/m^3
v_{max}	Maximum volume loss rate, mm^3/s
ΔV	volume of material eroded, mm^3
V(t)	Cumulative volume loss, mm^3
dV/dt	cumulative volume loss rate, mm^3/s
W_{pl}	Relative work of plastic deformation on the surface

Greek Symbols

α	Multiplication factor in pit number per unit time (representing the increase of pitting rate), h^{-1}
β	Coefficient of compressibility / shape factor or slope of the Weibull line / Factor representing the annihilation of pit number per unit time , $1/\mu$
ε	Strain / ultimate elongation
$\varepsilon(x)$	Strain at distance x from the surface
ε_z	surface strain at the point of impact
ε_r	Rupture strain

ε_0	Permanent strain
$\Delta\varepsilon_\varepsilon$	Elastic strain amplitude
γ	Gas expansion / compression index
η	scale factor or characteristic time, i.e ETT
θ	Power of work hardening / shape factor of the strain profile
μ	Liquid viscosity, N-s/m^2
ρ	Liquid density, kg/m^3
ρ_L	density of liquid, kg/m^3 (lbm/ft^3)
ρ_V	density of vapor, kg/m^3 (lbm/ft^3)
σ	Surface tension, N/m / Elastic limit, N/m^2 / Proof stress, N/m^2
σ_0	Reference stress corresponding to permanent strain ε_0
σ_{YS}	Yield stress, N/m^2
σ_{ULT}	Ultimate tensile strength, N/m^2
σ_a	Alternating stress amplitude, N/m^2
σ_f ‘	Fatigue strength coefficient
σ_e	Proof stress, N/m^2
σ_R	Rupture stress, N/m^2
τ	Average cavitation pulse duration, s

CONTENTS

CONTENTS

CHAPTER 1

INTRODUCTION

CHAPTER 1 - INTRODUCTION

1.0 INTRODUCTION

Cavitation is a phenomenon which occurs in liquid systems when the static pressure at any point in the system falls below the vapor pressure at constant system temperature. It is therefore the process of boiling in the liquid due to pressure reduction rather than heat addition. In a flowing system the pressure reduction can occur due to hydrodynamic effect and the resultant two phase flow is known as cavitating flow. The vapor bubbles thus formed, in the regions of minimum pressure, are carried by the flowing liquid to eventually collapse in regions where the pressure recovers and exceeds the vapor pressure. The collapse can result in noise and vibrations and can lead to severe damage of the metal surface if the collapse occurs adjacent to the metal surface. In hydraulic machinery this results in performance degradation and component damage. It is therefore the goal of every designer to avoid cavitation during the expected range of operation of the equipment. However, in the case of complex and capital intensive engineering systems like a nuclear reactor it is not always possible to avoid cavitation altogether during normal operation from economic considerations.

Operation with limited cavitation, while not conspicuously affecting pump performance parameters such as head, flow and efficiency, can result in damage in the long run. For eg., in pumps the parameter used conventionally as a measure of cavitation performance is $NPSHR_{3\%}$ i.e. the Net Positive Suction Head Required at which 3% head drop is detected and normally the NPSHA (Net Positive Suction Head Available) is $k*NPSHR_{3\%}$ where k is a safety margin (normally 1.5-2). The inception of cavitation usually occurs at much higher values (due to

dissolved gases and fluid turbulence) of NPSHA and it is seen that operation with a margin as high as 4 may be required to ensure damage free performance [1]. Providing such a high margin, especially in a nuclear reactor, will necessarily make the system capital intensive and uneconomical and therefore means to achieve cavitation tolerant operation through judicious material selection and improved hydraulic design assume importance.

Systematic studies on cavitation damage are therefore important to obtain valuable basic and applied data of direct use.

1.1 DESCRIPTION OF PROTOTYPE FAST BREEDER REACTOR (PFBR) [2]

The prototype fast breeder reactor (PFBR) is a sodium cooled, pool type, mixed oxide fuelled reactor. The main objective of the reactor is to demonstrate the techno-economic viability of FBR's on an industrial scale. Fig. 1 is the schematic of the PFBR showing the main vessel and reactor core (primary loop), the secondary sodium loop and the tertiary steam-water loop.

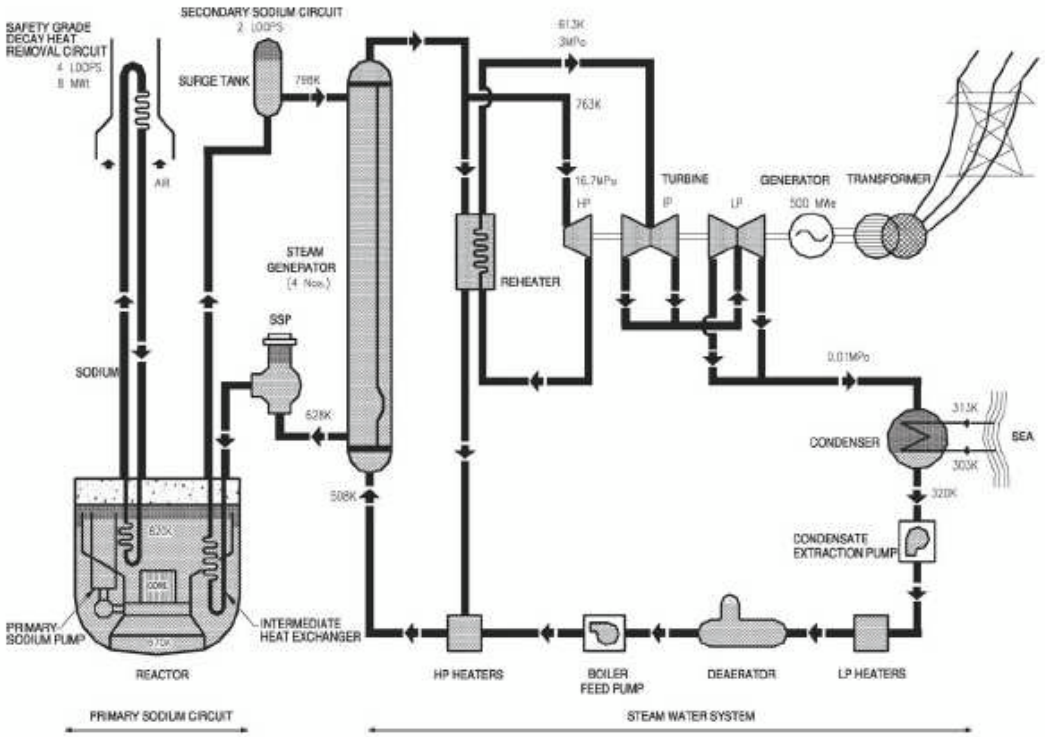

Fig. 1.1 – Schematic of PFBR

The primary loop consists of the reactor core, the hot sodium pool, the intermediate heat exchangers (IHX), the primary centrifugal coolant pump and the cold sodium pool. The hot and cold sodium pools are separated by an inner vessel or 'redan'. The primary pumps are located in the cold sodium pool 670 K (397 ºC) and the temperature of sodium at the reactor outlet is 820K (547 ºC).

The heat generated in the core is extracted by circulating liquid sodium through the core using primary coolant pumps. There are two primary loops each consisting of one primary pump and two IHX's.

The hot sodium in the primary pool transfers the heat to the sodium in the secondary circuit in the IHX's.

There are two secondary circuits each consisting of one centrifugal sodium pump, two IHX's and four steam generators. Heat extracted by the secondary sodium is transferred to water, in the tertiary steam-water circuit, in the steam generator to produce steam which is used to drive the turbine to produce power.

1.2 STRUCTURAL MATERIALS USED IN FAST REACTORS

Low alloy steels are not considered for fabrication of components in the primary heat transport system because they do not possess adequate mechanical properties. Stainless steel is therefore used. Among the stainless steels, (a) Ferritic stainless steel is not used because of (i) inadequate high temperature mechanical properties (ii) susceptibility to embrittlement at 475°C (iii) susceptibility to sigma phase embrittlement at high temperature, and (iv) difficulties experienced during welding due to grain coarsening. (b) Martensitic stainless steel is not used because of (i) notch sensitivity (ii) low ductility, and (iii) embrittlement between 420°C and 550°C. Austenitic stainless steel is therefore used as the major structural material. It has (i) adequate mechanical properties (ii) is compatible with liquid sodium (iii) has good weldability and irradiation resistance, and (iv) has good availability of design data because of its vast operating experience as fast reactor structural material. Monometallic construction is preferred in sodium systems to avoid interstitial element transfer (eg. of carbon) through liquid sodium due to differences in thermodynamic activity in a bimetallic system. Hence austenitic stainless steels are employed in the entire system. Table 1 lists the structural materials used in fast reactors **[3].**

Table 1.1 - Materials used in FBRs for major components [3]

Reactor	Country	Reactor Vessel	IHX	Primary Circuit Piping Hot leg (cold leg)#	Secondary Circuit Piping Hot leg (cold leg)
Rapsodie	France	316 SS	316 SS	316 SS (316 SS)	316 SS (316 SS)
Phenix	France	316L SS	316 SS	(316 SS)	321 SS (304 SS)
PFR	U.K.	321 SS	316 SS	(321 SS)	321 SS (321 SS)
JOYO	Japan	304 SS	304 SS	304 SS (304 SS)	2.25Cr-1Mo (2.25Cr-1Mo)
FBTR	India	316 SS	316 SS	316 SS (316 SS)	316 SS (316 SS)
BN-600	Russia	304 SS	304 SS	304 SS	304 SS (304 SS)
Super Phenix-1	France	316L(N) SS	316L(N) SS	(304L(N) SS)	316 L(N) SS
FFTF	U.S.A.	304 SS	304 SS	316 SS (316 SS)	316 SS (304 SS)
MONJU	Japan	304 SS	304 SS	304 SS (304 SS)	304 SS (304 SS)
SNR-300	Germany	304 SS	304 SS	304 SS (304 SS)	304 SS (304 SS)
BN-800	Russia	304 SS	304 SS	304 SS	304 SS (304 SS)
CRBRP	U.S.A.	304 SS	304 and 316 SS	316 SS (304 SS)	316H (304H)
DFBR	Japan	316FR SS	316 FR	316FR (304 SS)	304 SS (304 SS)
EFR	Europe	316L(N) SS	316L(N) SS	316L(N) SS	316L(N) SS

for pool-type reactor, there is no hot leg piping

1.3 RELEVANCE OF CAVITATION DAMAGE STUDIES IN SODIUM

In a fast neutron reactor liquid sodium is used as the primary and secondary coolant because (i) it is non-moderating (ii) has excellent heat transfer properties, and (iii) it requires relatively low pumping power compared to other coolant candidates.

The areas in a fast neutron reactor where the possibility of cavitation exists are suction face of the impeller of coolant (primary / secondary) pumps , foot of core sub assemblies, fluid film bearings etc.

Cavitation can occur on the suction face of pump impeller blades when the available NPSH is less than that required (classical cavitation). Cavitation can also occur in regions where high velocities exist such as impeller outlet, diffuser, impeller wearing ring etc. Cavitation damage has been observed in the impellers of the BN-350 primary and secondary coolant pumps and the BN-600 primary pump. The severity of the problem may be appreciated from the dimensions (150 mm in length, 70 mm in breadth and 18 mm in depth) of the damaged region on the BN 600 primary pump impeller [4]. Fig. 2 is a representative photo [5] showing the cavitation susceptible areas on the suction face of a pump impeller. The impeller in the photograph was subjected to cavitation testing (paint erosion test) and the areas on the blade suction face where paint is removed are the regions where bubble collapse has occurred.

Fig. 1.2 – Cavitation susceptible areas on a pump impeller [3]

The reactor core consists of fuel, blanket, reflector, shielding, control and storage subassemblies. The power generated by each of these sub assembly types is different and therefore the flow rate through the sub assemblies is regulated by means of orifices provided at

the foot of the sub assemblies (flow zoning) thereby ensuring a uniform temperature distribution across the core exit. In addition to this, labyrinths (top and bottom) are provided at the sub assembly foot to reduce the leakage between the sub assembly and the grid plate. Cavitation can occur downstream of these devices (orifice and labyrinth) if the pressure drops across these are high and therefore extensive efforts are expended in the development of the same. Cavitation can also occur in the seating surfaces of the sub assemblies on the grid plate when there is marginal lifting of the sub assembly (due to bending, handling etc.) resulting in small gaps (< 1.5 mm) at the bearing surfaces. Although cavitation was not a problem in the Rapsodie plant, difficulties due to cavitation were experienced during the development of flow control orifices and in the seating surface of sub assembly on the grid plate in both Phenix and Super Phenix plants [6]. In the Enrico Fermi atomic power plant erosion type damage was observed in some of the sub assembly seating surfaces in the lower support plate during inspection after pre-operational tests but before criticality. This was attributed to local high velocities resulting in cavitation due to improper seating of the sub assembly nozzles in the support plate holes. All the holes in the lower support plate were then modified with Stellite inserts and no erosion of the inserts was observed during a later inspection [7].

The rotor assemblies of reactor coolant pumps are supported in sodium using hydrostatic bearings. The bearings are fed with high pressure sodium from the pump outlet and their load capacity is proportional to the pump head (square of the pump speed). Cavitation in fluid film bearings [8] can possibly occur when the driving head is low (low pump speed operation) or due to entrainment of gas in the pumped liquid.

Cavitation damage can be avoided by (a) proper material selection (b) optimizing the hydraulic design to delay cavitation inception, and (c) by using protective coating or surface

treatment of the material to increase its resistance to cavitation erosion. While model testing can be used to validate improvements in design, experimental study of cavitation damage is invaluable to evaluate material performance / efficacy of hard facing treatment vis-a-vis resistance to cavitation erosion.

1.4 HARD FACING AND SURFACE TREATMENT METHODS TO IMPROVE CAVITATION RESISTANCE

A study of cavitation erosion literature reveals that several hardfacing / surface treatment techniques are being studied to improve resistance to cavitation erosion. These include hardfacing (using Stellite [9], Colmonoy [10]), hard chrome plating [11], metal plating [12], coatings (nanocrystalline TiN [13], Cr-N [14], etc.), surface treatment methods [15, 16] and laser surface modification [17] . In fast reactors, Colmonoy and Stellite are commonly used for hard facing components.

Stellite6 is a cobalt based alloy with 27%Cr, 2.5%Ni, 0.08%W and 1%C. Its microstructure consisting of Co rich matrix phase dendrites with interdendritic Cr rich carbides provides the alloy with the hardness to resist cavitation damage. On irradiation in the reactor, the stable isotope Co^{59} is transmuted to radioactive Co^{60}. The isotope Co^{60} emits γ radiation of 1.17 MeV and 1.33 MeV energy with a half life of 5.3 years. It therefore poses problems during maintenance and repair of hardfaced components.

Colmonoy5 is a Nickel based alloy with 11.5% Cr, 3.75% Si, 2.5% Boron and 0.65% Carbon. It contains high volume fraction of interdendrite carbides, borides, silicides along with eutectic lamella of borides/silicides/Ni phase and relatively soft Ni/phase dendrites. The hard interdendrite phases provide it with high resistance to wear. It does not become active under

irradiation and is therefore preferred for hardfacing nuclear reactor components especially those that require regular maintenance.

Therefore, the Indian Prototype Fast Breeder Reactor (PFBR) uses Colmonoy as the material of choice for hardfacing reactor components [18].

Components hard faced with Colmonoy5, in the centrifugal coolant pumps of PFBR, include the hydrostatic bearing (of both primary and secondary pumps), the pump pipe connection (in the primary pump) and the piston ring seals (in the secondary pump). The main hydraulic components, viz. suction casing, impeller and diffuser, which are made of CF3 (casting of austenitic stainless steel equivalent to 304L), are not hard faced. Hard facing / surface treatment / surface modification of components such as pump impeller is challenging because of the complex vane profile and the danger of distortion during the process resulting in modification of the blade profile / vane angles. Boy et. Al. [19] and Sollars [20] discuss the application of thermal spray coating to bolster resistance to cavitation erosion in water turbines and pumps. Application of hard facing / surface treatment techniques on cavitation susceptible regions of pump hydraulics of future FBR's deserves consideration especially in view of the modest available NPSH and high suction specific speed design for pumps of future FBR's.

Most of the laboratory work reported on cavitation erosion resistance of stainless steel and hardfaced materials are based on the studies carried out with water as the testing medium.. Work done in sodium, in the 1960's and 1970's in USA and France, has mainly involved stainless steels (316, 316L, 3121), iron base alloys (Sicromo 9M, A-286), nickel base alloys (Inconel 600, Hastelloy X, Rene 41), cobalt base alloys (L-605, Stellite6B) and refractory alloys [21,22, 23, 24]. However, little published literature [10] exists on the cavitation damage resistance of Colmonoy in liquid sodium. As Colmonoy5 is the hardfacing material for

components in PFBR, it is important to study the improvement in cavitation damage resistance achieved by hard facing as well as to study the relative cavitation damage resistance of Colmonoy5 vis-à-vis Stellite6.

In the Russian fast reactor BN 1200, the R&D work of which is in progress, the technical feasibility of increasing the life of impellers of the main coolant pumps through the use of anti-cavitation coatings on the impellers is being explored [25]

The above discussion enforces the conclusion that it is therefore worthwhile to study in detail the damage produced by cavitation so as to enable quantification of the relative cavitation erosion resistance of various hardfacing materials.

1.5 ORGANIZATION OF THE THESIS

The thesis is divided into six chapters. The first chapter begins with an introduction to the phenomenon of cavitation in liquids, its insidious effects and the challenge posed in avoiding cavitation altogether. This is followed by a brief description of a fast reactor where liquid sodium is used as the primary and secondary coolant. The major materials used in the hot and cold legs of fast reactors worldwide are then discussed The cavitation susceptible regions in a fast reactor with examples of damage caused due to cavitation are highlighted and the need for a detailed study of cavitation damage in liquid sodium is justified. This is followed by a discussion on cavitation damage observed in various fast reactors. The chapter concludes with a discussion on methods (related to materials) by which cavitation damage can be mitigated such as hard facing (using Co based alloys (eg. Stellite) and Ni based alloys (Colmonoy) and surface treatment methods such as thermal spray coating.

Chapter 2 is an exhaustive literature survey on work done in the area cavitation damage. The chapter reviews the work done in the area of theoretical and experimental estimation of bubble collapse pressure, the liquid and material parameters influencing cavitation damage, the work done in the area of cavitation damage modeling and the experimental methods & facilities available for cavitation damage measurement. The chapter begins with a discussion on the basic theory of bubble collapse and covers the governing equations of single bubble collapse and their limitations, the liquid properties affecting cavitation damage and the theoretical and experimental work done in the estimation of single bubble collapse pressure. The chapter also discusses the laboratory techniques for cavitation damage measurement, the facilities available for measurement of cavitation damage in liquid metals (sodium) and the instrumentation employed in water and sodium for measurement of bubble collapse pressure. The section on predicting cavitation damage from material properties covers the various models used for damage estimation. The chapter concludes with a review of cavitation damage studies done so far in liquid metals.

Chapter 3 covers the numerical estimation of single bubble collapse pressure. The chapter begins with a quick derivation of the Rayleigh Plesset Noltingk Neppiras Poritsky (RPNNP), discusses the limitations of the equation and then moves to the Gilmore equation which is capable of handling liquid compressibility experienced in the final stages of bubble collapse. Both RPNPP and Gilmore equations are solved using the 4th order Runge Kutta (RK) method and the results verified using benchmark problems. A comparison is made between the results of RPNNP equation (incompressible liquid) and Gilmore equation (taking into account the effect of compressibility) as well as between the magnitudes of single bubble collapse pressure in water and in sodium. The large difference between the jet velocities produced in water and in sodium

as well as between the back pressures at the end of bubble collapse, that govern the magnitude of the shock wave produced during expansion, in water and in sodium underline the need for tests in sodium to determine the damage resistance of materials.

Chapter 4 discusses the vibratory cavitation sodium test facility installed in Indira Gandhi Centre for Atomic Research (IGCAR), Kalpakkam, using which the cavitation studies reported in the thesis are carried out.. A detailed description of the test facility and its components, the preheating system, and the instrumentation employed is provided. Design of the mechanical components and the cooling arrangement for the top flange portion of the vessel are also discussed followed by pre-commissioning tests conducted. This is followed by a discussion on the specimen geometry, preparation of specimens for testing, details of sodium composition, operating parameters of the ultrasonic vibratory device and the detailed experimental procedure and cleaning methodology of specimen after testing.

Chapter 5 begins with details of the specimens tested and the test temperatures. This is follows by error analysis of test results. The results of weight loss experiments (cumulative weight loss vs time and cumulative weight loss rate vs time) with SS316L, Colmonoy5 and Stellite6, in sodium at various temperatures, are compared and explained in terms of material hardness, material fracture toughness and stacking fault energy. The chapter concludes with a detailed discussion of the visual and SEM images of the specimens.

Chapter 6 concludes with a summary of the results obtained and directions for further work in this area.

CHAPTER 2

LITERATURE SURVEY

CHAPTER 2 – LITERATURE SURVEY

2.0 INTRODUCTION

This chapter reviews the work done in the field of cavitation especially in the area of cavitation damage. The published literature in the area of theoretical and experimental estimation of bubble collapse pressure, the liquid and material parameters influencing cavitation damage, the work done in the area of cavitation damage modeling and the experimental methods & facilities available for cavitation damage measurement.

2.1 BASIC THEORY OF BUBBLE COLLAPSE

It was Rayleigh [26], in 1917, who first propounded the idea of surface damage in materials through the symmetrical collapse of individual cavitation bubbles. He analysed the symmetrical collapse of individual empty or vapor filled spherical bubbles, at constant pressure during the collapse process, in an inviscid, incompressible liquid. This work was extended by Plesset, Poritsky and others to include the effects of internal pressure of gas in the bubble and the effects of liquid properties like surface tension and viscosity to give the now famous Rayleigh-Plesset equation which expresses the temporal variation in the radius of a collapsing single bubble.

In real systems, the cavitation cloud consists of large numbers of individual bubbles of varying sizes that collapse either in the bulk liquid or adjacent to solid boundaries. The collapse of the bubbles may be spherically symmetric or asymmetric.

Spherically symmetric collapse occurs in bubbles located away from solid boundaries and is driven by a local pressure rise resulting in the bubble contents being compressed to vey high

values of pressure and temperature. The increasing pressure of the bubble contents stops the radially inwards moving bubble wall causing the bubble to rebound and a pressure transient to be generated that evolves into a shock wave front. The interaction of this wave front with a solid boundary results in damage to the solid surface.

Asymmetric collapse of spherical cavities results in the case of cavities attached to the solid boundary. A localised high pressure or shock wave, from the collapse of neighboring cavities, deforms the bubble wall and the resulting asymmetry causes the formation of a high velocity microjet **[**27, 28**]** that pierces the bubble wall and impacts the rigid wall on the other side when the standoff distance is small. The impact of the jet creates a water hammer or jet cutting intensity pressure that stresses the material. In addition, when the compressed bubble rebounds, under the pressure of its contents, a shock wave or pressure wave capable of causing damage is created. The relative magnitude of the water hammer pressure and the shock wave depends on various physical parameters, the collapse pressure differential and the standoff distance **[**29**]**. The damaging phenomenon is thus characterized by high pressures and temperatures existing in localized regions (of few microns to hundreds of microns) near the surface over very short periods of the order of microseconds. In reality, the resulting shock wave or micro jet is due to the collapse of a cluster of bubbles / cavities, with the bubbles at the periphery collapsing first and the resulting pressures causing the collapse of the cavities towards the centre in a concerted manner [30]. The surface is therefore subjected to repeated mechanical loading at high frequency. If the stresses generated are higher than the elastic limit this can result in permanent deformation; however, if the stresses are less than the elastic limit then failure can occur by fatigue. The resulting damage produced is more complex than a unique circular pit.

The collapse mode of a bubble is dependent on its closeness to the boundary. A bubble can collapse multiple times before it is fragmented and dissolves in the liquid. The following impulsive pressures are generated in the first collapse of a bubble attached or very close to a solid boundary : (i) the pressure pulse during collapse (ii) the impact pressure from the liquid jet formed in the bubble (iii) the impulsive pressure from the interaction of the radial flow, following liquid jet impact, and tiny bubbles in the vicinity, and (iv) the impact pressure from the shock wave front produced during bubble rebound [31].

2.1.1 Equations of bubble collapse

The theoretical treatment of cavitation invariably begins with the equations of bubble collapse formulated by Rayleigh [26]. Rayleigh considered the symmetrical collapse of an empty spherical cavity in an infinite body of incompressible liquid under constant pressure. By equating the work done on the system (i.e. liquid and empty cavity) by the constant external pressure to the kinetic energy (KE) gained by the liquid, the expression for the velocity of the cavity wall was obtained

$$U^2 = \frac{2P}{3\rho}\left(\frac{R_0^3}{R^3} - 1\right) \qquad \text{----------} \qquad (2.1)$$

where ρ = density of the liquid, R = bubble radius at any instant of time, R_0 = initial bubble radius, P = pressure at infinity driving collapse, U = bubble wall velocity = $\frac{dR}{dt}$. Equation (1) shows an unlimited increase of velocity as R -> 0. Rayleigh was aware of the problem and resolved the issue by explaining that in reality there will be insoluble gas in the cavity.

Considering the isothermal compression of the gas in the cavity and equating the work done on the system (i.e. liquid and gas filled cavity) to the sum of the KE of the liquid and the work done in compressing the gas, the equation becomes

$$U^2 = \frac{2P}{3\rho}\left(\frac{R_0^3}{R^3} - 1\right) - \frac{2Q}{\rho}\frac{R_0^3}{R^3} ln \frac{R_0}{R} \quad \text{----------} \quad (2.2)$$

where Q = initial pressure within the bubble.

From the above equation, U = 0 when P(1-z) + Q ln z = 0 where $z = (R/R_o)^3$

The equation was improved by Plesset [32], Noltingk and Neppiras [33], and Poritsky [34] to give the now famous Rayleigh-Plesset equation

$$R\ddot{R} + \frac{3}{2}\dot{R}^2 = \frac{1}{\rho}\left\{P_{vp} - P_\infty(t) + P_{g0}(\frac{R_0}{R})^{3\gamma} - 2\frac{\sigma}{R} - 4\mu\frac{\dot{R}}{R}\right\} \quad \text{----------} \quad (2.3)$$

where

P_{vp} = vapor pressure of the liquid, $P_\infty(t)$ = pressure at infinity in the liquid, P_{g0} = initial pressure of gas in the liquid, σ = surface tension of the liquid, μ = viscosity of the liquid.

The above equation is derived with the following assumptions, viz. the bubble is spherical during the entire collapse process, the liquid is incompressible, no body forces exist, conditions within the bubble are spatially uniform and the gas content in the bubble is constant.

In reality, the bubble collapse is rapid and liquid compressibility is to be considered. Flynn [35] discusses other forms of the above equation which take the compressibility of liquid into consideration. The simplest is the acoustic approximation in which the speed of sound is considered constant and this limits its use to cases where the bubble wall velocity is small compared to the speed of sound. The loss of energy due to sound radiation is considered in this analysis. The acoustic approximation equation is given by

$$R\ddot{R} + \frac{3}{2}\dot{R}^2 = \frac{1}{\rho}\left\{P_L + \frac{R}{C}\left(1 - \frac{\dot{R}}{C}\right)\frac{dP_L}{dt} - P_\infty(t)\right\} \quad \text{----------} \quad (2.4)$$

The Herring [36] approximation incorporates a more satisfactory description of the energy loss through compression of the liquid and sound radiation. It is given by

$$\left(1-\frac{2\dot{R}}{C}\right)R\ddot{R}+\frac{3}{2}\left(1-\frac{\dot{4R}}{3C}\right)\dot{R}^2=\frac{1}{\rho}\left\{P_L+\frac{R}{C}\left(1-\frac{\dot{R}}{C}\right)\frac{dP_L}{dt}-P_\infty(t)\right\} \text{ ----------(2.5)}$$

The Gilmore equation [37] considers the formation of shock waves when the bubble wall velocity approaches the velocity of sound. This is achieved using the Kirkwood-Bethe hypothesis which states that the shock waves are propagated with a velocity equal to the sum of the sound velocity and the fluid velocity. This equation is

$$\left(1-\frac{\dot{R}}{C}\right)R\ddot{R}+\frac{3}{2}\left(1-\frac{\dot{R}}{3C}\right)\dot{R}^2=\left(1+\frac{\dot{R}}{C}\right)H+\frac{R}{C}\left(1-\frac{\dot{R}}{C}\right)\frac{dH}{dt} \text{ ----------} \quad (2.6)$$

Based on the appropriate assumption made, one of the above equations may be solved to obtain the variation of bubble radius with time, the variation of bubble wall velocity with time, the maximum jet velocity at the end of collapse as well as the maximum pressure produced in the liquid during bubble collapse.

2.1.2 Liquid properties affecting cavitation damage – comparison between water and sodium

(i) Compressibility - During the final stages of bubble collapse, the wall velocities approach the velocity of sound in the liquid and the liquid behaves like a compressible medium. A portion of the energy of collapse is therefore expended in compression of the liquid resulting in reduced energy for material removal. The water hammer pressure produced by the impingement of the high speed jet produced during collapse is linearly proportional to the velocity of sound in the liquid which depends on the liquid compressibility. The velocity of sound in sodium is proportional to $(B/\rho)^{0.5}$. The bulk modulus of sodium (6.3 GPa) is about ~ 3 times that of water

(2.15 GPa) while the density of sodium at operating temperature is ~ 0.82-0.86 times that of water at room temperature. The damage produced in sodium, at the operating temperature, is therefore expected to be higher

(ii) Viscosity and density – The absolute & kinematic viscosities of sodium at 400 $^{\circ}$C is about 1/3 of that of water at 25 $^{\circ}$C. The effect of viscosity is to retard bubble growth as well as bubble collapse. Therefore as viscosity increases (a) the maximum radius of bubble at the end of expansion is smaller, (b) both the growth rate and collapse rate are smaller and the velocity of bubble wall at the end of collapse is lower. The effect of viscosity is maximum in the early stages of bubble growth and in the final stages of bubble collapse. Poritsky's [34] analysis of the effect of viscosity on bubble collapse in incompressible liquid showed that both growth and collapse of a bubble is strongly affected by viscosity and surface tension. It is, however, seen from numerical calculations of Ivany, considering liquid compressibility, that viscosity and surface tension do not affect the general behaviour of bubble collapse. [27, 38].

(iii) Thermal conductivity of gas / vapor mixture – The higher the thermal conductivity of the gas/vapor mixture in the bubble, the lower is the temperature and pressure of the bubble contents. This increases the bubble wall velocity at the end of collapse and lowers the rebound pressure due to compression of the bubble contents.

(iv) Thermodynamic effect – The thermodynamic criterion was introduced by Stepanoff [39] to explain the reduction in Net Positive Suction Head (NPSH) requirement for pumps handling hydrocarbons when compared to those handling water. The criterion expresses the ratio of the volume of vapor formed per unit quantity of liquid passing through the low pressure zone for

unit reduction in pressure head, under thermal equilibrium conditions. This effect is responsible for the variation of cavitation erosion rate with temperature and is observed not only in pumps but also in vibratory cavitation. This was expressed using the following relationship by Stepanoff, $B = V_v / V_L = (v_v / v_L) * (\Delta h_f / L)$ ---------- (2.7)

where V_v = total volume of vapor produced, V_L = total volume of liquid passing through the low pressure region, v_v = specific volume of vapor, v_L = specific volume of liquid, Δh_f = enthalpy increase corresponding to a reduction in pressure below saturation conditions, L = latent heat of vaporization of the liquid. Although the values predicted by this equation are not meaningful quantitatively, it is able to establish the trend qualitatively. This is because the equation does not consider the rate of bubble formation and bubble collapse, i.e. the heat transfer rate, which depends on the latent heat and thermal diffusivity of the liquid and the equilibrium bubble size. Florshuetz and Chao [40] modified this expression to include the heat transfer effects, viz.

$$B_{eff} = \left(\frac{\rho_L c_L \Delta T}{\rho_v L}\right)^2 \frac{K_L}{R_0} \left(\frac{\rho_L}{\Delta P}\right)^{1/2} \quad \text{---------- (2.8)}$$

Expressing the equation in terms of specific volumes of liquid and vapor

$$B_{eff} = \left(\frac{v_v c_L \Delta T}{v_L L}\right)^2 \frac{K_L}{R_0} \left(\frac{\rho_L}{\Delta P}\right)^{1/2} \quad \text{---------- (2.9)}$$

where k_L = thermal conductivity of the liquid, BTU/hr-ft-$^\circ$F

K_L = thermal diffusivity of the liquid = $k_L/(\rho_L c_L)$, ft^2/hr

c_L = specific heat of the liquid, BTU/lbm-$^\circ$F

ρ_L= density of liquid, lbm/ft^3 ; v_L = specific volume of liquid, lbm/ft^3

ρ_V= density of vapor, lbm/ft^3 ; v_V = specific volume of vapor, lbm/ft^3

R_0 = equilibrium radius of the bubble, ft

ΔP = reduction in pressure causing cavitation, lbf/ft^2

ΔT = reduction in temperature in the liquid film due to vaporization, $^\circ$F

L = latent heat of evaporation, BTU/lbm

B_{eff} = dimensionless

Since the thermal conductivity of liquid sodium is higher than that of water and the volumetric heat capacities of the liquids are similar, the vaporization produced in liquid sodium by a local pressure drop is much more vigorous than in water as it draws upon the heat capacity of the surrounding liquid. A larger ratio of vapor volume to liquid volume means a larger value of B_{eff}. The collapse of such large vapor volumes is inertia controlled resulting in high jet velocities.

(v) Surface tension – The surface tension of sodium is about twice that of water and this results in the maximum bubble radius and the bubble population in sodium being lesser than that in water. The effect of increase in surface tension inhibits bubble formation and retards bubble expansion thereby reducing the potential energy of the bubbles. It, however, also tends to accelerate bubble collapse thereby increasing the potential for damage. As mentioned earlier Poritsky's analysis of bubble collapse in an incompressible liquid showed that both growth and collapse of a bubble is strongly influenced by surface tension and viscosity while subsequent analysis by Ivany including the effect of liquid compressibility has shown that surface tension and viscosity do not affect the behaviour of bubble collapse [27, 38].

(vi) Vapor pressure – The bubbles formed due to cavitation contain a mixture of gas and vapor. During bubble growth as well as the initial collapse period there is adequate time for heat transfer and evaporation / condensation respectively. However, during the final stages of collapse the vapor behaves as an ideal gas because there is insufficient time for condensation and heat transfer. The resulting increase in pressure of the bubble contents has a retarding effect on the bubble wall velocity but also produces a higher rebound pressure. The higher the initial pressure of vapor, the greater is the cushioning effect and the magnitude of the rebound pressure. The vapor pressure of sodium at the reactor operating temperature of 400 $^{\circ}$C is very small compared to that of water at room temperature. Hence (i) the retarding effect in sodium on the bubble wall velocity is much lower than that in water and this tends to aggravate the damage produced by bubbles collapsing adjacent to a surface (ii) the rebound pressure, however, is also lower in sodium than that produced in water and this has an attenuating effect on damage.

(vii) Gas content – Increase in the gas content of the liquid increases the number of bubbles and the extent of the cavitation zone. However, the compression of the gas inside the bubble retards the bubble wall velocity and provides a cushioning effect against collapse. The compression of the gas, however, results in a higher rebound pressure. The dissolved argon gas content in sodium, at the reactor operating temperature of 400 $^{\circ}$C is small compared to that of air in water at room temperature.

The effect of vapor pressure and gas content results in (i) lower cushioning effect in sodium, and (ii) lower rebound pressure in sodium, compared to that produced in water.

(viii) Temperature – As the temperature of a liquid approaches the boiling point, the damage rate is affected by (i) increase in thermodynamic effect which inhibits bubble growth and collapse (ii) decrease in mechanical strength of the material (if the temperature range is large), and (iii) increase in corrosion effect.

(ix) Static pressure - The variation in static pressure results in (i) reduction in the number and size of vapor bubbles in the cavitation zone, and (ii) increase in the pressure differential driving bubble collapse. While (i) tends to reduce damage, (ii) tends to increase damage. The overall effect on erosion damage will depend on the specific application.

Table 2.1 summarises the effect of liquid properties on cavitation damage.

Table 2.1 – Summary of effect of liquid property on cavitation damage

Sl. No.	**Liquid Property**	**Remarks**
1	Compressibility (expressed in terms of Bulk modulus of elasticity, GPa)	Lower compressibility results in higher transfer of collapse energy to the boundary
2	Density	Does not affect the general behaviour of bubble collapse
3	Viscosity	
4	Thermal conductivity of gas/vapor mixture	The higher this value, the higher is the liquid velocity at end of collapse and lower is the gas rebound pressure.
5	Thermodynamic effect (expressed in terms of Beff) – a measure of the ratio of volume of vapor to the volume of liquid in the low pressure zone	A high value results in inertial controlled bubble collapse (high jet velocity)
6	Surface tension	Inhibits bubble formation and retards bubble collapse

Table 2.1 – Summary of effect of liquid property on cavitation damage

Sl. No.	Liquid Property	Remarks
7	Vapor pressure	Increase in vapor pressure has retarding effect on bubble wall velocity but increases rebound pressure.
8	Gas content	Increasing gas content results in increased bubble population. However, it has a retarding effect on bubble wall velocity while the rebound pressure is increased.
9	Liquid temperature	Increase in liquid temperature inhibits bubble growth and collapse.
10	Static pressure	Increase in static pressure reduces the bubble population and size of bubbles. It, however, increases the pressure differential driving collapse which leads to increase in damage.

The above considerations indicate that the damage produced during collapse is a complex phenomenon and is therefore best simulated using the working liquid at the operating temperature. It is observed that the cavitation damage in sodium, at the operating temperature, is more than that in water at room temperature. Preiser [41] has reported that the damage in sodium at 204 $^{\circ}$C is about 1.5 times that in water at 27 $^{\circ}$C.

Liquid properties have a strong influence on the damage rate and therefore cavitation damage in liquid metals (eg. sodium) is best predicted by experiments in the same liquid. However, the high temperature, leak tight operating requirement of a sodium system poses operational difficulties. It is therefore worthwhile to explore the possibility of using surrogate

liquid / material combinations to simulate damage. In spite of the progress made in the past in understanding cavitation damage such a task remains a challenge

2.1.3 Estimate of bubble collapse pressure

Rayleigh's seminal paper [26] is a fundamental analysis of the pressure generated during the collapse of a spherical void initially at rest in an incompressible, inviscid liquid under constant pressure at infinity. He showed that as the collapse nears completion, the wall velocity and the pressure in the liquid approach indefinitely large values. He, however, was aware that a realistic model consisting of a small amount of insoluble gas within the cavity retards the inward motion of the cavity wall, limiting the pressure in the liquid and causing the cavity to rebound.

Using Cook's formula, Rayleigh [26, 27] estimated the pressure generated on a rigid sphere of radius R at the instant a jet of water strikes the surface. In this analysis the liquid is considered incompressible up to the moment the liquid jet strikes the solid surface. The instantaneous pressure exerted on the solid surface is then estimated using the relation,

$$\frac{P\prime^2}{2E} = \frac{1}{2}\rho U^2 = \quad = \frac{P}{3}\left\{\left(\frac{R_0}{R}\right)^3 - 1\right\}$$

where P' = instantaneous pressure generated on the solid surface, Pa, E = modulus of elasticity of water = 20000 atm, P = 1 atm, R_0 = initial radius of cavity, R = final radius of cavity. For R/R_0 = 1/20, he showed that the pressure generated is 10300 atm (1030 MPa) which is sufficient to cause damage.

Hickling & Plesset [42], in their theoretical analysis of a cavity in an inviscid, compressible liquid with spherically symmetric cavity motion, concluded that damage could certainly result from the pressure waves emanating from collapsing bubbles situated some distance from the wall. The cavity was assumed to contain a uniform gas whose pressure varied as ρ^{γ} where γ = 1

for isothermal analysis and γ=1.44 for adiabatic case. The numerical solutions also showed that the bubble wall velocity for an empty cavity approached infinity during compression varying as $(R_0/R)^{0.785}$ where R_0 = initial bubble radius and R = final bubble radius, with the index (i.e 0.785) remaining same for different values of external pressure (viz. P_∞ = 1 atm and 10 atm). In the case of bubbles containing gas, the results showed the rebound of the compressed gas and the formation of a shock wave front in the liquid. It was also observed that isothermal compression of the gas resulted in a more violent collapse when compared to adiabatic compression because in the former case the bubble collapses to a much smaller radius than for the latter case (for the same initial internal gas pressure at the beginning of collapse). The results also showed that the maximum pressure attenuates as 1/r, where r = distance from the centre of the compressed bubble, and that the peak pressure of the wave attenuated from 1000 atm at $r/R_0 = 0.3$ (for $p_0 = 10^{-3}$ and $\gamma = 1.4$) to 200 atm at $r/R_0 = 2$. This attenuation of the peak pressure with distance led to the conclusion that bubbles must necessarily collapse close to a solid boundary to produce damage. The initial pressure of gas inside the bubble was observed to also have a strong cushioning effect on the maximum pressure. The peak pressure of the wave was reduced from 1000 atm for $p_0 = 10^{-4}$ (with $\gamma = 1.4$ and $r/R_0 = 2$) to 200 atm for $p_0 = 10^{-3}$ atm (where p_0 = initial gas pressure inside the bubble and γ = exponent of radius during compression) [43]. Ivany [38], in his analysis of a spherically symmetric cavity in a viscous, compressible liquid, concluded that there is no shock wave produced during collapse and the pressure generated in the liquid, during collapse, at a distance equal to the initial bubble radius is insufficient to cause damage. However, the rebound of the bubble can generate a shock wave capable of producing damage. Since the maximum pressure attenuated as 1/r, it was necessary for a bubble to be close to the surface to cause damage.

Benjamin and Ellis [44] in their experimental work, showed that a cavity acquires a translation motion towards the boundary during collapse since the cavity volume becomes a small fraction of its original volume while its centroid moves towards the boundary. As the shrinking cavity accelerates towards the boundary, circulation is produced in the liquid and the cavity takes the form of a torus thus producing a hollow vortex ring. A jet, formed by involution at the back of the bubble, results in the transfer of a large impulse onto the solid boundary. The large water hammer pressure generated by the impact of the jet is in addition to the high pressure from compression of the cavity contents. Their photographs of single bubble collapse near a solid boundary showed the involution of the cavity on the side farther away from the wall and the formation and impingement of a jet during the collapse process. It is concluded that even after the moderating influence of liquid compressibility is accounted for there is no doubt that collapse pressures can typically be of the order of 10^4 atm.

Naude and Ellis [45] in their investigation to understand the mechanism of damage due to cavities collapsing in contact with a solid boundary concluded from measurement of the dimensions of the pit produced on aluminum specimen that the cause of damage was not the high pressure of cavity contents resulting from their compression during collapse but the effect of impact of high speed jet produced during collapse.

Plesset and Chapman [46] concluded from numerical investigations of asymmetric vapor bubble collapse in incompressible, inviscid liquid that jet speeds as high as 130 m/s to 170 m/s are possible for bubbles attached to a solid boundary and away from it respectively under a collapse pressure of 1 atm. They showed that the damage caused is more likely due to the high stagnation pressure generated when the jet is stopped by the solid surface than from the water

hammer pressure because the time of action of the stress in the former case is an order of magnitude higher than that in the latter case (order of 10^{-7} sec).

While initially the cause of damage to a surface was considered to be due to the collapse of an essentially spherical cavity and the impingement on the surface of the shock waves created during collapse [26], later theoretical and experimental evidence have shown that mechanical damage to the surface results from the impingement of high speed liquid jets resulting from the asymmetrical collapse of vapor bubbles very close to the surface. It is also understood that a shock wave is produced during the rebound of the compressed bubble, under the effect of its high internal pressure, and not during the collapse of the bubble. This results in the formation of a shock wave front that causes damage to the surface [47].

Plesset and Ellis [48] while investigating the mechanism of cavitation damage in polycrystalline materials and pure monocrystals concluded that damage results from plastic deformation and cold work leading to fatigue failure under repeated mechanical loading from vapor bubble collapse. It was observed that the X ray diffraction pattern of the specimen, which was sharp before exposure to cavitation, became diffused after cavitation exposure of a few seconds in water indicating the onset of plastic deformation. They have estimated the pressure pulses to be between 50,000 psi (~ 3400 atm) and less than 130,000 psi (~8844 atm).

2.2 TECHNIQUES AND FACILITIES FOR CAVITATION DAMAGE MEASUREMENT

2.2.1 Laboratory Techniques

Several methods have been used in the laboratory for the measurement of cavitation damage. These are explained briefly.

(i) Water tunnel - The water tunnel is used to study cavitation produced by hydrodynamic pressure reduction. It consists of (i) a piping system with circulating pump (ii) a test section inside which the body to be tested is mounted (iii) instrumentation and control system for measuring flow parameters, dissolved air content and maintaining liquid temperature (iv) resorber section for re-absorbing dissolved air released in the test section. Cavitation is generated by the presence of the body in the test section. Damage occurs on the body surface where the bubbles collapse. Chapter 2 (pages 22 to 34) and Chapter 10 (pages 444 to 497) in ref. 2 discusses several water tunnels in detail. Fig. 2.1 below shows the test section in the cavitation water tunnel in Hohenwarte II pumped storage power plant in Germany.

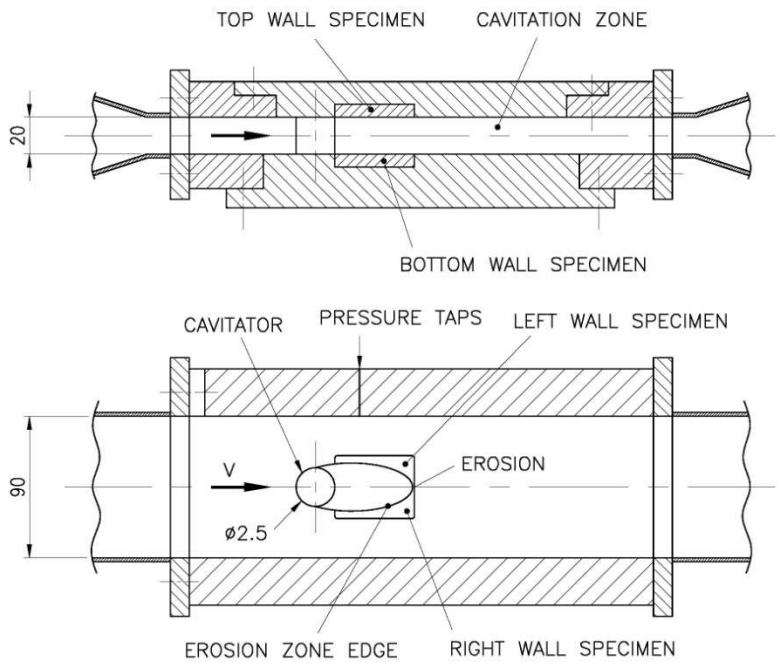

Fig. 2.1 – Test section in cavitation tunnel in Hohenwarte II pumped storage power plant in Germany [49]

(ii) Venturi [50]: A venturi device employs restriction in the flow cross section to convert pressure head into velocity head and thereby generate cavitation. The specimens are mounted downstream of the throat where the bubbles collapse causing damage. The venturi test section is mounted in a water tunnel / closed loop system in which the test liquid is circulated. A typical design used at the University of Michigan (U-M damage venturi) for study of cavitation damage is shown in Fig. 2.2 below.

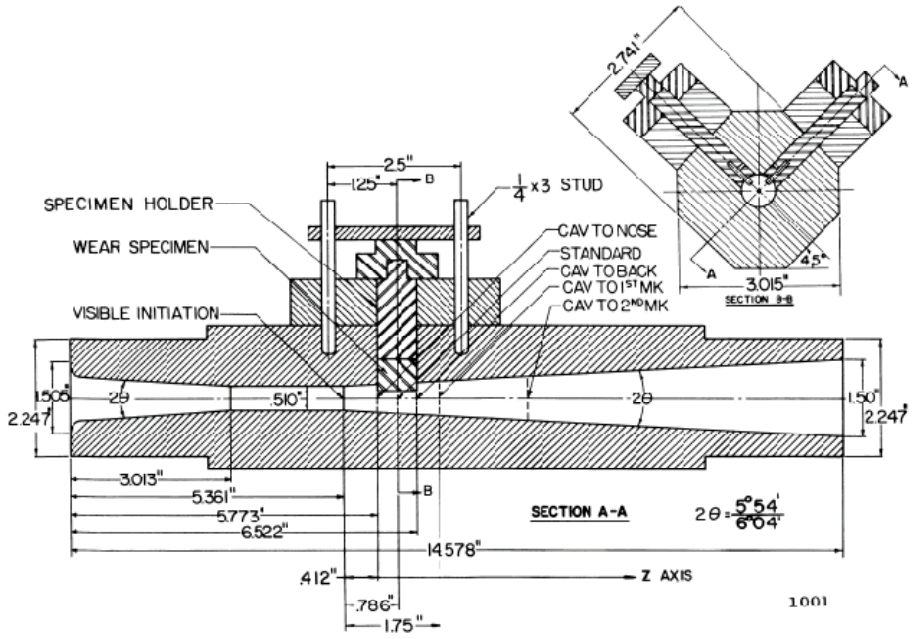

Fig. 2.2 – Venturi design (U-M damage venturi) used for cavitation studies at University of Michigan by Hammitt and colleagues [51]

Other design variants include that of Boetcher at Holtwood laboratory and Shal'nev [50]. In the Boetcher type (Fig. 2.3) , cavitating jet impinges directly on the specimen while in the Shal'nev design (Fig. 2.4) cavitation is generated downstream of the model resulting in erosion of the specimen fixed to the wall of the device. Both devices generate much more intense cavitation than that due to a U-M venturi.

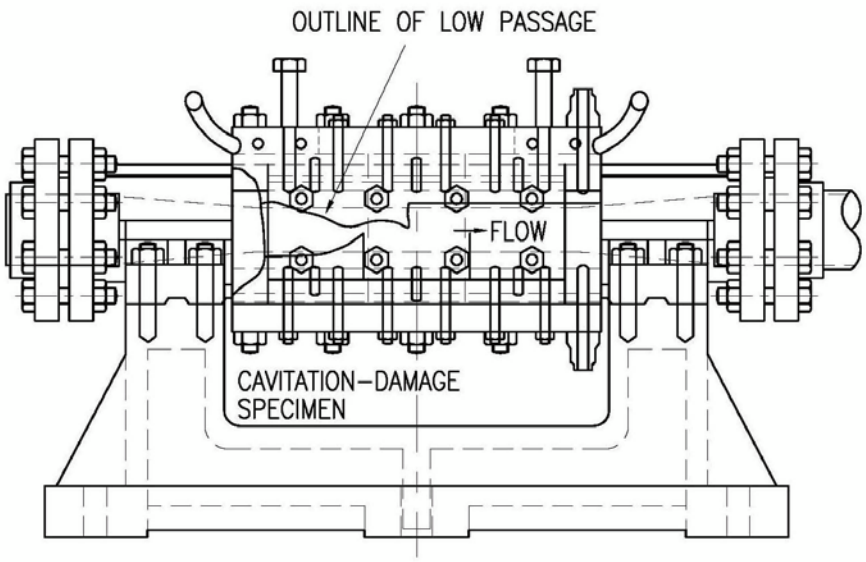

Fig. 2.3 – Boetcher type cavitating device [50]

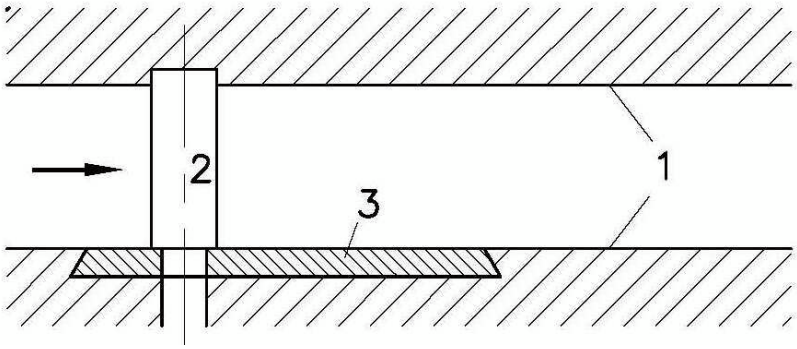

Fig. 2.4 – Shal'nev type cavitating device [50]

1 – Flow boundary, 2- model, 3 – test specimen

(iii) Rotating disk device : This device, originally by Rasmussen, consists of a disk provided with pins or through holes at various radii. The disk rotates at high speed in the test liquid and cavitation is produced by the movement of the pins or holes in the disk through the stationary liquid. The cavitation bubbles collapse on the test specimens that are mounted flush on the disk

surface. Rigid body like rotation of the liquid is prevented by the presence of baffles in the chamber. Fig. 2.5 shows the device at the IMP PAN lab in Gdansk, Poland.

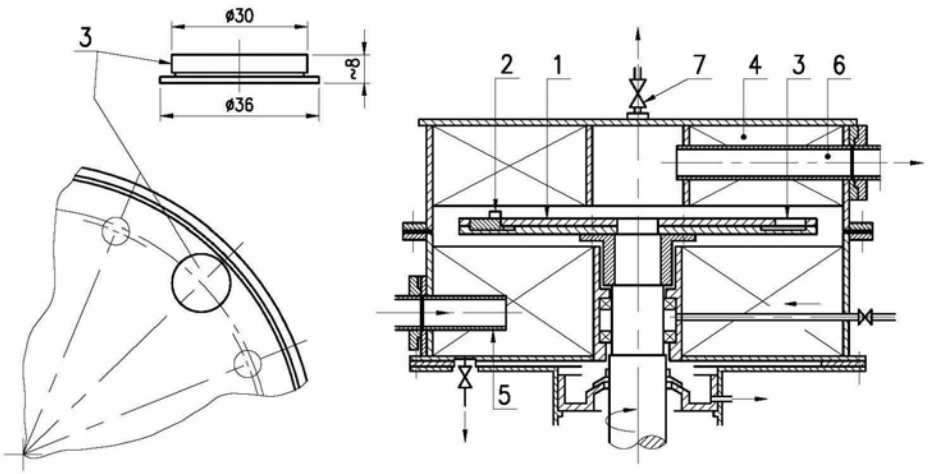

Fig. 2.5 – Rotating disk device [49] **1 – disk; 2-cavitator (pin); 3-specimen; 4-stagnator vane; 5,6-liquid inlet, outlet; 7-de-aerating valve**

(iv) Rotating wheel [50] : This device consists of a rotating wheel on the periphery of which the test specimens are mounted (Fig. 2.6). The wheel is rotated in the path of a water jet located coaxial with the axis of rotation of the shaft and at a radial distance from the shaft that is equal to that of the specimens from the shaft.

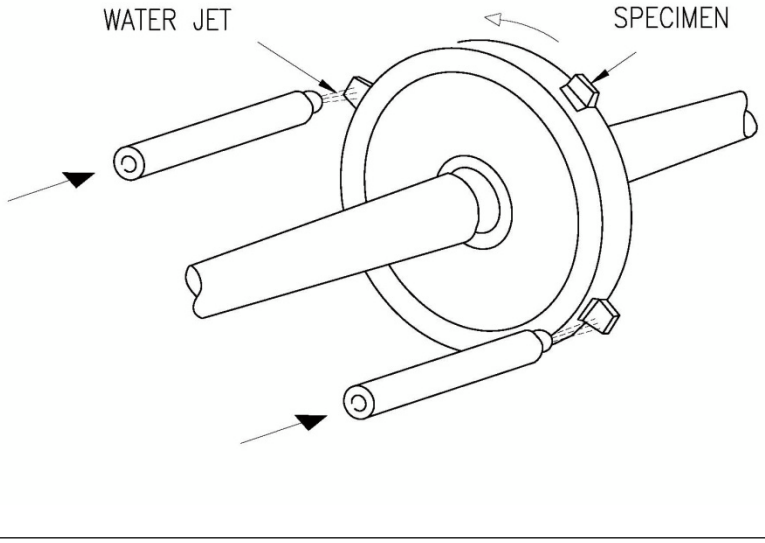

Fig. 2.6 – Rotating wheel [50]

(v) Vibratory cavitation device [50] : This device consists of a rod (called horn) to the bottom of which the test specimen is mounted. The horn is mounted on the test vessel, containing the liquid in which cavitation is to be produced, with the specimen immersed in the liquid (Fig. 2.7) . The horn is vibrated at ultrasonic frequency of 20 kHz using a piezoelectric (or magnetostrictive) crystal and converter /booster arrangement. The mechanical oscillation of the crystal under the influence of the applied electric (magnetic) field is magnified by the booster to which the horn is mechanically fixed. The horn further amplifies the mechanical vibrations and transmits it to the specimen mounted at the other end. The high frequency oscillation of the specimen, which is immersed in the test liquid, generates an acoustic field in the liquid and produces cavitation at the bottom face (which is normal to the direction of oscillation) of the specimen. There are two variants to this design viz. that (i) in which the specimen is fixed to the horn and vibrates with the horn (as above), and (ii) the specimen is kept stationary at a 'stand-off distance' from the bottom of the horn. The vibratory device has several advantages, viz. (i) the design is simple allowing easy sealing of the test liquid (ii) requires small inventory of test liquid which is an

advantage when handling hazardous liquids like liquid sodium (iii) facilitates rapid testing of materials especially for comparison of relative ranking of cavitation resistance. This technique is standardized by ASTM using the standard ASTM G 32 [52]

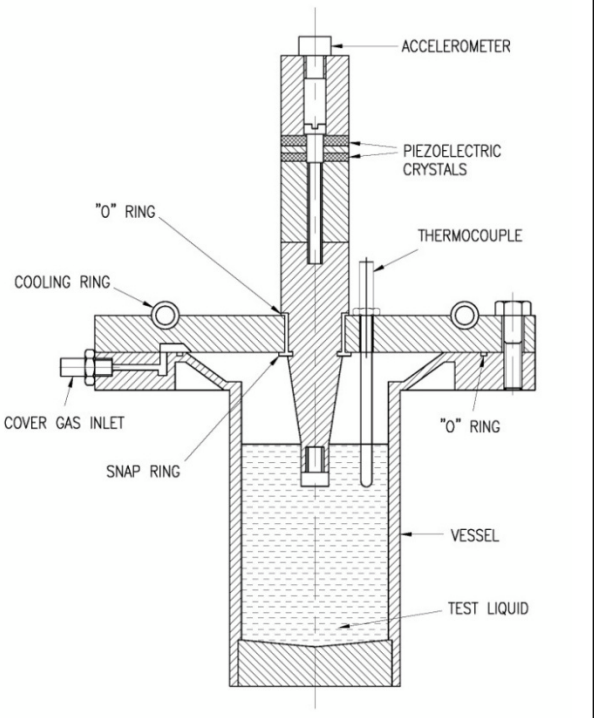

Fig. 2.7 – Vibratory cavitation device [50]

(vi) Cavitating jet method / Lichtarowicz cell [53, 54] (Fig.2.8) : In this device a cavitating jet is used to produce erosion. A positive displacement pump is used to deliver constant rate of liquid through a sharp entry cylindrical bore nozzle resulting in the discharge of a jet of liquid into a chamber at a controlled pressure. Cavitation begins at the vena contracta of the jet within the nozzle. The specimen is placed in the path of the jet at a specified stand-off distance from the nozzle. The cavitation bubbles collapse on the specimen causing damage. The arrangement is

small, simple and inexpensive and can be used for fast evaluation of materials. This technique is standardized by ASTM using the standard ASTM G 134 [55]

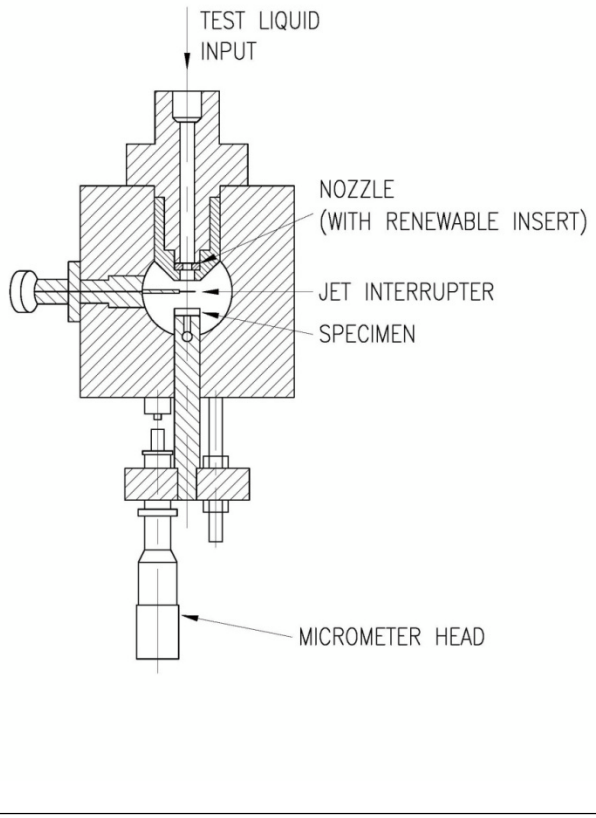

Fig. 2.8 – Lichtarowicz cell [54]

(vii) Cavitation chamber with slot cavitator (Fig. 2.9): The test section in this arrangement consists of a semi-cylindrical barricade and slot width adjuster system. The specimens to be tested are mounted downstream of the slot. The device is installed in a cavitation tunnel and cavitation intensity at the slot is varied by adjusting the slot width and pump flow rate. Quartz glass windows in the test section facilitate visual observation of cavitation.

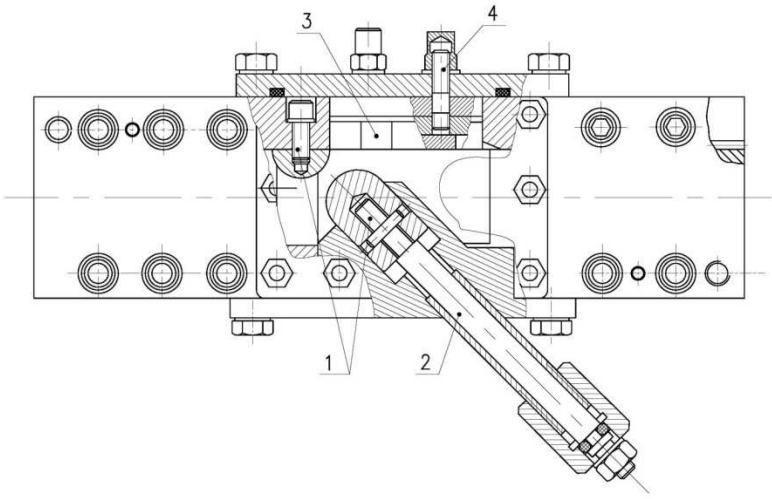

Fig. 2.9 – Slot cavitator in cavitation chamber [56] **1-Semicylindrical barricade, 2-slot with adjustment screw, 3-specimen, 4-pressure transducer**

In principle all the above techniques are applicable for any liquid. However, selection of a facility will depend upon factors such as (i) whether the study is to compare the relative cavitation damage of materials or if it is to study the performance of a material under operating conditions (eg. flow, temperature , pressure) (ii) ease of engineering the system (eg. achieving leak tightness in the case of hazardous liquids) (iii) parameters measured (eg. damage rate, collapse pressure) (iv) test duration.

As seen in the preceding paragraphs various types of devices are available for simulating cavitation erosion. The different types are, however, suited for specific applications. For instance, a venturi device (i.e a flow device that employs a flow restriction to convert pressure head into velocity head and thereby creates a cavitation zone) simulates the erosion damage in a flowing system more closely compared to a vibratory device. The water tunnel, U-M damage venturi, Boetcher type device, Shalnev type device all fall into this category.

The rotating disk device, however, mimics the erosion damage in a turbomachine. When the cavitation damage in different candidate materials is to be evaluated in a short time, a vibratory device is preferred.

Among the various erosion testing methods, the vibratory method and the cavitating jet method or Lichtarowicz cell are standardized, in ASTM G32 and ASTM G134 respectively, thus providing acceptable methods for laboratory use.

2.2.2 Facilities for liquid metals

Reference [50] contains an excellent compilation of laboratories around the world engaged in cavitation research. Almost all the facilities listed here, save for notable exceptions such as that at ORNL, NASA at CANEL and at Hydronautics, CEA-Cadarache, are for studies in water. Cavitation erosion studies in sodium has been limited not only because of the restricted application of the liquid (eg. in the LMFBR program, SNAP system etc.) but also because of the special precautions to be followed during handling of the liquid. However, in view of the insidious effect of long term cavitation damage in sodium and mindful of the fact that it is not economically sustainable to design hydraulic machinery for cavitation free operation, LMFBR R&D programs have invested time, effort and money in the construction and operation of experimental loops for the study of cavitation erosion.

Some of these loops are :

(i) Sodium test facility at Westinghouse-Advanced Reactors Division (W-ARD) [7] (Fig. 2.10) : The main goals of this facility were to (i) study the degree of cavitation damage in a prototype LMFBR as a function of time (ii) to compare damage rates in sodium with that in a conventional liquid like water (iii) to understand the difference in damage produced in the hot leg with that in the cold leg. The loop consisted of a main portion

and two auxiliary or side loops, viz. a cold loop at an isothermal temperature of 371°C and a hot loop at an isothermal temperature of 537.7°C. Both these loops were connected through the main loop which was therefore subjected to a temperature differential of 166.7°C. A venturi test section was used to generate cavitation damage. The facility was used to study the effect of temperature on cavitation damage in sodium as well as to compare the Mean Depth of Penetration (MDP) in sodium with that produced in water.

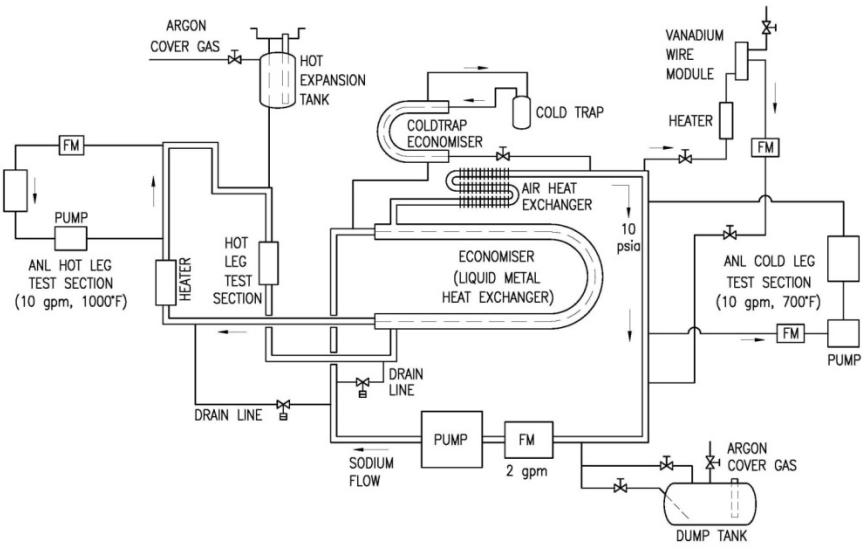

Fig. 2.10 – Sodium test facility with venturi test section for cavitation testing at W-ARD [7]

(ii) The cavitation loop at Risley Engineering and Materials Laboratory (REML) [57] : The sodium cavitation test loop at REML was a small (maximum flow rate 40 lps) bypass loop connected to the pump test facility. The loop employed a venturi test section and

operated in the range 200 °C to 400 °C. The facility had a provision to vary the quantity of free gas in the system by means of external injection. Fig. 2.11 is a schematic of the sodium cavitation loop at REML.

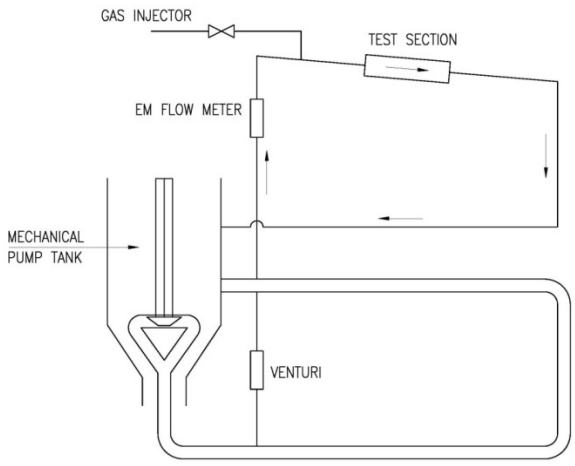

Fig. 2.11– Schematic of sodium cavitation test loop at REML [57]

(iii) CANADER sodium loop [58, 59] : This loop was used for cavitation inception and erosion tests in sodium. It had a nominal flow rate of 10 lps and maximum pressure rating of 10 bars. An electromagnetic pump was used to circulate sodium through the loop. A pressure reducer downstream of the test section was used to create a variable pressure drop and thus simulate the pressures at various operation points in the nuclear reactor while maintaining the pressure in the downstream tank above atmospheric pressure (to prevent air ingress). Fig. 2.12 is a sketch of the CANADER sodium loop.

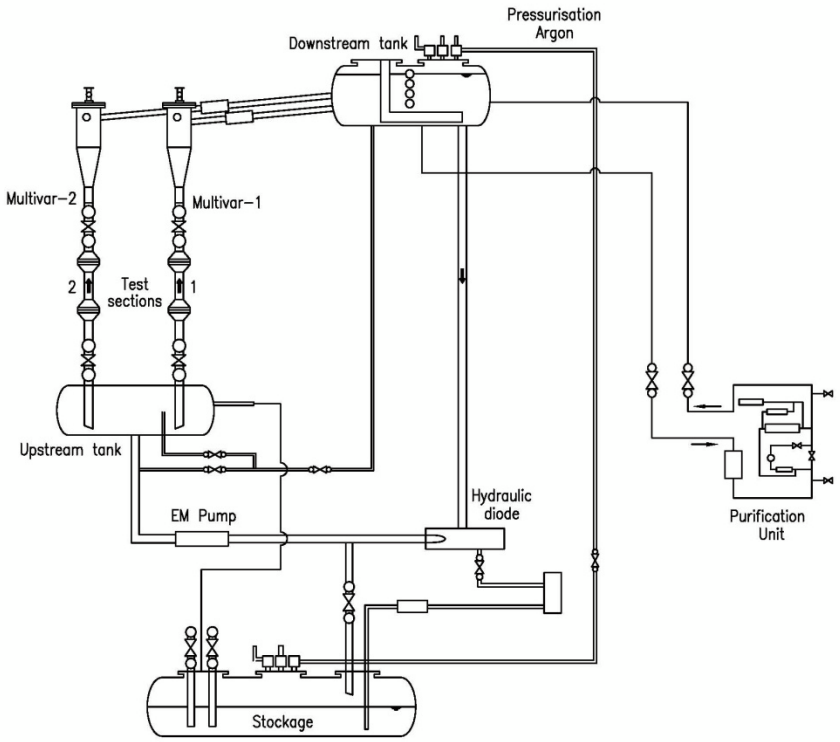

Fig. – 2.12 CANADER sodium loop [58]

(iv) CARUSO : [60, 61] : One of the secondary loops of the RAPSODIE plant was modified and briefly used for the cavitation testing of the PSX2 (SuperPhenix 2) pump impellers to decide on the cavitation margin.

(v) Vibratory cavitation device : This device employs small amplitude ultrasonic vibration of a horn, immersed in liquid sodium, to generate cavitation. This is the simplest and widely used device, especially for producing cavitation in liquids that require careful handling, eg. sodium. This technique is preferred for rapid evaluation of cavitation erosion resistance of different materials. The device used for sodium testing is provided with additional features, compared to that used for water testing, such as leak tight sealing of the cavitation chamber from the atmosphere and suitable cooling facility to ensure that temperatures at the top of the horn and

the piezoelectric device are within limits. The device is useful for cavitation erosion rate testing in sodium because the vertical testing arrangement makes it possible to easily seal liquid sodium from the atmosphere through an intermediate cover gas. The system has been used at the University of Michigan [62, 63], at Hydronautics Inc [64] and at NASA, CANEL [65]

It is clear from the above discussion that detailed facilities have been used worldwide for the study of cavitation damage in sodium; the severity of cavitation damage in sodium was perhaps the motivating factor in the construction of these facilities.

2.2.3 Instrumentation for impact load measurement

Measurement of impact load on a surface due to collapse of cavitation bubbles is essential to understand the loading of the surface under cavitation. Accurate measurement of impact loads and their characterization (such as amplitude, loading rate, spatial distribution etc.) coupled with the ability to model material response is invaluable in the prediction of damage and its temporal evolution.

To determine the correlation between cavitation damage and the concomitant cavitation noise produced by individual bubble collapse, experiments were done at the University of Michigan [66, 67], in water and in sodium using (i) a wave guide type probe, and (ii) a submerged type probe. Such a correlation is useful in the prediction of cavitation damage a priori from bubble collapse noise spectra.

The wave guide probe employed a stainless steel rod of about 1 ft in length with one end of it immersed in sodium and the other end connected to a Barium Titanate piezoelectric crystal. The operating principle of the wave guide was based on the conversion of the force on the PZT

crystal, generated from the collapse of vapor bubbles on the immersed face of the rod, into a proportional electrical charge output.

The submerged type probe employs a high temperature PZT crystal which is enclosed in a stainless steel diaphragm so that it does not come into direct contact with sodium. The pressure of the collapsing vapor bubbles on the stainless steel diaphragm is converted into a proportional electrical charge output by the PZT crystal. These experiments concluded that it is possible to predict the damage rate due to cavitation by measuring the resulting cavitation bubble collapse spectra. This is useful for cavitation damage prediction of hydraulic machinery in the field.

Okada et al [68] developed a pressure transducer that could simultaneously measure the impact load from bubble collapse as well as the attendant damage. The sensor was a pressure sensitive piezoelectric ceramic disk of 3 mm in diameter and 0.2 mm in thickness with a resonance frequency of 10 MHz. Tests were done in water at room temperature, on specimens of Cu, Al and SS 304, using a vibratory device as well as a venturi system. The standoff distance of the sensor from the vibratory horn was 1 mm. Impact loads, at early stage of cavitation, were compared with the size of the indents produced and a linear relation observed between the impact load and the indent area.

Momma and Lichtarowicz [53] used a film type pressure sensor made from the piezoelectric polymer PVDF (Polyvinylidene Fluoride) to measure collapse pressure in a cavitating water jet apparatus. PVDF transducers are capable of withstanding severe cavitation. Moreover, they also have high resonance frequency which is essential for capturing short duration cavitation pulses. Their results showed that the peak erosion rate correlated very well with the sum of the square of the measured pulse heights.

In the effort to characterize the pressure distribution in a cavitating field in water, Sowmitra Singh et al [69] employed a commercially available high response pressure transducer (PCB 102A03) with a rise time of 1 μs, a resonance frequency of 500 kHz, sensitivity of 0.5 mV/psi, an exposed sensitive area of 3.14 mm^2 (2 mm in diameter) and a base diameter of 5 mm. The sensitive area of the transducer was protected from cavitation erosion by a plexiglass insert. The possible overlap of pressure pulses of the collapsing bubbles was minimized by modifying the insert so as to reduce the effective sensitive area from 19.63 mm^2 to 3.14 mm^2. The sensor was employed for pressure measurements in the cavitating field of an ultrasonic horn as well as that of a cavitating jet. The standoff distance of the sensor from the ultrasonic horn was 0.5 mm. It was concluded that the pressure fields from cavitating jet as well as an ultrasonic horn can be characterized by cumulative number distribution of the cavitation impulsive pressure peaks as functions of pressure peak amplitude. The distribution was found to be similar to a Weibull distribution.

Jean-Pierre Franc et al [70] measured the impact load in the cavitating field of a high speed cavitation loop using a commercial piezoelectric pressure tansducer (PCB 108A02) with a natural frequency > 250 kHz, and rise time smaller than 2 ms. The sensitive area of the sensor was 3.6 mm in diameter and the outer diameter of the sensor was 6.2 mm. Sampling rates of 2 MHz and 50 MHz were employed to obtain detailed impact load distributions. It was observed that while the relative comparisons of the impact loads are satisfactory, the absolute values require further confirmation. It is also seen that the measured impact loads do not corroborate with the values obtained from analysis of results of pitting tests using conventional nanoindentation tests at low strain rates.

An integrated pressure sensor and specimen was developed by Hattori et al [71] to evaluate the cavitation erosion resistance of materials. The erosion of nine different materials were studied in water using a vibratory device and a venturi system. It was concluded that a linear relation exists between the accumulated impact energy (expressed as the summation of squares of the measured impact loads) and the cumulative volume loss of material and that when materials are exposed to a given impact energy the cumulative volume loss is independent of the test conditions such as amplitude of vibration and stand off distance. The pressure sensor employed a piezoelectric ceramic disk (of $PBTiO_3$ and $PbZrO_3$) sandwiched, using electrically conducting adhesive, between a 20 mm length pressure detection rod and 15 mm length pressure reflection rod. The sensor, supplied by MURATA co. Ltd., was 3 mm in diameter and 0.5 mm in thickness.

Carnelli, Karimi and Franc [72] have pointed out that the methodology of estimating the impact load from collapse pressure measurement may not be accurate because of (i) the size of the sensors which is often larger than the cavitation bubbles (ii) the resonant frequency of the transducers which is often lower than the bubble collapse frequency (iii) the high rise time of the transducers. They have instead proposed the idea of using the material itself as a sensor and calibrating / inferring the magnitude of the collapse pressure from the geometric characteristics of the pits, produced in cavitation testing, using the Tabor relationship[1] and the hypothesis of pits with spherical cap geometry. Instead of using mechanical properties derived from conventional

[1] In an indentation test, the strain produced at the indenter contact surface is given by Tabor's relation, $\epsilon = 0.1\ \frac{a_c}{R}$ where ε = strain produced by the indenter, a_c = projected radius and R is the end radius of the spherical tip. For a cavitation pit with a spherical cap geometry, the strain is given by $\epsilon = 0.2\ \frac{d/2}{R}$, where d = diameter of the cavitation pit, R = $\frac{d/2^2 + h^2}{2h}$ where h = pit depth. The stress producing the indentation / cavitation impact pressure is obtained in either case using the Ramberg-Osgood relation, $\epsilon = \frac{\sigma}{E} + \epsilon_0 \left(\frac{\sigma}{\sigma_0}\right)^{1/2}$

mechanical tests, they used depth-sensing nanoindentation measurements to obtain mechanical properties of the test sample viz. Nickel-Aluminum-Bronze alloy C95800 which was subjected to cavitation in a cavitation tunnel using water as the working fluid at velocities ranging from 45 m/s to 90 m/s. The indentation tests were done using a spheroconical diamond probe tip with a nominal radius of 10 μm at a constant indentation rate of 0.05 1/s. They concluded that there was a strong, almost linear, correlation between the impact load and the pit volume.

Choi and Chahine [73, 74] carried out a computational study to investigate the suitability of the approach of deducing the collapse pressure amplitude from pit geometric characteristics, using the Tabor relation, by numerically simulating the pits formed under impulsive pressure loading and comparing the Tabor predicted peak pressure from the resulting pit with the peak collapse pressure applied to the material. Their inference was that the approach was more qualitative, rather than quantitative in nature, and that the peak pressure inferred from the pit geometry was the maximum effective von Mises stress in the material instead of the peak pressure due to cavitation. The unanimous conclusion from the results of four metals that were investigated (viz. Aluminum 1100, Aluminum 7075, Nickel Aluminum Bronze and Stainless steel A2205) was that the value estimated from pit dimensions, using Tabor's formula, underestimated the actual loading, due to cavitation, by a large factor.

Bubble collapse pressure measurement is invaluable in the characterization of impact pressure loading. This characterization is important because the response of materials is influenced by the load distribution. Although pressure transducers are commercially available for water applications, the probes required for high temperature liquid metal applications often need to be custom built.

2.3 PREDICTING CAVITATION DAMAGE FROM MATERIAL PROPERTIES

Research on cavitation erosion damage of engineering materials has been in progress since the 1930s and extensive investigations have been carried out mainly in water and to some extent in liquid metals [27, 50]. The objectives have been to (i) estimate the resistance of materials to cavitation damage and rank them in terms of this parameter (ii) to correlate the cavitation erosion resistance of untested engineering materials with that already tested in terms of easily measured material properties (iii) to explore the possibility of reducing the testing time by using a weaker material for laboratory testing and then establish a correlation between the erosion resistance of the material used in the field to that tested in the laboratory by relating the measured erosion rate in the laboratory with the respective material properties [75] (iv) to arrive at correction factors that can be used to convert the erosion resistance measured on scaled models in the laboratory to prototype components (v) to correlate the erosion damage to physical properties such as tensile strength, yield strength, engineering strain energy, true strain energy, hardness, elongation, reduction in area and elastic modulus (vi) to develop phenomenological models.

Rao and Thiruvengadam [76] showed that the erosion rate measured for commercial aluminum samples of different hardness was inversely proportional to yield strength, ultimate strength and hardness. Thiruvengadam [77], Thiruvengadam and Waring [78] showed that this, however, was not the case for materials with different chemical composition (eg. three grades of Aluminium, SS 304L, SS 316, SS 410, Molybdenum, cast iron, Tobin Bronze, Monel) . It was observed that the reciprocal of the steady state volume loss rate correlated best with the strain

energy[2] and poorly with the common mechanical properties such as yield strength, ultimate strength, Brinell hardness, modulus of elasticity and ultimate elongation. Hobbs [79] showed that the maximum erosion rate correlated well with the ultimate resilience[3] in the case of tool steels.

Hammitt [50] attempted to formulate a relationship between erosion rate and easily measured engineering parameters using data from both liquid impingement and cavitation experiments. The combined data was used considering the similarity of the erosion process in liquid impingement and cavitation. The simplest correlation between the erosion rate, expressed in terms of the Mean Depth of Penetration Rate (MDPR) (MDPR, μm/hr is defined as the rate of volume loss per unit of exposed area) was found to be proportional to the ultimate resilience of the material.

Tichler et al [80] ,however, found that the true tensile strength was most representative of the erosion strength for a group of chromium steels while Syamala Rao [81] concluded that the product of ultimate resilience and Brinell hardness was the most relevant parameter of erosion strength. Heyman [82], however, indicated that the product UTS^2 * E was the appropriate parameter for a wide range of materials, where UTS and E are the ultimate tensile strength and modulus of elasticity respectively of the material.

---

[2] Strain Energy (SE) is defined as the area under the engineering stress strain curve from a tensile test. When the stress / strain curve is unavailable it is approximated using the relation , SE =$(\frac{\sigma_{YS} + \sigma_{ult}}{2})\epsilon$ where σ_{ult} = ultimate tensile strength, σ_{YS} = yield strength and ε = ultimate elongation

[3] The Ultimate Resilience (UR) (aka Hobb's Ultimate Resilience) is defined as the area under the true stress vs true strain curve assuming linear stress/strain relationship up to fracture. It is given by the formula

UR = $\frac{1}{2}(\frac{\sigma_{ult}^2}{E})$ where σ_{ult} = ultimate tensile strength and E = modulus of elasticity.

Hattori and Ishikura [83] analysed 990 data points of cavitation erosion testing of 143 materials (iron and steel, cast iron, stainless steel – rolled, stainless steel-castings, al alloys, cu alloys, Ti alloys, Ni alloys, Co alloys, plastic, ceramics etc.). The tests were conducted in water using vibratory device (stationary specimen and vibrating specimen), venturi and rotating disk. They observed that for stainless steels the cavitation erosion resistance (defined as the reciprocal of the erosion rate) was expressed as

$$\text{Erosion resistance} = 2.6*10^{-7}* (HV * F_{mat})^{2.4} \quad \text{----------} \quad (2.10)$$

where HV = Vickers hardness of the specimen surface after the erosion test, F_{mat} = material factor = $HV_{\text{after erosion test}} / HV_{\text{before erosion test}}$

The importance of accurate quantification of cavitation damage of materials was emphasized when an international effort, known as the International Cavitation Erosion Test (ICET), involving 15 laboratories and 24 test facilities, was initiated in 1987 by the Institute of Fluid Machinery of the Polish Academy of Sciences (IMP PAN) to formulate guidelines for standardizing flow cavitation methods [56]. The exercise involved testing of 6 materials in water in these facilities which included vibratory rigs, cavitation tunnels, rotating disks and cavitating jet cells. The study concluded that while standardization of experimental techniques was a basic requirement for accurate prediction of cavitation damage of materials, it was equally important to obtain information about the distribution of cavitation loading (frequency and magnitude of collapse pressure pulses). The study also motivated the formulation of a model by Steller and his team [84, 85] for the prediction of cavitation damage.

Steller [84, 85] observed that often there was poor agreement between cavitation resistance of materials measured in different types of test rigs and this proved to be a stumbling block in the prediction of material performance in the prototype. He pointed out that the

cavitation load distribution on a material influences the response of the material (eg. structural transformation, work hardening) and that the dependence of results on the test technique can be eliminated only by correlating the progress of erosion with the cavitating loads applied on the material. Steller accounted for the cavitation load conditions in the prediction of progress of erosion using an equation of the form MDE = MDE(R, J, t) ---------- (2.11)

where R = a matrix representing the material erosion resistance under cavitation load of specified structure, J = density of energy flux delivered to the material by the collapsing bubbles; MDE = mean depth of erosion = $\Delta V/A$, mm, ΔV = volume of material eroded, mm^3, A = area of specimen face, mm^2

The cavitation intensity factor, ME was given by

$$ME = \frac{A}{A_0}\frac{\tau}{2C\rho}\sum_{i=1}^{N} n_i p_i^2 \quad \text{----------} \quad (2.12)$$

where n_i is the number of pressure pulses of peak value p_i recorded in unit time by a pressure sensor of membrane surface area, A, mm^2; A_o is the membrane surface area of a reference sensor, mm^2; τ is the average cavitation pulse duration (assumed to have an average value of 10^{-5} s; ρ is the liquid density, kg/m^3; C is the velocity of sound in the liquid, m/s; N is the total number of pulses. J was assumed to be proportional to the cavitation intensity factor

Therefore MDE = MDE(R, ME, t) and the total eroded volume , ΔV is calculated using a superposition law wherein the fractional volume loss curve is given by the expression

$$\Delta V_i = A.\ MDE(R_i, E/A)_{i=1..N} \quad \text{-- (2.13)}$$

Since the material behaviour is influenced by the absorption of energy of bubble collapse the superposition of volume losses due to load fractions is justifiable only for small increments of

time. In this incremental time period, the volume eroded is considered as the sum of the volume losses due to the delivered energy increments.

Rao and Young [86] combined and analysed their experimental data from rotating disk device and vibratory device on a wide range of materials (such as Ni, Al, Zn, Fe, L-605 cobalt based alloy, Stellite and SS 316) tested in both water, at room temperature, and sodium at 204 to 649. They concluded that the results could be fitted by an almost universal curve by plotting the normalised cumulative erosion rate against the normalised time. The cumulative erosion rate was normalized with respect to the maximum erosion rate while the time was normalized with respect to the time at which the cumulative erosion rate was maximum. It was also concluded that the erosion rate between the laboratory model and the field prototype could be correlated if four parameters were known, viz. the maximum erosion rate (from the cumulative erosion rate vs time curve), time to attain this value, incubation period[4] and erosion resistance which is a measure of the relative erosion strength of the material coupled with the severity of the erosion attack. Rao and Buckley [87] also proposed a power law relationship between the cumulative volume erosion rate and the cumulative eroded volume, for mild steel, that could be generated with few experimental points. The paper also summarizes eleven different erosion models proposed by various investigators.

Richman and McNaughton [88] strived to demonstrate the influence of strain based material properties, obtained from cyclic deformation tests, on cavitation damage rate. They analysed the data of a wide range of metals and alloys in Feller and Kharrazi [89] and Knapp[27]

[4] The incubation time or incubation period is defined in ASTM G 32 as 'the initial stage of the erosion rate-time pattern during which the erosion rate is zero or negligible compared to later stages'.

and concluded that good correlation exists between the fatigue strength coefficient, σ_f' [5]and incubation time. The quantity of material removed, expressed in terms of mean depth of penetration, MDP was, however, found to correlate inversely with the product (n'σ_f') where n' is the cyclic strain hardening exponent. They also found that the product (n'σ_f') correlated inversely with the stacking fault energy, SFE, emphasizing the importance of mechanical twinning and also, in certain cases, strain induced phase transformation in improving cavitation erosion resistance.

Bedkowski et al [91] studied the relation between cavitation erosion and fatigue properties of steels. The steels selected for the study were structural steels (10HNAP, 18G2A and 15G2ANb). Uniaxial fatigue tests with random tension/compression loading with zero mean stress was applied on several specimens of these materials at different loads. The dominating frequency of loading was 15 Hz and the limiting frequency of loading was 50 Hz. The loading applied by the fatigue testing machine was controlled through a microcomputer.

The fatigue testing results were expressed, for each material, using regression equations of the form

$$\lg T_{exp} = C_1 - C_2 \lg \sigma_{RMS} \quad \text{----------} \quad (2.14)$$

where C_1 and C_2 are material dependant constants and lg is log to base 10.

---

[5] Basquin's equation [90] describes the high cycle, low strain regime in which the nominal strains are elastic. It is given by

$$\sigma_a = \frac{\Delta\epsilon_e}{2} E = \sigma_f'(2N)^b$$

where σ_a = alternating stress amplitude; $\frac{\Delta\epsilon_e}{2}$ = elastic strain amplitude; E = modulus of elasticity; σ_f' = the fatigue strength coefficient which is defined as the stress intercept at 2N = 1. σ_f' is approximately equal to the true fracture stress.

2N is the number of load reversals to failure, b is the fatigue strength exponent (varies from -0.05 to -0.12 for most metals)

These equations were then normalised with respect to the mean value of the standard deviation σ_{RMS} in the tests and the corresponding value of T_{exp} from the regression equation for each material.

Cavitation was produced using a submerged jet in a Lichtarowicz cell designed in conformance with ASTM G 134. The cumulative erosion rate expressed as the cumulative weight loss divided by the total exposure time was used to quantify the cavitation effect.

The cavitation test results were expressed, for each material, in the form

$$\lg T_{PER} = C_3 - C_4 \lg p_1 \quad \text{----------} \qquad (2.15)$$

where C_3 and C_4 are material dependant constants and p_1 is the jet upstream pressure

These were then normalised with the mean value of the jet upstream pressure, p_1 in the tests and the corresponding value of T_{PER} from the regression equation for each material.

Plot of the normalised equations for both fatigue and cavitation erosion revealed that both phenomena can be expressed by mathematical models of the same type and that a linear relationship exists, on a log log plot, between cavitation erosion and fatigue strength under random loading.

Karimi and Leo [92] formulated a phenomenological model for cavitation erosion rate computation. The model describes the erosion rate as a function of mechanical properties, viz. proof stress, σ_e and rupture stress,σ_R; and metallurgical properties, viz. depth of work hardening, L, coefficient of work hardening, n and power of work hardening, ϑ.

These properties represent the response of the material to cavitation attack and are influenced by the material stacking fault energy which has a strong influence on cavitation erosion resistance.

The model was validated for cavitation generated using a vortex generator in water on duplex stainless steel sample.

The paper may be consulted for the detailed derivation of expressions for the acceleration erosion rate, the steady state erosion rate, the time for the damage rate to become steady and the accumulated mass loss.

Berchiche et al [93] proposed an analytical model to enable prediction of cavitation erosion without model tests or with only limited testing. The material was characterized by its stress-strain relationship and microhardness measurements on a cross section of the eroded sample. The assumptions used in the development of the model were : (i) Loads below the elastic limit have no effect on the erosion produced particularly with regard to fatigue damage (ii) the impacts occur at the same point and during each subsequent impact, after the first, the same amount of energy is absorbed (iii) there is no interaction between adjacent pits on the material surface.

The strain distribution, due to cavitation loading, within the material is expressed as

$$\epsilon(x) = \epsilon_z(1 - \frac{x}{l})^{\theta} \quad \text{----------} \quad (2.16)$$

where ϵ_z = surface strain at the point of impact, l = depth of the hardened layer, θ = shape factor of the strain profile and $\epsilon(x)$ = strain at distance x from the surface.

The thickness of the hardened layer is given by $l = L(\frac{\epsilon_z}{\epsilon_r})^{1/\theta}$ ---------- (2.17)

where ϵ_r = rupture strain, L = maximum thickness of the hardened layer, μm.

The metallurgical parameters used in the model are (i) the maximum depth of hardened layer and (ii) the shape factor of the strain profile, which are determined from microhardness measurements on cross sections of the eroded target.

Pitting tests were done on a sample and the sample analysed by measuring the number of pits produced, co-ordinates of pit centre, diameter of pit and depth of pit. The surface strain for a pit is obtained from the relation

$$h_{max} = l\ \frac{\epsilon_z}{\theta+1} \text{ ----------} \qquad (2.18)$$

where h_{max} = maximum depth of the pit, μm.

The maximum stress is obtained from the stress- strain relationship, which for ductile materials is given by $\sigma = \sigma_e + K\epsilon^n$ where σ_e= elastic limit. For SS316L, n= 0.5, K = 900 MPa, σ_e= 400 MPa. The radial stress distribution in a pit is given by a Gaussian distribution of the form

$$\sigma = \sigma_{max}\left(\frac{\sigma_{max}}{\sigma_e}\right)^{-\frac{r^2}{r_e^2}} \text{ ----------} \qquad (2.19)$$

This is done for all the pits identified on the specimen to get the distribution of loads from the pitting test. It is then applied randomly on the specimen surface until mass loss occurs with only the co-ordinates of the pit centre changed and the pit diameter and impact load remaining the same. The model was validated for SS 316L material and it was observed that while the order of magnitude of the predicted erosion rate was in agreement with the experimental value, the incubation time was under predicted.

Using the experimental results of round robin tests from cavitation erosion testing with a vibratory device, Meged [94] explained the difficulty in accurately measuring the incubation time in erosion tests as well as the large variability in the measurement of the ASTM recommended alternative of nominal incubation time[6]. A new parameter called the erosion

[6] The nominal incubation time, as per ASTM G32, is 'the intercept on the time or exposure axis of the straight-line extension of the maximum-slope portion of the cumulative erosion-time curve'.

threshold time (ETT)[7] was proposed instead of the former parameters and the cumulative erosion time curves, in the initial stage of erosion, modeled using a 2 parameter Weibull cumulative distribution function, $F(t) = 1 - e^{-(\frac{t}{\eta})^{\beta}}$ ---------- (2.20)

where F(t) = fraction failing or cumulative distribution function, η = scale factor or characteristic time, i.e. ETT, and β = shape factor or slope of the Weibull line. The expression was tested using results of Ni 200 tests.

Jayaprakash et al [95] carried out pitting tests on samples of Aluminum alloy, Nickel Aluminum Bronza and Duples stainless steel, using a vibratory device as well as a cavitating jet, and statistically analysed the measured pit characteristics. They concluded that the distribution of pit sizes could be represented by a 3 parameter Weibull distribution of the form

$N = N^{*} e^{-(\frac{D}{D^{*}})^{k}}$ ---------- (2.21)

where N = number of pits of diameter D per unit area per sec, N^{*} = characteristic number of pits per unit area per sec, D = pit diameter, D* = characteristic pit equivalent diameter, k = shape factor of the Weibull curve. D* and N* were representative of the intensity of cavitation and the material properties while k was found to be independent of field/material property.

The diameter of the pit generated is proportional to the collapse pressure intensity and this is reflected in the cumulative number distribution, N(p), of the collapse pressure peaks as functions of pressure peak amplitude is given by a similar Weibull distribution [69],

[7] The erosion threshold time (ETT) is defined as the time required to reach a cumulative mean depth of erosion value of 1 μm.

$N(P) = N^* e^{-(\frac{P}{P^*})^k}$ ---------- (2.22) where N(p) is the cumulative number of peaks with peak height larger than the pressure P, N* is a normalizing parameter for the cumulative number of peaks, P* is a normalizing parameter for peak height, k is a shape parameter.

Szkodo [96] showed that a Weibull distribution is a good representation of the probability of cumulative volume loss due to cavitation erosion. He proposed a relationship of the form

$$V(t) = V\, exp\left\{\frac{H}{h}\ln\left[1 - exp\left(-I\left(\left(\frac{t}{K_c}\right)^{\frac{1}{W_{pl}}}\right)\right)\right]\right\} \quad \text{----------} \quad (2.23)$$

and

$$\frac{dV}{dt} = V(t)\frac{\frac{H}{h}\, I\, t^{\frac{(1-W_{pl})}{W_{pl}}} exp\left(-I\left(\frac{t}{K_c}\right)^{\frac{1}{W_{pl}}}\right)}{W_{pl}K_c^{\frac{1}{W_{pl}}}\left\{1 - exp\left(-I\left(\frac{t}{K_c}\right)^{\frac{1}{W_{pl}}}\right)\right\}} \quad \text{----------} \quad (2.24)$$

where V(t) = cumulative volume loss, dV/dt = cumulative volume loss rate W_{pl} = relative work of plastic deformation on the eroded surface, h = depth of strain hardening, Kc = relative impact toughness of the material, I = relative intensity of cavitation, A= area of the sample, H = depth of the sample, t = time.

The cavitation erosion resistance was expressed in terms of a factor,

$R = \frac{(t_{inc} + t_{vmax})}{v_{max}}$

where t_{inc} = incubation time, t_{vmax} = time at which maximum volume loss rate occurs and v_{max} = maximum volume loss rate.

Hattori and Maeda [97] proposed a logistic model to express the progress of cavitation erosion in metallic materials. The model assumed that the volume loss rate can be expressed by a logistic curve as

$\frac{du}{dt} = \alpha u - \frac{\beta}{F} u^2$ ---------- (2.25)

where u = volume loss rate, mm^3/h, α = multiplication factor in pit number per unit time (representing the increase of pitting rate), h^{-1}; β = factor representing the annihilation of pit number per unit time , $1/\mu$

The change in MDE was expressed as $d = \frac{\alpha}{\beta} t - \frac{1}{\beta} ln \frac{(1+c)}{(1+ce^{-\alpha t})}$ ---------- (2.26)

Where d = mean depth of erosion (MDE), t = exposure time, c = constant = $\frac{\alpha}{\beta} \frac{1}{u_0} - 1$ where u_0 = u(0) is the initial condition.

The model was validated for a range of materials, viz. pure aluminum, pure copper, carbon steels, carbon tool steels, cast iron, stainless steels, stainless cast steel and cobalt alloy, using a vibratory apparatus with stationary specimen in deionized water at 25°C. The paper gives detailed equations for obtaining α, β and c from the experimental results.

It is seen from the preceding paragraphs that although there have been considerable efforts to develop simple relationships between cavitation damage and easily measured / available material properties, these efforts have seen limited success because of the complex nature of the phenomenon and the synergistic effect of material and liquid properties and flow conditions on the damage produced.

2.4 SOME CAVITATION DAMAGE STUDIES IN LIQUID METALS

Cavitation studies in liquid metals started in the 1950s in response to the need to design high temperature compact centrifugal pumps for handling sodium and sodium-potassium alloy. The need arose to meet the requirements of aircraft nuclear power plant project and space nuclear power plants (SNAP systems) [98]. In these systems the primary objective of realizing compact systems makes operation with limited cavitation unavoidable; however, the equally

important compulsion to achieve long, unattended life motivated fundamental and applied studies on cavitation damage of materials / hydraulic machinery in liquid metals.

In the 1960s and 1970s testing for evaluation of cavitation damage was carried out extensively, for applications in the space and nuclear industry, particularly at the University of Michigan, Ann Arbor under Prof. Hammitt and by Thiruvengadam et al on contract to NASA. Using results of experiments in vibratory device [62, 63] on a wide range of materials such as SS304, SS316 etc. (refer Table 1 of [39]) in different liquids such as water, Hg, Pb-Bi alloy and Li at various temperatures ranging from room temperature to 815°C for Pb-Bi and Li, Hammitt and co-workers attempted to establish a correlation between damage rate and fluid properties. Although several mechanical properties like tensile strength, yield strength, engineering strain energy, true strain energy, hardness, elongation, reduction in area and elastic modulus were considered, both individually and in different combinations, it was observed that a reasonably precise and simple formulation was difficult, except for small subsets of the data. A reasonable correlation was, however, possible when the damage rate was related to the ultimate resilience (α $UR^{-1/2}$) . When fluid properties were also considered, a satisfactory correlation was obtained between the damage rate and a combination of ultimate resilience and liquid density. With data from a venturi system, using mercury and water at room temperature, it was observed that while the damage rate in mercury correlated with the ultimate resilience, as for the vibratory test data, the correlation between damage rate and ultimate resilience for water was unsatisfactory. This was attributed to the dominant effect of chemical oxidative corrosion (which is not considered in the correlation), over mechanical damage, in the low intensity venturi system.

Preiser et al [64] carried out tests on a vibratory cavitation device in liquid sodium at 205°C for pure iron, 201 nickel, 316 stainless steel, Inconel 600 and 100A titanium and obtained

the variation of the weight loss rate with time for the materials. The reciprocal of the volume loss rate was observed to correlate reasonable well with the strain energy of the materials tested. It was also concluded from the tests that the intensity of cavitation damage in sodium at 205°C was about 1.5 times greater than that in water at 27°C. Moreover, the rate of cavitation damage in sodium increases initially with temperature and then decreases.

Young and Freche [99], measuring the cavitation erosion rate (expressed in terms of volume eroded per unit time) in liquid sodium, showed that while the strain energy correlated well with the measured erosion rate of materials such as AISI 316, A-286, Inconel 600, Hastelloy X, L-605, it was a poor correlation parameter for the erosion rate of Stellite 6B.

Young and Johnston [100] studied the effect of cover gas pressure (in the range 1 atmpshere to 4 atmospheres) on the cavitation damage of L-605, Stellite 6B and AISI 316 stainless steel in liquid sodium at 427°C using a vibratory device (at 25 kHz and 45 μ P-P displacement). It was also reported that the steady state volume loss rate (based on the total specimen area) increased linearly with increase in the cover gas pressure with Stellite 6B having the maximum resistance to damage and SS 316 the least resistance to damage.

Dayer [23] tested austenitic stainless steel SS 316 and stabilized steel SS 321 in sodium at various temperatures using a vibratory cavitation device (operated at 15.5 kHz with P-P displacement of 25 μ). His results showed that the cavitation damage rate was measurably higher in the temperature range 200°C – 300°C than at higher temperatures. It is also reported that the erosion resistance of SS 321 is marginally lower than that of SS 316. Hammitt and Courbiere [10] reported that the maximum damage temperature for SS 316 was in the range

200°C – 400°C, based on tests done at CEA, Cadarache and three laboratories in the USA (viz. Hydronautics, Inc, NASA and University of Michigan).

In addition to the macroscopic mechanical properties discussed in the preceding paragraphs such as yield strength, ultimate tensile strength, hardness, strain energy etc., it is observed that microscopic properties such as stacking fault energy and fracture toughness coefficient (K_{IC}) influence the damage produced.

2.5 RELEVANCE OF THE WORK IN THE THESIS

It is evident from the above survey of literature in the area of cavitation damage that damage prediction is still a challenging task. Cavitation damage in liquid metals such as sodium is even more insidious than in water and therefore experimental work in sodium itself is desirable for a comprehensive understanding of the problem. This is underlined by the complex nature of the phenomenon which is the result of the interplay of a number of fluid and material properties (both macroscopic and microscopic).

Combating cavitation damage requires effort not only in hydraulic design but also in material selection, enhancement of damage resistance by hardfacing, surface treatment etc.

A systematic study of the cavitation damage resistance in sodium of the common fast reactor structural material (austenitic stainless steel) including the effect of hardfacing (with Ni and Co based alloys) is of practical value. The work discussed in the thesis is an effort in this direction and attempts to explain the difference in wear resistance in terms of microscopic properties ,such as fracture toughness and stacking fault energy, in contrast to common explanations in terms of macroscopic properties such as hardness, ultimate tensile strength etc.

CHAPTER 3

THEORETICAL ESTIMATION OF SINGLE BUBBLE COLLAPSE PRESSURE

CHAPTER 3 – THEORETICAL ESTIMATION OF SINGLE BUBBLE COLLAPSE PRESSURE

3.0 INTRODUCTION

This chapter discusses solution of the equations for bubble collapse. The equation for bubble collapse is solved both for the incompressible case (Rayleigh Plesset (RP) equation) and the compressible case (Gilmore equation) to estimate the jet velocity[1] at the end of collapse and the subsequent pressure exerted on the solid boundary to produce damage. The equations are also used to estimate the jet velocities and pressures in liquid sodium vis-à-vis that in water.

Cavitation damage of a solid surface results when a bubble containing a mixture of vapor and gas collapses adjacent to the surface. An estimation of the magnitude of the collapse pressure can be obtained by solving the equations governing bubble collapse. In these equations the pressure generated due to the collapse of a single bubble is investigated. In reality, however, there will be a population of bubbles in the cavitation zone and the resultant damage produced

[1] In this chapter the bubble wall velocity and pressure resulting from the symmetrical collapse of a single bubble in an infinite medium is computed. The term **jet velocity** used in this chapter is actually the **bubble wall velocity** obtained from solution of the equations (RP or Gilmore equations). It is to be noted that in reality a jet is formed only during the asymmetrical collapse of a bubble (i.e in the case of collapse of a bubble adjacent to a solid boundary or in the presence of longitudinal pressure gradient or in the final stages of collapse [44]). However, since the bubble wall velocity has a direct bearing on the magnitude of the velocity of jet formed at the end of collapse, the term jet velocity is used in this chapter.

will be affected by (i) the concerted collapse of bubbles wherein the pressure generated due to the collapse of a specific bubble produces the collapse of adjacent bubbles (ii) the cushioning effect of surrounding bubbles on the pressure transmitted through the liquid on to the surface. Single bubble collapse pressure calculation is nevertheless useful in understanding the bubble collapse mechanism and providing an estimate of the magnitude of the damage pressure.

3.1 EQUATIONS OF BUBBLE COLLAPSE

As mentioned in Sec. 2.1.1, the theoretical treatment of cavitation invariably begins with the equations of bubble collapse formulated by Rayleigh [26]. Sec. 2.1.1 gives the various equations that express the variation of bubbles radius with time under different approximations. This section and the following two sections discusses in greater detail the Rayleigh Plesset equation (which neglects liquid compressibility) and the Gilmore equation (which accounts for the effects of compressibility in the final stages of bubble collapse). These equations are used later on in the chapter to compute the collapse pressure resulting from bubble implosion.

Rayleigh considered the symmetrical collapse of an empty spherical cavity in an infinite body of incompressible liquid under constant pressure. Equating the work done on the system (i.e. liquid and empty cavity) by the constant external pressure to the kinetic energy (KE) gained by the liquid, the expression for the velocity of the cavity wall was obtained

$$U^2 = \frac{2P}{3\rho}\left(\frac{R_0^3}{R^3} - 1\right) \qquad \text{---------- (3.1)}$$

where ρ = density of the liquid, R = bubble radius at any instant of time, R_0 = initial bubble radius, P = pressure at infinity driving collapse, U = bubble wall velocity = $\frac{dR}{dt}$. Equation (3.1) shows an unlimited increase of velocity as R -> 0. Rayleigh was aware of the problem and resolved the issue by explaining that in reality there will be insoluble gas in the cavity.

Considering the isothermal compression of the gas in the cavity and equating the work done on the system (i.e. liquid and gas filled cavity) to the sum of the KE of the liquid and the work done in compressing the gas, the equation becomes

$$U^2 = \frac{2P}{3\rho}\left(\frac{R_0^3}{R^3} - 1\right) - \frac{2Q}{\rho}\frac{R_0^3}{R^3} ln \frac{R_0}{R} \qquad \text{---------- (3.2)}$$

where Q = initial pressure within the bubble.

From the above equation, U=0 when $P(1-z) + Q \ln z = 0$ ---------- (3.3) where

$z = (R/R_o)^3$

In reality, however, the compression process is extremely rapid and therefore an adiabatic compression process is a better approximation than an isothermal compression process.

3.1.1 Rayleigh Plesset equation

Consider a bubble with initial equilibrium radius R_e containing a mixture of gas and vapor at a pressure P_{g0} in a liquid at hydrostatic pressure P_0. In the event of a momentary increase in the pressure from $P_{\infty 0}$ to P_∞ (due to an acoustic wave, step change in pressure etc.), the bubble collapses from R_e to R. During this collapse of the bubble, the pressure driving the collapse P_0 increases by the liquid surface tension ($2\sigma/R$). Simultaneously, the bubble collapse is opposed by the increase in pressure of the bubble contents (from P_{g0} to P_g) which are compressed adiabatically. The work done by the external pressure on the liquid is equal to the sum of the kinetic energy (KE) of the liquid and the work done in compressing the bubble contents. For an infinitesimal change in volume,

The work done by the external pressure, $WD_{liquid} = - \int_{R_e}^{R} \left(P_\infty + \frac{2\sigma}{R} \right) dV$

$$= \frac{4\pi}{3} \left(P_\infty + \frac{2\sigma}{R}\right)(R_e^3 - R^3) \qquad \text{---------- (3.4)}$$

The work done in compressing the bubble contents, $WD_{gas} = -\int_{R_e}^{R} P_g \, dV$

$$= \frac{4\pi}{3}(P_g)(R_e^3 - R^3) \qquad \text{---------- (3.5)}$$

KE of the liquid outside the bubble, $KE_{liq} = \int_R^\infty \frac{1}{2}(4\pi r^2)dr.\rho.(\frac{dr}{dt})^2$ ---------- (3.6)

where r is the instantaneous radius of the bubble.

For an incompressible liquid, $R^2 \frac{dR}{dt} = r^2 \frac{dr}{dt}$

$$\text{Hence} \quad \frac{dr}{dt} = \frac{R^2}{r^2}\frac{dR}{dt} \qquad \text{---------- (3.7)}$$

$$u = \frac{R^2}{r^2}\dot{R}$$

Substituting (7) in (6) and simplifying gives

$$KE_{liq} = 2\pi\rho \int_R^\infty r^2 \frac{R^4}{r^4}.(\frac{dr}{dt})^2 \, dr$$

$$= 2\pi\rho R^4(\frac{dR}{dt})^2 \int_R^\infty \frac{1}{r^2}.dr$$

$$= 2\pi\rho R^3(\frac{dR}{dt})^2 = \frac{1}{2}m_{eff}U^2 \qquad \text{---------- (3.8)}$$ where $U = \frac{dR}{dt}$ is the bubble wall velocity

and $m_{eff} = 3\,(\frac{4}{3}\pi R^3\rho)$ is the effective mass of the liquid.

Since the work done by the external pressure on the liquid is equal to the sum of the kinetic energy (KE) of the liquid and the work done in compressing the bubble contents

$$\frac{4\pi}{3}(P_\infty + \frac{2\sigma}{R})(R_e^3 - R^3) = \frac{4\pi}{3}(P_g)(R_e^3 - R^3) + 2\pi\rho R^3(\frac{dR}{dt})^2$$

Differentiating the above expression

$$\frac{4\pi}{3}(P_\infty + \frac{2\sigma}{R})(-3R^2\dot{R}) = \frac{4\pi}{3}(P_g)(-3R^2\dot{R}) + 2\pi\rho 3R^2\dot{R}^3 + 2\pi\rho R^3\, 2\dot{R}\ddot{R}$$

Dividing throughout by $2\pi\rho R^2\dot{R}$

$$\frac{2}{\rho}\left[P_g - P_\infty - \frac{2\sigma}{R}\right] = 3\dot{R}^2 + 2R\ddot{R}$$

i.e $$R\ddot{R} + \frac{3}{2}\dot{R}^2 = \frac{1}{\rho}\left[P_g - P_\infty - \frac{2\sigma}{R}\right]$$ ---------- (3.9)

$$= \frac{1}{\rho}\left[P_L(t) - P_\infty(t)\right]$$ ---------- (3.10)

where P_L is the pressure in the liquid at the bubble wall = $P_g - \frac{2\sigma}{R}$

P_g is the pressure of vapor and gas inside the bubble. $P_g = P_{vp} + P_{g0}(\frac{R_e}{R})^{3\gamma}$ (where γ is the ratio of specific heats of the gas),

P_{g0} is the initial gas pressure inside the bubble. $P_{g0} = P_{\infty 0} + \frac{2\sigma}{R} - P_{vp}$ and $P_\infty = P_{\infty 0} + P_a$ where P_{vp} is the vapor pressure of the liquid and P_a is the change in pressure (eg. a step change or a sinusoidal change in pressure).

When the liquid viscosity is also considered the pressure in the liquid at the cavity interface, P_L is given by

$$P_L + \frac{2\sigma}{R} - 2\mu\frac{\partial u}{\partial r}\Big]_{\text{at r =R}} = P_g \quad \text{where u} = \frac{dr}{dt}$$ ---------- (3.11)

From equation (7), $\frac{\partial u}{\partial r} = -\frac{2R^2}{r^3}\dot{R}\Big]_{\text{at r =R}}$

$$= -\frac{2\dot{R}}{R}$$

Therefore $P_L = P_g - \frac{2\sigma}{R} - 4\mu\frac{\dot{R}}{R}$ ---------- (3.12)

Substituting for P_L in equation (10) gives the well known Rayleigh Plesset (RP) (or Rayleigh Plesset Noltingk Neppiras Poritsky (RPNNP)) equation (3.13) [32,33,34,101]

$$R\ddot{R} + \frac{3}{2}\dot{R}^2 = \frac{1}{\rho}\left[P_g(t) - \frac{2\sigma}{R} - 4\mu\frac{\dot{R}}{R} - P_\infty(t)\right]$$

$$R\ddot{R} + \frac{3}{2}\dot{R}^2 = \frac{1}{\rho}\left[P_{vp} + P_{g0}(\frac{R_e}{R})^{3\gamma} - \frac{2\sigma}{R} - 4\mu\frac{\dot{R}}{R} - P_\infty(t)\right] \quad \text{---------- (3.13)}$$

This equation is identical to equation (2.3).

Solving equation (3.13) the variation of bubble radius with time can be obtained for an imposed pressure variation $P_\infty(t)$. The pressure in the liquid at the bubble interface at any point of time during bubble collapse can be obtained from equation (3.12).

The above equation (3.13) is derived with the following assumptions (i) the bubble is spherical during the entire collapse process (ii) the liquid is incompressible (iii) no body forces exist (iv) the conditions within the bubble are spatially uniform (v) the gas content in the bubble is constant. Equation (3.13) is normally applicable when the bubble wall velocity is < 1/5 of the velocity of sound.

3.1.2 Gilmore equation

In reality, however, the collapse of a bubble is rapid and liquid compressibility is to be considered. Among other forms of the above equation which take into account the effect of liquid compressibility, the simplest formulation is the acoustic approximation [35]. In this formulation all pressure disturbances are considered to propagate with the speed of sound which is constant. This limits the use of the equation to cases where the bubble wall velocity is small compared to the speed of sound (M = $\frac{\dot{R}}{c}$ << 1). The loss of energy due to sound radiation is considered in this analysis. The acoustic approximation equation (i.e equation 2.4) is reproduced below

$$R\ddot{R} + \frac{3}{2}\dot{R}^2 = \frac{1}{\rho}\left\{P_L + \frac{R}{c}\left(1 - \frac{\dot{R}}{c}\right)\frac{dP_L}{dt} - P_\infty(t)\right\} \quad \text{---------- (3.14)}$$

Another approximation that considers a more satisfactory description of the energy loss through compression of the liquid and sound radiation is the Herring [36] approximation (i.e. equation 2.5) which is reproduced below

$$\left(1-\frac{2\dot{R}}{c}\right)R\ddot{R}+\frac{3}{2}\left(1-\frac{\dot{4R}}{3c}\right)\dot{R}^2=\frac{1}{\rho}\left\{P_L+\frac{R}{c}\left(1-\frac{\dot{R}}{c}\right)\frac{dP_L}{dt}-P_\infty(t)\right\} \quad \text{---------- (3.15)}$$

Under conditions involving the rapid collapse of transient bubbles the bubble wall velocity often exceeds the velocity of sound in the liquid producing shock waves. Gilmore [37] used the Kirkwood-Bethe hypothesis, which states that pressure disturbances are propagated outward with a velocity equal to the sum of the sound velocity and the liquid velocity (i.e the quantity $r\left(h+\frac{U^2}{2}\right)$ is propagated outward along a path traced by a point moving with (C+U) where h is the enthalpy difference between the liquid at pressure P and the liquid at pressure P_∞, C is the local sound velocity and U is the local liquid velocity, to develop the following equation

$$\left(1-\frac{\dot{R}}{c}\right)R\ddot{R}+\frac{3}{2}\left(1-\frac{\dot{R}}{3c}\right)\dot{R}^2=\left(1+\frac{\dot{R}}{c}\right)H+\frac{R}{c}\left(1-\frac{\dot{R}}{c}\right)\frac{dH}{dt} \quad \text{---------- (3.16)}$$

Equation (3.16) is known as the Gilmore's equation (i.e. equation 2.6).

The pressure in the liquid at the bubble interface, P_L is specified as a function of t or R and H and C are related to P_L using an equation of state for liquids. For most liquids the pressure-density curve for adiabatic compression can be expressed using the relation known as Tait's equation of state [37, 102] viz. $\frac{p+B}{P_\infty+B}=\left(\frac{\rho}{\rho_\infty}\right)^n$ ---------- (3.17)

where ρ = density of the liquid, p = pressure of the liquid, n = index, subscript ∞ refers to the pressure and velocity at infinite distance from the bubble (normal condition).

For water B = 3000 atm = $3*10^8$ N/m^{2}and n = 7 [102]

The quantity, nB = compressibility coefficient = $\frac{1}{\rho}\frac{d\rho}{dp}$ [102]

The liquid enthalpy is given by the expression [103], H = $\int_{P_\infty}^{P_L}\frac{dp}{\rho}$ ---------- (3.18)

From equation (3.17), $\rho = \left(\frac{p+B}{p_\infty + B}\right)^{\frac{1}{n}}\rho_\infty$.

Sub for ρ in (3.18), H = $\frac{A^{\frac{1}{n}}}{\rho_\infty}\int_{P_\infty}^{P_L}(p+B)^{\frac{-1}{n}}\,dp$

$$H = \frac{n}{n-1}\frac{A^{\frac{1}{n}}}{\rho_\infty}\left((P_L+B)^{\frac{n-1}{n}} - (P_\infty + B)^{\frac{n-1}{n}}\right) \quad \text{---------- (3.19)}$$

where A = P_∞ + B = 3001 atm. and P_∞ is the pressure in the liquid at infinity.

P_L = pressure in the liquid at the bubble wall = $P_{vp} + P_{g0}(\frac{R_e}{R})^{3\gamma} - \frac{2\sigma}{R} - 4\mu\frac{\dot{R}}{R}$

The local velocity of sound in the liquid [103], C = $\sqrt{\frac{\partial p}{\partial \rho}}$ ---------- (3.20)

Using equation (3.17), $C^2 = \frac{\partial p}{\partial \rho} = \frac{(P_\infty + B)\,n\,\rho^{n-1}}{\rho_\infty^n}$

$$= (P_\infty + B)\,(\frac{\rho}{\rho_\infty})^{n-1}(\frac{n}{\rho_\infty})$$

$$= C_0^2(\frac{\rho}{\rho_\infty})^{n-1} \quad \text{---------- (3.21) where}$$

$C_0^2 = (P_\infty + B)\,(\frac{n}{\rho_\infty})$ ---------- (3.22) is the absolute velocity of sound in the liquid.

The expression for liquid enthalpy can also be written in terms of the absolute velocity of sound in the liquid and the local and absolute liquid densities.

Using equation (3.18), H = $\int_{P_\infty}^{P_L}\frac{dp}{\rho}$

Substituting for dp from equation (3.21)

$$H = \int_{\rho_\infty}^{\rho} C_0^2 \left(\frac{\rho}{\rho_\infty}\right)^{n-1} \frac{\partial \rho}{\rho}$$

$$= \frac{C_0^2}{n-1} \left[\left(\frac{\rho}{\rho_\infty}\right)^{n-1} - 1\right] \quad \text{---------- (3.23)}$$

Substituting for $\left(\frac{\rho}{\rho_\infty}\right)^{n-1}$,from equation (3.21), in equation (3.23), we get $H = \frac{C^2 - C_0^2}{(n-1)}$.

Therefore, $C = (C_0^2 + (n-1)H)^{\frac{1}{2}}$ ---------- (3.24)

In the case of an sinusoidally varying externally applied pressure field (as for acoustic cavitation) the pressure P_∞ is given by $P_\infty = P_0 - P_a \sin(\omega t)$, where P_0 is the normal (atmospheric) pressure and P_a is the amplitude of the imposed field and ω is its angular frequency.

3.1.2.1 Estimation of pressure due to bubble collapse from shock waves

During collapse of a bubble the pressure at the interface can attain extremely large values radiating spherical waves which are converted into shock waves as they propagate through the liquid. According to the Kirkwood Bethe hypothesis in the case of spherical waves of finite amplitude the quantity $r\varphi$ propagates with a velocity C' = C + U where C is the local velocity of sound in the liquid and U is the local liquid velocity. In addition to this the quantity G = r $\frac{\partial \phi}{\partial t}$ also propagates with velocity C'. It is seen from the continuity equation and the equation of motion [103] that $\frac{\partial \phi}{\partial t} = h + \frac{u^2}{2}$.

Therefore, G(r,t) = r $(h + \frac{u^2}{2})$ ---------- (3.25).

The quantity G is propagated with velocity C'. Hence if the value of G(R, t_R) is known at the surface of a radiating sphere of radius R at time t_R , its value at any other radius r can be determined from the condition G(R, t_R) = G(r, t) where $t = t_R + \int_R^r \frac{dr}{C'}$

From equation (3.24) it may be concluded that

$G(R, t_R) = R\left(H + \frac{U^2}{2}\right)$ ---------- (3.26)

where H and U are obtained from the solution of equation (3.16). The value of G at any point r in the liquid is determined by the value of the pressure p at that point.

The value of the pressure P at any point r is given by the equation [103]

$$P = A\left[\frac{2}{n+1} + \frac{n-1}{n+1}\left(1 + \frac{n+1}{rC_0^2}G\right)^{1/2}\right]^{\frac{2n}{n+1}} - B \quad \text{---------- (3.27)}$$

where $A = P_0 + B = 3001$ atm.

The time of propagation of the spherical wave is given by [103]

$$t = t_R + \frac{2G}{C_0^2}\left[\frac{1+2\beta u}{\beta u(1+\beta u)} - \frac{1+2\beta U}{\beta U(1+\beta U)} - 2\ln\frac{(1+2\beta u)\beta U}{\beta u(1+\beta U)}\right] \quad \text{---------- (3.28)}$$

where $\beta u = \frac{1}{2}\left[\left(1 + \frac{n+1}{rC_0^2}G\right)^{\frac{1}{2}} - 1\right]$ and $\beta U = \frac{1}{2}\left[\left(1 + \frac{n+1}{rR}G\right)^{\frac{1}{2}} - 1\right]$

Gilmore's equation (3.16) is solved simultaneously with equations (3.19) and (3.24) to obtain the variation of bubble radius with time for an imposed external pressure, $P_\infty(t)$. Equation (3.27) is then used to obtain the variation of the pressure in the liquid with radius.

As Gilmore's solution accounts for the compressibility of the liquid, it is generally used when the ratio of the maximum bubble size to the equilibrium size is >10 [104]

Programs were developed to solve Rayleigh Plesset (RP) equation (equation 3.13) and Gilmore's equation (equation 3.16).

3.1.2.2 Estimation of pressure due to impingement of liquid jet

In the case of a bubble collapsing on a solid surface the jet of liquid produced from the collapsing bubble impinges on the surface directly and produces damage. The jet velocity is obtained by solution of the Gilmore equation (or RP equation for the case of incompressible liquid). It is assumed that at the instant the liquid jet comes into contact with the solid surface the kinetic energy of each particle of the jet is converted to elastic deformation of the same particle as determined by the bulk modulus of elasticity of the liquid. The instantaneous pressure P' on the solid surface is then obtained using the relation [26, 27]

$$\frac{P\prime^2}{2E} = \frac{1}{2}\rho U^2 \quad \text{---------- (3.29)}$$

where

P' = instantaneous pressure on the solid surface, Pa; E = modulus of elasticity of sodium (water), Pa; U = jet velocity at the end of bubble collapse, m/s

3.2 VALIDATION OF CODE

The code for numerical solution of RP and Gilmore equations were validated using available literature.

(i) Validation of RP code

The code for solving RP equation was validated using published literature [103]. The equation was solved for the following conditions : Ro = equilibrium bubble size of air bubble

= 1 μm, $\frac{dR}{dt}_{t=0} = 0$, acoustic frequency = 500 kHz, acoustic amplitude, P_a = 2*10^5 Pa to 40*10^5 Pa. The variation in the radius of the bubble is in agreement with [103]. Fig. 3.1 (a) shows the results in [103] and Fig. 3.1 (b) shows the results obtained from the code

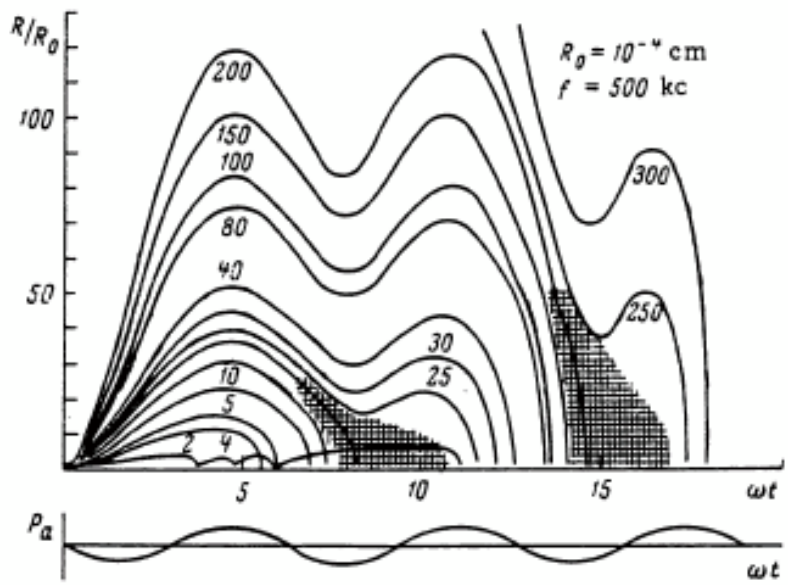

Fig. 3.1(a) – Variation of bubble radius with time from solution of RP equation (R_0 = 1μm, P_a = 2*10^5 Pa to 40*10^5 Pa, f = 500 kHz) [103]

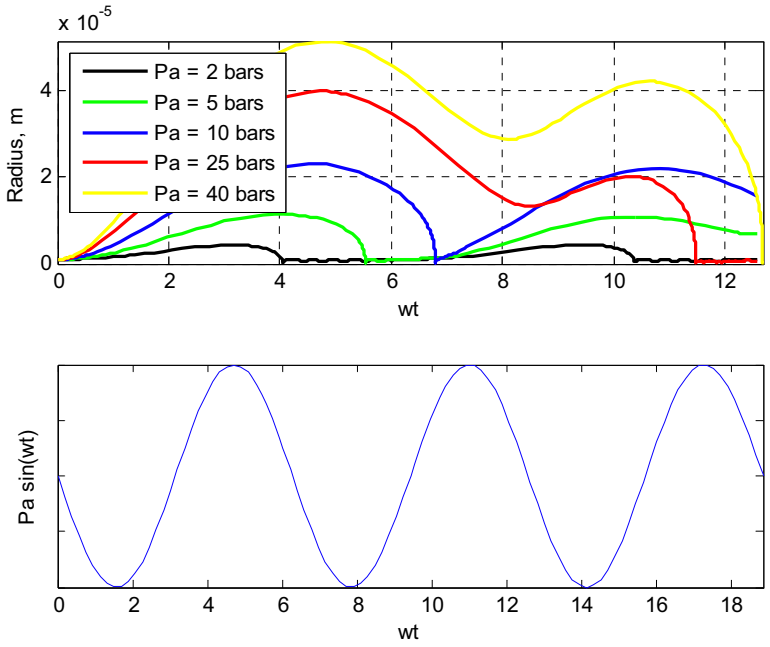

Fig. 3.1 (b) - Variation of bubble radius with time for various acoustic pressure amplitudes (R_0 = 1μm, P_a = 2*10^5 Pa to 40*10^5 Pa, f = 500 kHz) from code

(ii) Validation of Gilmore equation code

The code developed for solving Gilmore equation (equation 3.16) was validated using published data [103]. The equation was solved for the following conditions : Ro = equilibrium bubble size of air bubble = 1μm, acoustic frequency = 500 kHz, acoustic amplitude, P_a = 5*10^5 Pa.

The values of the constant 'B' and the index 'n' for water in Tait's equation of state (equation (3.17) $\frac{p+B}{P_\infty + B} = \left(\frac{\rho}{\rho_\infty}\right)^n$ where ρ = density of the liquid, p = pressure of the liquid, subscript ∞ refers to the condition far away from the bubble and $P_\infty = P_0 - P_a \sin(\omega t)$ and P_0 is the normal (atmospheric) pressure.

B = 3000 atm = $3*10^8$ $N/m^2$and n = 7 [103] .

The variation in the radius of the bubble from [103] is shown in Fig. 3.4(a) while Fig. 3.4(b) below shows the bubble size variation obtained from the code.

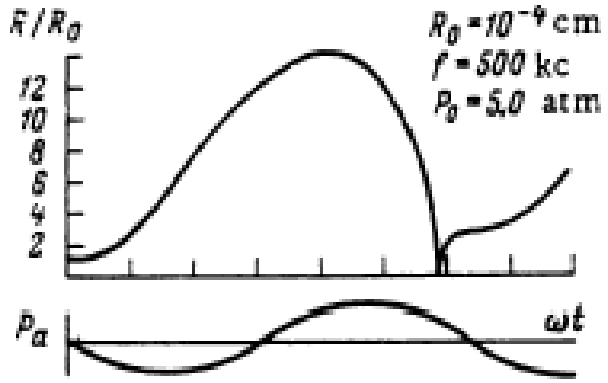

Fig. 3.2(a) – Variation of bubble radius from solution of Gilmore's equation (R_0 = 1μm, P_a = $5*10^5$ Pa, f = 500 kHz) [103]

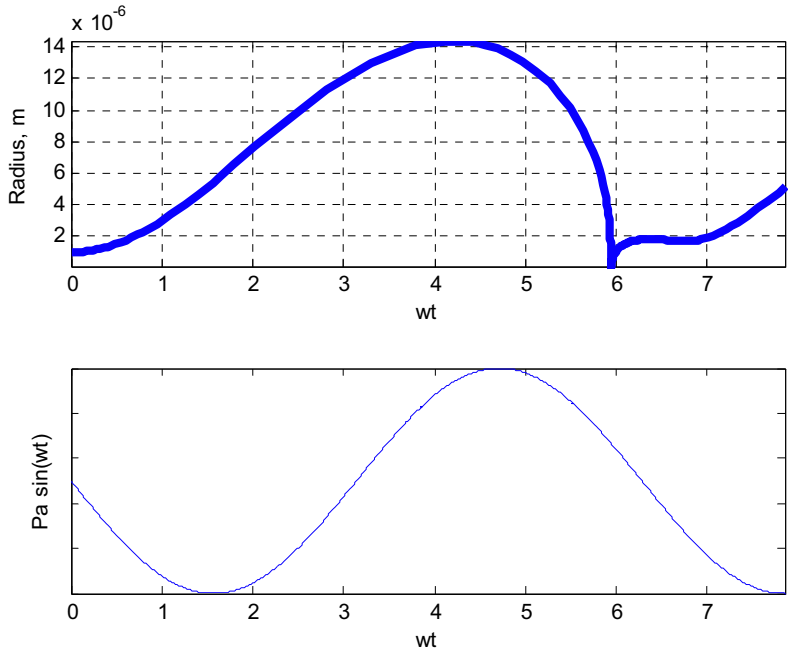

Fig. 3.2(b) – Variation of bubble radius from solution of Gilmore's equation (R_0 = 1μm, P_a = $5*10^5$ Pa, f = 500 kHz) from code

3.3 EFFECT OF COMPRESSIBILITY ON JET VELOCITY

The liquid jet produced at the end of asymmetrical collapse of a bubble attached to a surface produces erosion of the surface. Liquid compressibility reduces the bubble wall velocity at the end of collapse. In order to understand the effect of compressibility on the velocity of the jet the Gilmore equation is used. The velocity of the jet is computed first using the RP equation and then using Gilmore's equation for the following conditions.

According to Flynn [35] the upper limit on the size of free nuclei in water is $2*10^{-2}$ cm (200 μm) whereas the size of free nuclei in fresh drawn tap water that is allowed to stand for a few seconds is $5*10^{-3}$ cm (50 μm).

Assuming an initial bubble size of 200 μm (i.e R_0 = 200 μm) and $\frac{dR}{dt}_{t=0} = 0$ in water at 293 K, the bubble variation is first computed assuming incompressible liquid (i.e solving RP equation – 3.13) and then taking into account the effect of liquid compressibility in the final stages of bubble collapse (i.e using Gilmore's equation – 31.6)

In vibratory cavitation the horn vibrates at a frequency, ω = 20kHz with peak to peak amplitude of 25μm.

For water at 293K - vapor pressure = 2200 Pa, density = 998 kg/m^3, surface tension = 0.072 N/m, viscosity = 0.0018Pa-s, acoustic amplitude, P_a[2] = 23.237*10^5, frequency of horn = ω = 2*π*20000, atmospheric pressure, P_{atm} = 1*10^5 , speed of sound in water, C_0 = 1482 m/s, compressibility, β = 4.6*10^{-10} m^2/N [105], modulus of elasticity, E = 1/β = 2.17*10^9 N/m^2. The constants A, B and n in Tait's equation of state are A = 3001*10^5 N/m^2, B = 3000*10^5 N/m^2, and n = 7 [103].

Fig. 3.3 below shows the comparison of bubble radius variation assuming incompressible liquid with that taking into account the effect of liquid compressibility and Table 3.1 summarises the results.

[2] In vibratory cavitation, the horn vibrates at a frequency, ω = 20kHz with peak to peak amplitude of 25mm. The applied pressure is a sinusoidal wave Pa sin(ωt), The acoustic amplitude Pa = ρ V C_0 . The velocity V = A ω where A = peak- peak amplitude / 2 = 25*10^{-6} / 2 = 12.5*10^{-6} m and ω = 2*p*20000 = 125.67*10^3, C_0 = speed of sound in water = 1482 m/s for water

Therefore, Pa = ρ V C_0 = 998.2 * (125.67*10^3*12.5*10^{-6}) * 1482 = 23.237*10^5 Pa.

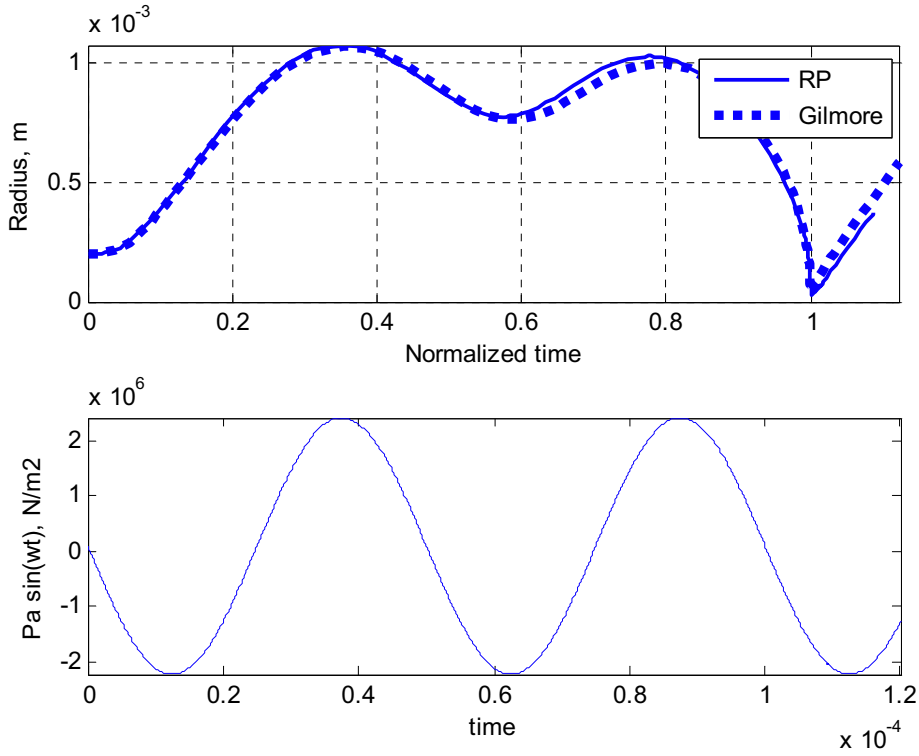

Fig. 3.3 – Variation of bubble radius with time in water assuming incompressible liquid (R-P equation) and taking into account the effect of compressibility (Gilmore's equation)

Table 3.1– Calculated collapse pressure in water

Initial conditions	**Parameter**	**RP equation (3.13)**	**Gilmore equation (3.16)**
Water at 293K, R_0 = 200 μm and $\frac{dR}{dt}_{t=0} = 0$	R_{max}	1.07 mm	1.07 mm
	R_{min}	0.0246 mm	0.0352 mm
	Max jet velocity	1365 m/s	741 m/s
	Collapse pressure, MPa	2010	1090

3.4 COLLAPSE OF VAPOR BUBBLE IN LIQUID SODIUM

Assuming an initial bubble size of 200 μm (i.e R_0 = 200 μm) and $\frac{dR}{dt}_{t=0} = 0$ in water at 293 K, the bubble variation is first computed assuming incompressible liquid (i.e solving RP equation – 3.13) and then taking into account the effect of liquid compressibility in the final stages of bubble collapse (i.e using Gilmore's equation – 3.16).

For sodium at 400ºC the properties are [106] – vapor pressure = 78.2 Pa, density = 858 kg/m^3, surface tension = 0.169 N/m, viscosity = 2.79*10^{-4} Pa-s, surface tension = 0.169 N/m); adiabatic compressibility of liquid sodium, β_0 , at 400 ºC, is 2.09*10^{-10} m^2/N, modulus of elasticity, E = 1/β = 4.79*10^9 N/m^2.

In vibratory cavitation, the horn vibrates at a frequency, ω = 20 kHz, with peak to peak amplitude of 25μm.

The operating parameters are : acoustic amplitude[3], P_a = 31,8*10^5 Pa, frequency of horn = ω = 2*π*20000, atmospheric pressure, P_{atm} = 1*10^5 , speed of sound in sodium, C_0 = 2361 m/s. The index 'n' for liquid sodium in Tait's equation of state (3.17) is, from [107], n = 4.002,

The constant B = $\frac{1}{n\beta_0}$ [102]. B = $\frac{1}{4.002(\ 2.09*10^{-10}\ )}$ = 1.196*10^9 N/m^2

[3] In vibratory cavitation, the horn vibrates at a frequency, ω = 20kHz with peak to peak amplitude of 25mm. The applied pressure is a sinusoidal wave Pa sin(ωt), The acoustic amplitude, $P_a = \rho V C_0$. The velocity V = A ω where A = peak- peak amplitude / 2 = 25*10^{-6} / 2 = 12.5*10^{-6} m, and ω = 2*π*20000 = 125.67*10^3, C_0= speed of sound in sodium =2361 m/s in sodium at 400ºC

Therefore, $P_a = \rho V C_0$ =858 *(125.67*10^3*12.5*10^{-6}) * 2361 = 31.8*10^5 Pa.

Speed of sound in liquid sodium [106], $C_0 = \sqrt{\frac{1}{\rho\beta_0}} = \sqrt{\frac{1}{858*2.09*10^{-10}}} = 2361$ m/s

Fig. 3.4 below shows the comparison of bubble radius variation assuming incompressible liquid with that taking into account the effect of liquid compressibility and Table 3.2 summarises the results.

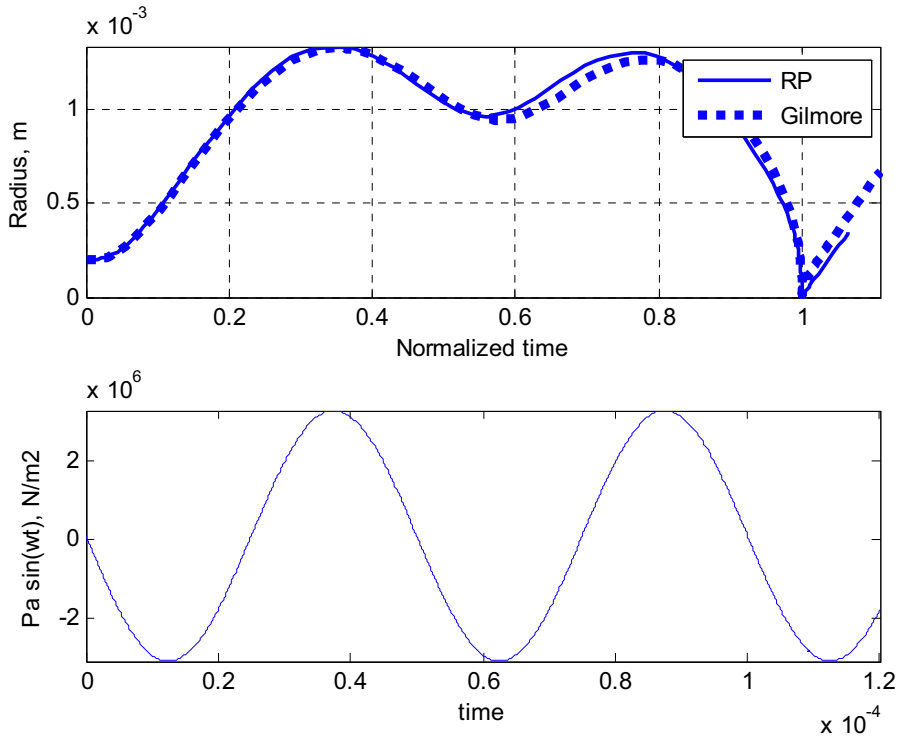

Fig. 3.4 – Variation of bubble radius with time in sodium assuming incompressible liquid (R-P equation) and taking into account the effect of compressibility (Gilmore's equation)

Table 3.2 – Calculated collapse pressure in sodium

Initial conditions	Parameter	RP equation (3.13)	Gilmore equation (3.16)
Sodium at 673 K, R_0 = 200 μm and $\frac{dR}{dt}_{t=0} = 0$	R_{max}	1.33 mm	1.32 mm
	R_{min}	$7.09*10^{-6}$ m	$1.79*10^{-5}$ m
	Max jet velocity	11125 m/s	1897 m/s
	Collapse pressure, MPa	$2.25*10^{4}$ MPa	3846 MPa

The RP equation gives unrealistic values of velocity when the pressure differential driving collapse is high. This is because the effect of liquid compressibility which is dominant in the final stages of collapse is not considered in the RP equation. In such cases, the Gilmore equation, which takes into account the effect of liquid compressibility, is to be used. It is seen from Table 3.2 that the velocity and collapse pressure in single bubble collapse predicted using the Gilmore equation is large enough to cause damage if the bubble is collapsing on or close to the solid surface.

In the event of a bubble collapsing in the bulk liquid, the liquid jet will not strike the surface directly and therefore the pressure due to water hammer effect is reduced. However, the pressure resulting from the compression of the bubble contents reaches very high values and the compressed bubble radiates spherical waves which are converted to shock waves in the course of propagation through the liquid. The pressure at the bubble wall in the liquid is calculated using equation 3.27 [103]. Fig. 3.5 shows the decrease in pressure with increasing radius due to spherical divergence. Although the pressure at the bubble wall is of the order of 10^{10} N/m^2, the pressure drops quickly away from the bubble wall and is still high enough to cause damage at a

distance of about 2 times the original bubble radius. In reality there will be an additional decrease due to irreversible thermodynamic losses at the shock wave front [103]. Hence the radial extent of damaging pressure value will be less than 2 times the original radius.

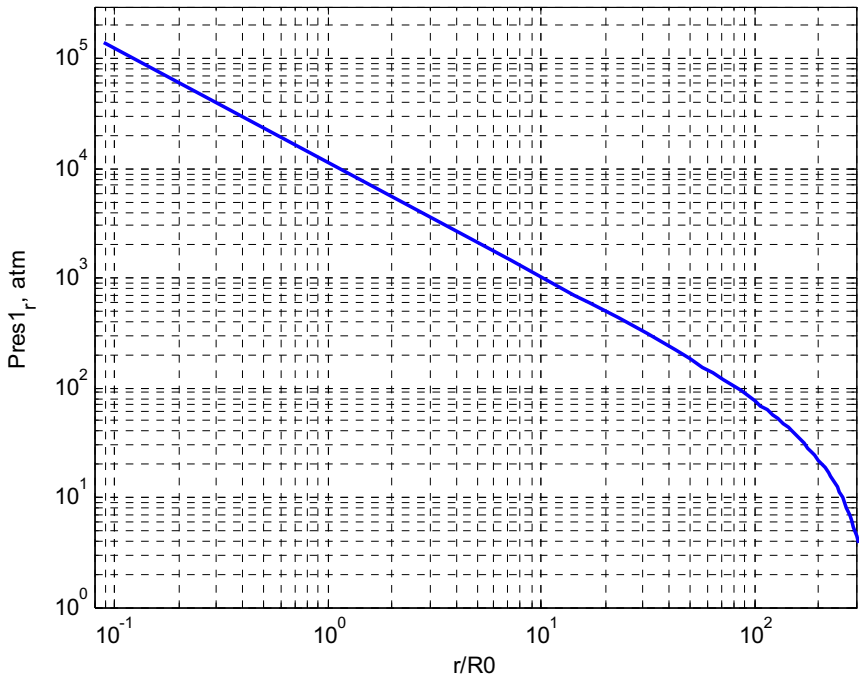

Fig. 3.5 – Variation of pressure in sodium with radial distance from the collapse center

3.5 COMPARISON OF COLLAPSE PRESSURE IN WATER WITH THAT IN SODIUM

The results of calculations done in water and sodium using Gilmore's equations (Table 3.1 and 3.2) are compared in Table 3.3.

Table 3.3 – Comparison of collapse pressures in water and sodium

Sl. No.	Parameter	Water	Sodium
1	Initial conditions / Ultrasonic parameters	Water at 293K, R_0 = 200 μm and $\frac{dR}{dt}_{t=0} = 0$	Sodium at 673 K , R_0 = 200 μm and $\frac{dR}{dt}_{t=0} = 0$
2	R_{max} , mm R_{min}, μm	1.07 35.2	1.33 17.9
3	Max. jet velocity, m/s	741	1897
4	Collapse pressure, MPa	1090	3840

It is evident from Table 3.3 that the bubble grows to a larger radius in sodium than in water and is compressed to a smaller radius in sodium (at 673K) compared to that in water at 293 K. This results in a larger transfer of energy to the liquid resulting in higher values of jet velocity and collapse pressure and consequently greater damage in sodium compared to that in water. Tests directly in sodium, although more difficult to do compared to that in water, are therefore preferred to evaluate material resistance to cavitation damage instead of extrapolating results from tests in water.

3.6 CONCLUSION

The above discussion, although simplistic as it considers the collapse of only a single bubble, shows that the pressures generated by the collapse of a single spherical bubble is large enough to cause damage. The collapse pressure computed in Tables 3.1 – 3.3 are rather high

even after the effect of compressibility is taken into account. This is because the effect of cushioning of surrounding bubbles is not accounted in the above calculations.

In reality, however, there will be a population of bubbles of various sizes in the cavitation zone and bubble collapse may be initiated by the shock wave propagating from the collapse of neighbouring bubbles. Moreover, bubbles adjacent to a solid surface will not retain the spherical symmetry during collapse. There will also be heat and mass transfer effects especially in the case of stable bubbles that oscillate with the applied field for a few cycles before breaking up into transient bubbles. The pressure generated from bubble collapse can also get partially cushioned by the neighboring bubbles containing dissolved gas; and many bubbles may not collapse adjacent or even close to a solid boundary. Liquid temperature will also influence the collapse pressure (and the resulting damage) not only due to the change in liquid properties (such as density, viscosity, compressibility, vapor pressure etc.) with temperature but also from changes in the number and size of the bubbles in the cavitation zone. As a result heat transfer effects will dominate collapse at higher temperatures while inertial effects will control at lower temperatures. The net effect of all the above mechanisms makes the numerical study of the collapse process a complex phenomenon deserving a detailed study by itself.

CHAPTER 4

DESCRIPTION OF EXPERIMENTAL FACILITY

CHAPTER 4 – DESCRIPTION OF EXPERIMENTAL FACILITY

4.0 INTRODUCTION

This chapter describes the experimental setup, the various components constituting it, the electrical and instrumentation details and the experimental procedure.

4.1 SELECTION OF TYPE OF FACILITY

As discussed in Sec. 2.2.1 and 2.2.2 several types of facilities are in use for measurement of cavitation erosion damage. For the present studies the vibratory cavitation device (described in Secns. 2.2.1 (v) and 2.2.2 (v)) is selected. The reasons for selecting the vibratory device are :

(i) It generates high intensity cavitation and therefore facilitates rapid evaluation of materials with high resistance to cavitation damage.

(ii) It is simple in construction and operation. Leak tightness, which is paramount while handling hazardous liquids like sodium, can be easily achieved with this device. The vertical construction of the device permits the use of a cover gas above the sodium free surface thus making it possible to achieve leak tightness by the easier method of sealing the cover gas from the atmosphere (rather than the more difficult task of sealing liquid sodium from the atmosphere).

(iii) Testing can be done with a small inventory of liquid

(iv) The method is codified (by ASTM G32-10) which standardizes the test procedure and permits comparison of results with published literature.

4.2 DESCRIPTION OF THE FACILITY

A facility for cavitation erosion testing of materials in liquid sodium was installed for the work.

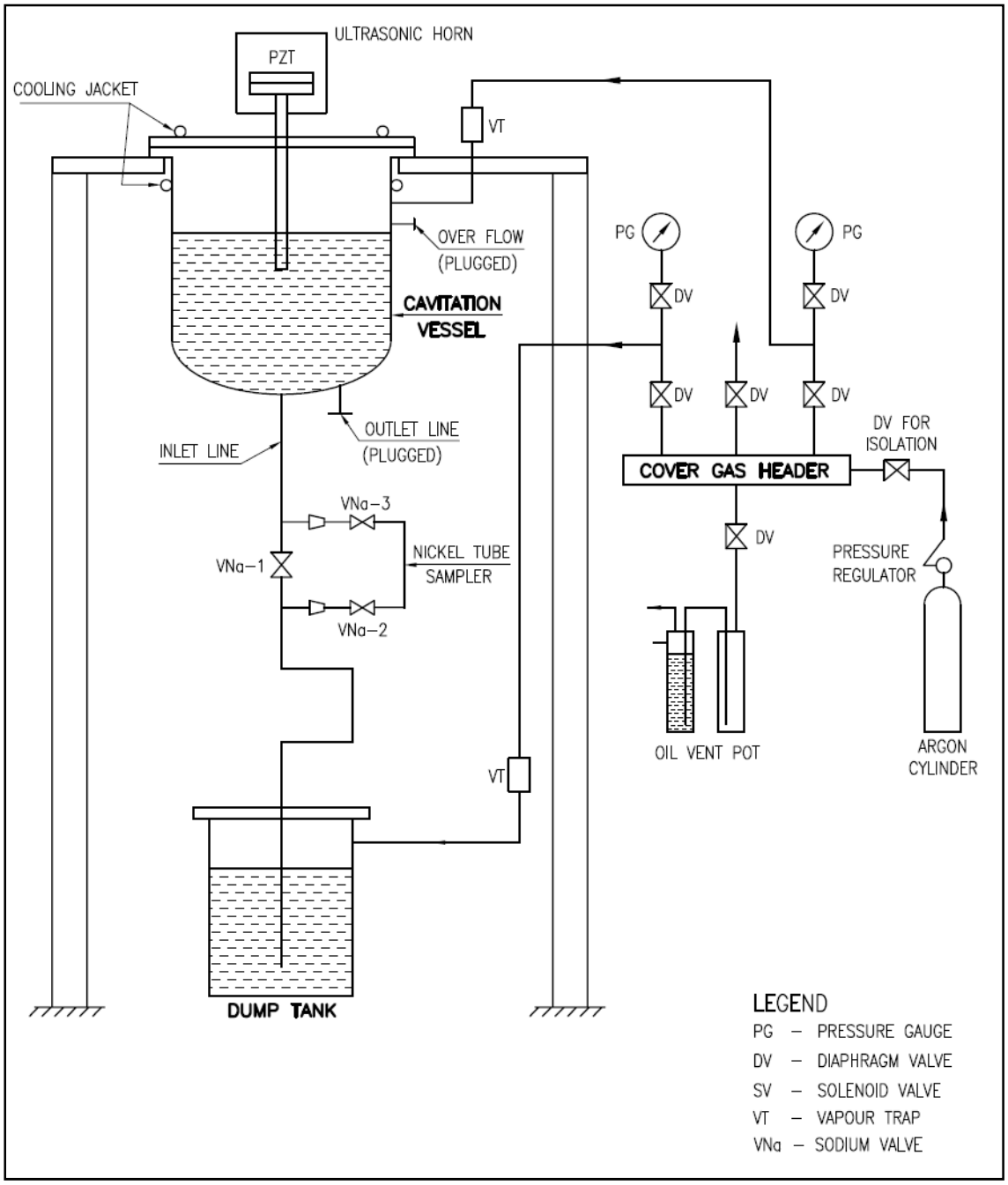

Fig. 4.1 – Schematic of the Cavitation Erosion Test Facility

Fig. 4.2 shows the photograph of the installed facility.

Fig. 4.2 – Cavitation Erosion Test Facility

The main components of the facility are (Fig. 4.1) :

(i) High Temperature Ultrasonic Cavitation (HTUC) equipment

(ii) Cavitation vessel

(iii) Dump tank

(iv) Piping

4.2.1 High Temperature Ultrasonic Cavitation (HTUC) equipment :

HTUC (Fig. 4.1 & 4.2) consists of ultrasonic generator, piezoelectric transducer, booster, horn, human machine interface (HMI), software, drive mechanism and cooling arrangement.

The ultrasonic generator works on 230 V, 50 Hz, AC power supply and delivers 20 kHz signal at the appropriate voltage and frequency to a piezoelectric (PZT) transducer through an RF cable. The piezoelectric transducer, which is mounted on a ring stand, converts the electrical energy into mechanical vibrations. The output of the PZT transducer is amplified by a booster mounted on the ring stand. An ultrasonic horn mounted to the booster amplifies the booster output. The specimen to be tested is threaded to the output end of the horn and immersed in the test liquid. Cavitation occurs at the specimen face when the horn vibrates. The HMI is used to position the horn in place, set the operating parameters and control the experiment. Software is also provided to control the operating parameters and the experiment. Both manual and auto mode operations are possible with the system. The operating parameters which can be controlled include horn positions (both horizontal and vertical), the amplitude of vibration, the cooling system temperature, experiment duration.

The rated power of the equipment is 3000 W (as per ASTM G 32, a power rating of 250 W to 1000 W is suitable). The power is selected to ensure that the amplitude of vibration remains steady when the specimen is submerged in sodium at the test temperature. The system is provided with automatic resonance and amplitude control and calibration of amplitude is done in air with a filar microscope. The amplitude of vibration of the horn can be adjusted, using the HMI or the provided software, to any value in the range of 22 μm. to 47 μm.

A pneumatic system is provided for horizontal movement of the transducer-booster-horn assembly. The vertical movement of the transducer-booster-horn assembly is achieved by means of a screw nut mechanism.

Cooling of the PZT transducer and the top of the horn is achieved by means of compressed air. Cooling of the top of the cavitation vessel and the vessel flange is achieved by

circulating thermic fluid (HYTHERM 600) through cooling jackets in the vessel and flange. The thermic fluid is cooled by means of a chiller unit of 2 TR capacity. The thermic fluid is circulated through the system by means of a gear pump of 1.2 m^3/h capacity (1/5 HP). . The oil pump and chiller unit is integrated with the HTUC system. The system is provided with auto ON/OFF feature to maintain the temperature of the thermic fluid.

4.2.2 Vibratory horn :

The function of the horn is to amplify the displacement of the PZT crystal. The horn is of stepped type with the diameter at its bottom end sized to suit the specimen dimension (16 mm) prescribed in ASTM G 32. The power of the ultrasonic generator is selected to ensure that the amplitude of vibration remains steady when the specimen is submerged in sodium at temperature. The material of the horn is AISI D2 . The temperature of the PZT transducer is maintained near room temperature by air cooling. The length of the horn is fixed such that the PZT transducer is well away from the sodium free surface. The horn is provided with a disc of 40 mm diameter which is pressed against the O ring seal on the vessel top flange central opening thus sealing the sodium in the vessel and preventing air ingress during operation. The disc is located at a nodal point on the horn and therefore its contact with the vessel at this point does not affect the frequency of operation of the horn. The length of the horn is fixed as 1.5 times the wavelength of sound in the material of the horn. The assembly of horn and specimen is designed for longitudinal resonance at the frequency of 20 kHz. The specimen is threaded to the bottom of the horn and the horn is threaded to the bottom of the PZT converter-booster assembly.

Fig. 4.3 is the sketch of the horn. Fig. 4.4 is the chemical composition test report of the material of the horn. Fig. 4.5 is the longitudinal resonance frequency test report of the horn.

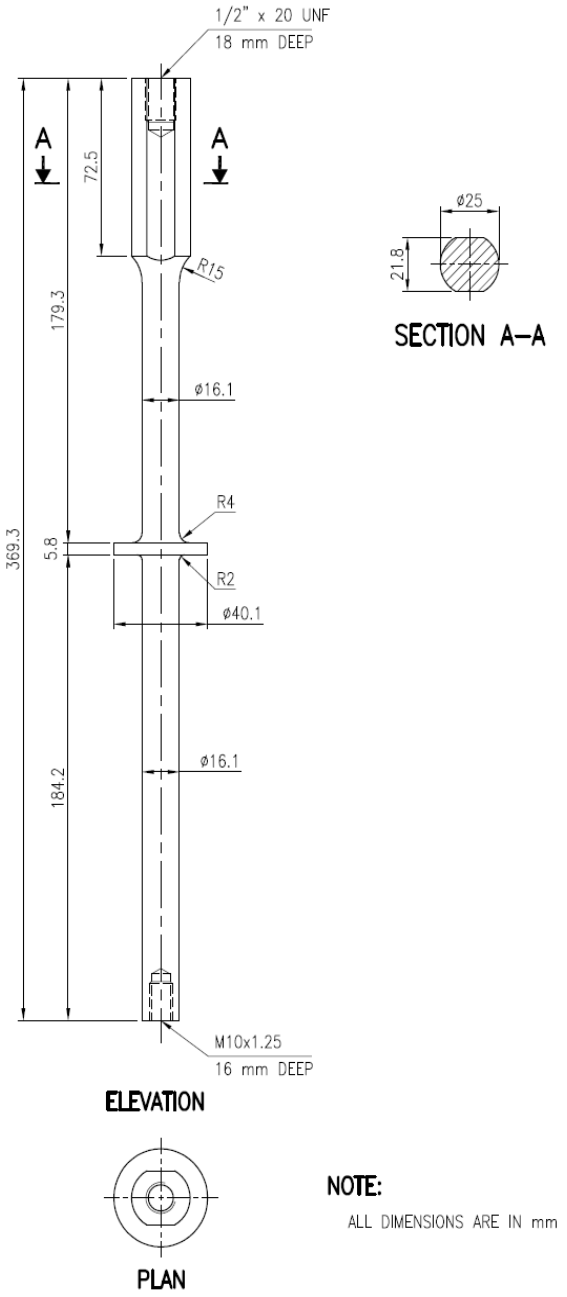

Fig. 4.3 – Ultrasonic Horn

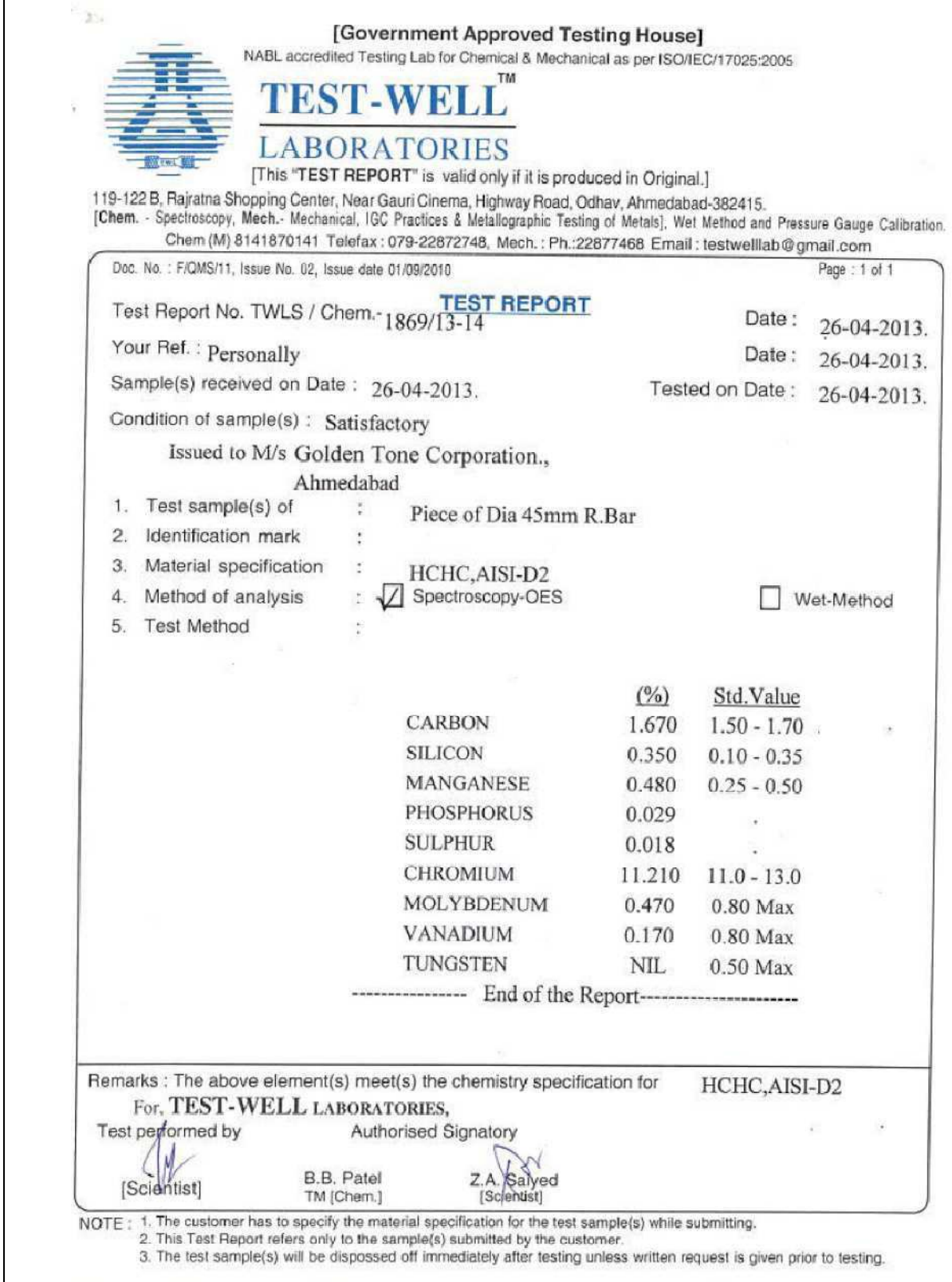

[Government Approved Testing House]

NABL accredited Testing Lab for Chemical & Mechanical as per ISO/IEC/17025:2005

TEST-WELL™

LABORATORIES

[This "TEST REPORT" is valid only if it is produced in Original.]

119-122 B, Rajratna Shopping Center, Near Gauri Cinema, Highway Road, Odhav, Ahmedabad-382415.

[Chem. - Spectroscopy, Mech.- Mechanical, IGC Practices & Metallographic Testing of Metals], Wet Method and Pressure Gauge Calibration.

Chem (M) 8141870141 Telefax : 079-22872748, Mech. : Ph.:22877468 Email : testwelllab@gmail.com

Doc. No. : F/QMS/11, Issue No. 02, Issue date 01/09/2010 Page : 1 of 1

TEST REPORT

Test Report No. TWLS / Chem.- 1869/13-14 Date : 26-04-2013.

Your Ref. : Personally Date : 26-04-2013.

Sample(s) received on Date : 26-04-2013. Tested on Date : 26-04-2013.

Condition of sample(s) : Satisfactory

Issued to M/s Golden Tone Corporation., Ahmedabad

1. Test sample(s) of : Piece of Dia 45mm R.Bar
2. Identification mark :
3. Material specification : HCHC,AISI-D2
4. Method of analysis : ☑ Spectroscopy-OES ☐ Wet-Method
5. Test Method :

	(%)	Std.Value
CARBON	1.670	1.50 - 1.70
SILICON	0.350	0.10 - 0.35
MANGANESE	0.480	0.25 - 0.50
PHOSPHORUS	0.029	.
SULPHUR	0.018	.
CHROMIUM	11.210	11.0 - 13.0
MOLYBDENUM	0.470	0.80 Max
VANADIUM	0.170	0.80 Max
TUNGSTEN	NIL	0.50 Max

---------- End of the Report----------

Remarks : The above element(s) meet(s) the chemistry specification for HCHC,AISI-D2

For, TEST-WELL LABORATORIES,

Test performed by Authorised Signatory

[Scientist] B.B. Patel TM [Chem.] Z.A. Sayed [Scientist]

NOTE : 1. The customer has to specify the material specification for the test sample(s) while submitting.
2. This Test Report refers only to the sample(s) submitted by the customer.
3. The test sample(s) will be dispossed off immediately after testing unless written request is given prior to testing.

Fig. 4.4 – Horn chemical composition test report

Roop Telsonic Ultrasonix Ltd.

QR/06/G/06

FINAL PERFORMANCE & TEST REPORT (SYSTEM INTEGRATION & APPLICATION DEPT.)

HORN TEST REPORT

GENERATOR:	SG-22-3KW- 20 KHZ						
CONVERTOR:	SE-50/50-4,20 KHZ HF						
BOOSTER:	1.0 ,20KHZ						
PARTY:		IGCAR		DATE:	25/5/2013		
Part :				JOB SHEET NO			
Horn Drg.No.				CODE NO.			
Required frequency		20 KHZ		Material		D2	

TESTING DETAILS

Frequency :-	HORN SR. NO.	AMP	70%	80%	90%	100%	
20.200 KHZ	20S1306-031	I.LOSS	0%	0%	0%	1%	

ZINC Plating: YES

Horn Accepted: YES

Tested by:- HARDIK PATEL Verified by:- HITESH PATEL

Fig. 4.5 – Horn longitudinal resonance frequency test report

The amplitude of vibration at the tip of the horn was measured in air is calibrated in-situ using a filar microscope as given in XI.2 of ASTM G32-10. Marcel Aubert filar microscope with RM-12 reticle having least count of 10 μm was used to measure the peak to peak amplitude of vibration. This value was measured to be 50 μm in air at room temperature.

The peak to peak amplitude of displacement employed for the present tests, however, is 25 μm. Although the recommended peak to peak displacement amplitude, as per ASTM G32-10

is 50 μm, an alternate value of 25 μm is also permitted (clause 9.1.2 of ASTM G 32-10). This value was selected because of loosening of the specimen and breakage of the horn during high temperature trials with peak to peak amplitude of 50 μm.

4.2.3 Cavitation vessel (Fig. 4.6) : The cavitation vessel is of 168.3 mm outer diameter, 260 mm in height and of 7.1 mm thickness. It is made from 6" schedule 40S pipe of ASTMA312 grade 316LN material. The vessel is provided with bottom inlet and outlet nozzles and two side nozzles that serve as overflow nozzles. The vessel is provided with a ring flange which rests on the support structure. The top of the vessel is closed with a top flange that is bolted to the ring flange. Leak tightness between the two flanges is achieved by means of O ring seal provided on the ring flange. Cooling jackets are provided at the vessel top and on the top flange. Thermic fluid is circulated through these jackets during operation to remove the heat transferred from the hot liquid sodium in the vessel to the top flange. This arrangement is necessary to maintain the temperature of the horn within limits during operation. The top flange is also provided with a central opening through which the horn containing the test specimen is introduced into the vessel. O ring seal is provided on the top surface of the opening to provide leak tightness between this surface and the horn. The central opening is closed with a blind flange, bolted to it, when the system is not in operation. The top flange is provided with nozzle openings for the introduction of level probes and cover gas connection. Nozzle openings are also provided to the cooling jackets for entry and exit of cooling thermo fluid oil. The bottom surface of the top flange is provided with thermal baffles for reducing the heat load from liquid sodium to the flange. The thermal baffles are supported on tie rods which are screwed to the bottom of the top flange.

The vessel is provided with two spark plug type level probes, viz. low level probe and high level probe, to maintain the submergence of the specimen to the desired level.

During operation the vessel is filled with sodium up to the high level indication and the sodium free surface is topped by argon cover gas. The cover gas in the vessel is connected to the common cover gas header through a vapor trap.

Although separate nozzles are provided at the vessel bottom for inlet and outlet, only one nozzle is used and the other is dummied and kept as spare nozzle. The inlet/outlet nozzle is provided with a bellows sealed valve to isolate the cavitation vessel and maintain the sodium level in the vessel during the experiment.

4.2.4 Dump tank : The dump tank (Fig. 4.7) is located at the bottom most part of the circuit. The tank is made from SS 316LN grade material. It contains enough sodium to fill the cavitation vessel to the required capacity. The cavitation vessel is emptied into the dump tank after each experiment is completed. The dump tank is provided with two spark plug type level probes. The sodium in the dump tank is topped by argon cover gas and the cover gas in the tank is connected to the common cover gas header through a vapor trap.

4.2.5 Piping : SS 316LN piping (1/2” sch 40) is used to connect the dump tank to the cavitation vessel. Adequate flexibility is provided in the piping through expansion bends

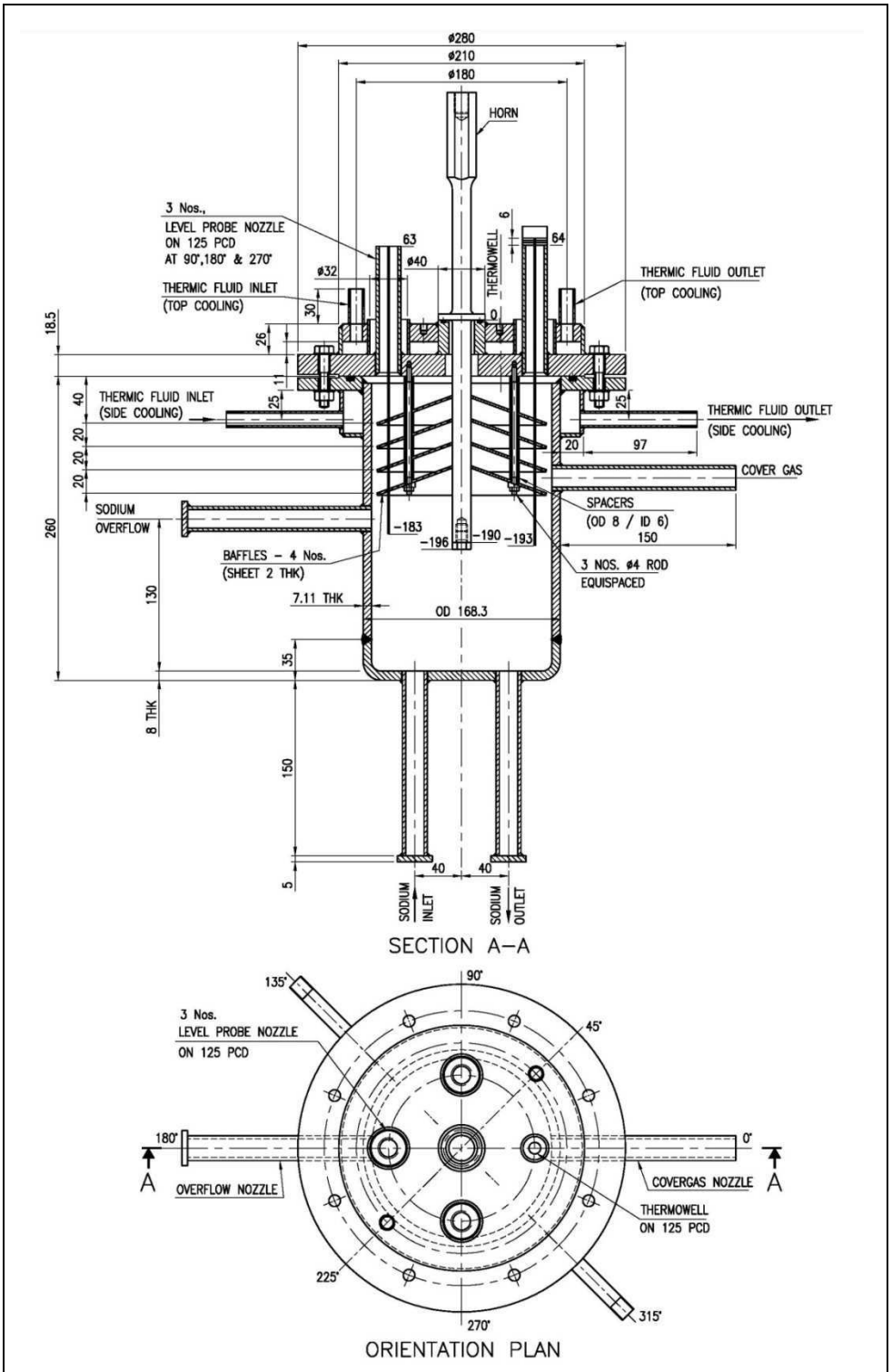

Fig. 4.6 – Cavitation Vessel

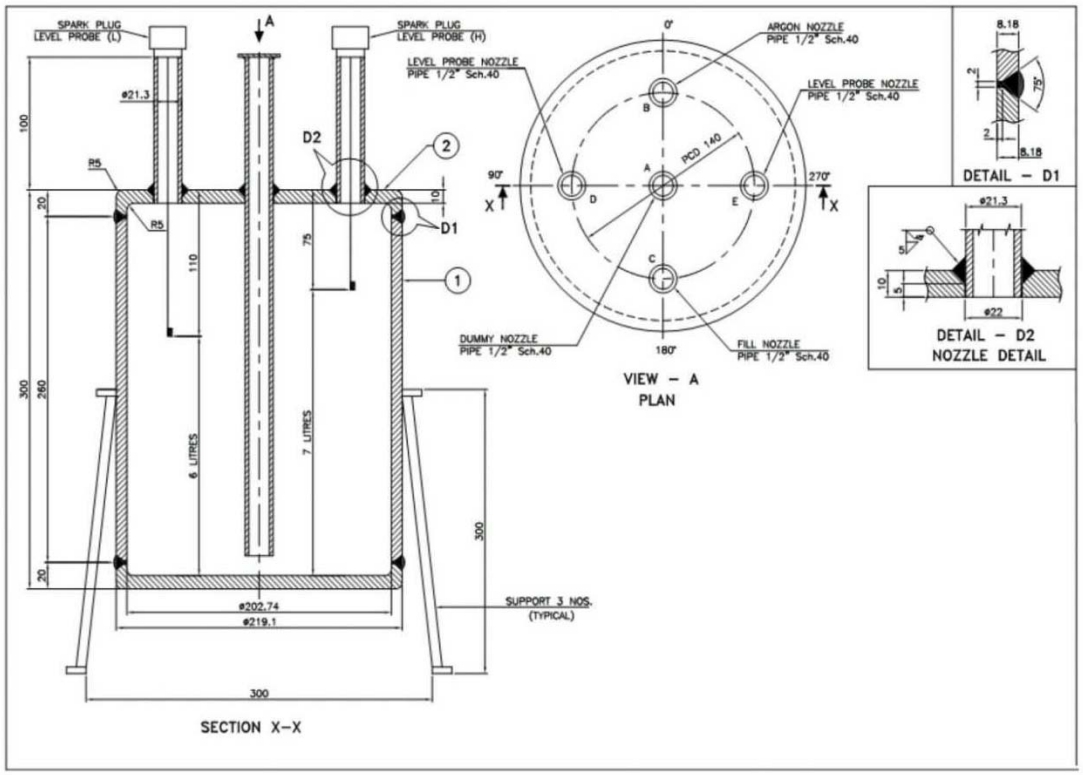

Fig. 4.7 – Dump Tank

4.2.6 Electrical And Instrumentation Details

The cavitation vessel, dump tank and interconnecting pipeline are provided with high temperature tape heaters for preheating the vessel and heating sodium in the vessel.

Table 4.1 gives the heater details.

Table 4.1 - Heater Details

Sl. No.	Heater	Rating	Location
1	H1	2 m / 400 W	Cavitation vessel
2	H2	5m / 1000 W	Sodium piping
3	H3	2 m / 400 W	Dump tank
4	H4	2 m / 400 W	Dump tank
5	H5	2m / 400 W	Vapor trap of dump tank
6	H6	2 m / 400 W	Vapor trap of cavitation vessel
7	H7	3 m / 600 W	Sodium sampler line

Power supply to the heaters is provided through triac based power control units. Heating system is divided into 4 zones. Zone-1 consists of cavitation vessel heater (H1), zone-2 consists of sodium pipe line heater (H2), zone-3 consists of dump tank heaters (H3) and (H4), zone 4 consists of heaters (H5) of vapor trap of dump tank, zone-5 consists of heaters (H6) of vapor trap of cavitation vessel, and zone-6 consists of heater (H7) in sodium sampler line.

Eleven K type thermocouples are provided for temperature measurement at different locations. The temperature of the sodium in the vessel is monitored using 2 nos. of thermocouples located at 50 mm and 150 mm from the vessel bottom.

The cavitation vessel is provided with 2 nos. of spark plug type level probes for level measurement. The elevation difference between the low level probe and the high level probe is 12 mm. Fig. 4.8 indicates the low level and high level of sodium in the vessel vis-à-vis the face of the specimen during testing.

The instruments used to measure the test parameters are given in Table 4.2 below

Table 4.2 - Instrumentation Details

Sl. No.	**Parameter**	**Instrument**	**Accuracy**
1	Weight	Electronic balance	$\pm$ 0.1 mg
2	Time	Stop watch	$\pm$ 1 s
3	Cover gas pressure	Bourdon gage	$\pm$ 10 mbar
4	Level of sodium	Resistance type level probe	$\pm$ 1 mm
5	Temperature	K type thermocouple	$\pm$ 1.5% of reading
6	Ultrasonic operating frequency	Automatic control in HTUC	$\pm$ 0.5 kHz
7	Displacement amplitude	Automatic control in HTUC	$\pm$ 2.5 μm

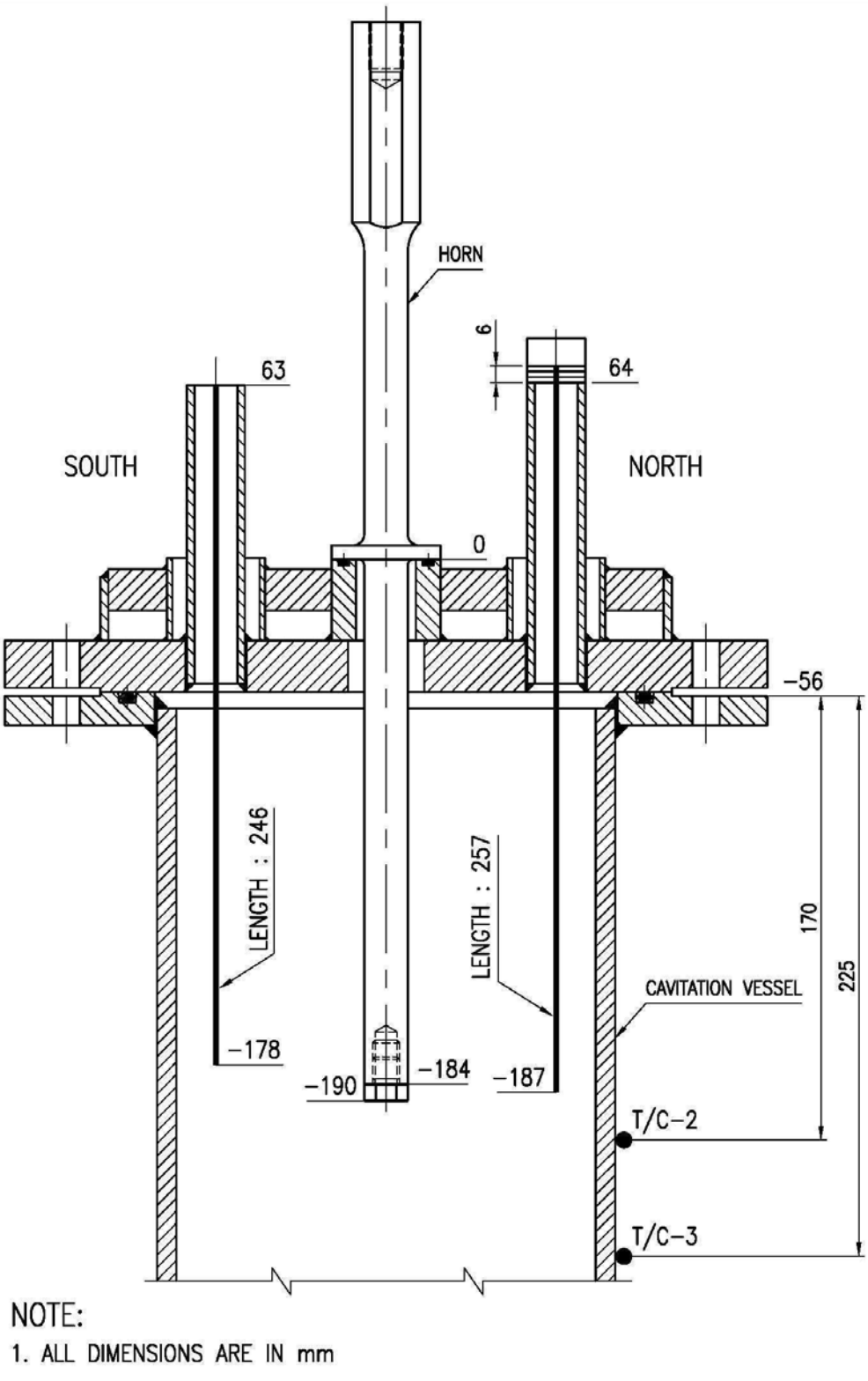

Fig. 4.8 – Sodium levels and specimen during testing

The bottom surface of the specimen is submerged by 12 mm when the high level indication is live. This ensures that the submergence of the specimen during testing is in conformance with the submergence requirement specified in ASTM G 32.

Seven leak detectors arranged in a single channel are provided for the test set up. One spark plug type leak detector is provided for valve VNa1. The output of thermocouples and leak detectors is displayed using a toggle switch operated digital indicator.

Fig.4.9 is a schematic of the facility showing heater, thermocouple and leak detector details.

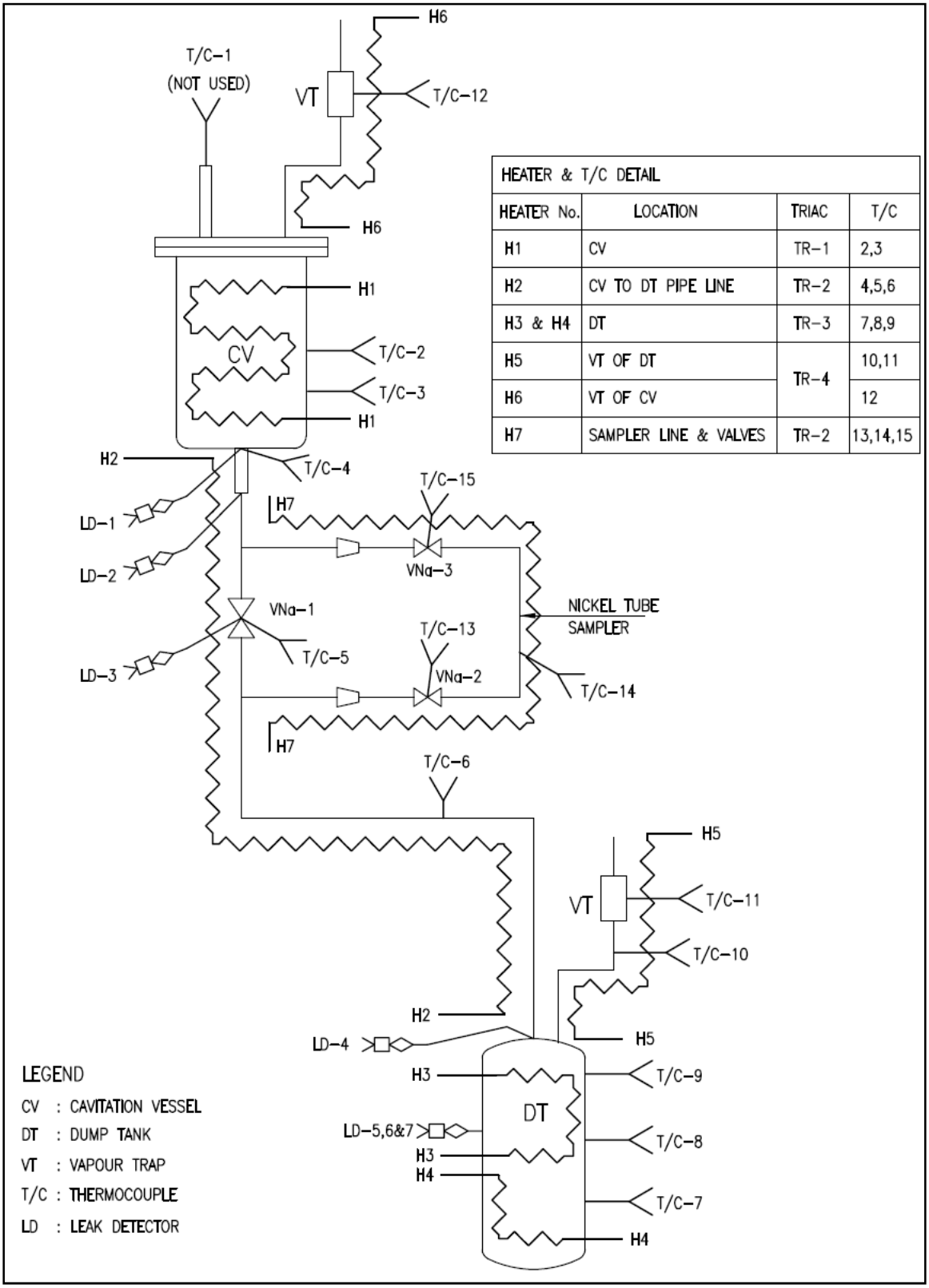

HEATER & T/C DETAIL			
HEATER No.	LOCATION	TRIAC	T/C
H1	CV	TR-1	2,3
H2	CV TO DT PIPE LINE	TR-2	4,5,6
H3 & H4	DT	TR-3	7,8,9
H5	VT OF DT	TR-4	10,11
H6	VT OF CV		12
H7	SAMPLER LINE & VALVES	TR-2	13,14,15

Fig. 4.9 – Layout of heaters, thermocouples and leak detectors in the facility

The locations of the leak detectors and thermocouples in the set up are summarized in Table 4.3 below:

Table 4.3 – Locations of leak detectors and thermocouples

		Instrumentation			
Sl. No.	**Component**	**Level probe**	**Leak detector**	**Thermocouple**	**Pressure gage**
1	Cavitation vessel	2 nos. of spark plug type	1 nos. on weld between vessel shell and bottom dished end 1 nos. on weld between vessel bottom nozzle and piping	K type 2 nos. on vessel body 1 nos. on vessel bottom nozzle 1 nos. on vapor trap	-
2	Bellows sealed valve	---	1 nos. on valve body 1 nos. above bellows	K type 1 nos. on vessel body	-
3	Piping	---	---	K type 1 nos. in horizontal run	-
4	Dump tank	---	1 nos. on weld between piping and dump tank nozzle 3 nos. on dump tank surface	K type 3 nos. on vessel body 1 nos. on cover gas line 1 nos. on vapor trap	-
5	Cover gas				Independent Bourdon type gage on cover gas lines of dump tank and cavitation vessel.

4.3 DESIGN OF MAJOR COMPONENTS

4.3.1 Components Design

4.3.1.1 Cavitation vessel

The cavitation vessel is designed as per Boiler and Pressure Vessel code ASME Sec VIII Divison1. The design temperature is 550°C. All welds are radiographed and the vessel subjected to pneumatic testing.

4.3.1.1.1 Cooling system : Cooling jackets are provided on the top flange and the top portion of the outer surface of the cavitation vessel. Cooling is achieved by circulating thermic fluid (Hytherm 600) through the cooling jackets. The thermic fluid is cooled by an air / liquid heat exchanger and auto regulation of temperature is provided. consists of

4.3.1.2 Dump tank : The dump tank is designed as per Boiler and Pressure Vessel code ASME Sec VIII Divison1. The design temperature is 400°C. All welds are radiographed and the vessel subjected to pneumatic testing.

4.3.1.3 Ultrasonic horn : The ultrasonic horn is made of tool steel HCHC, AISI D2. The following considerations govern the selection of material of construction of the horn :

(i) fatigue strength : materials with high fatigue strength can be operated at high amplitudes (i.e. high stress levels)

(ii) low acoustic loss

(iii) compatibility with sodium

(iv) resistance to cavitation because a portion of the horn is immersed in the liquid and can experience high impact load from collapsing bubbles

(v) machinability

(vi) availability and cost

(vii) high yield strength, high impact strength

(viii) satisfactory mechanical properties at high operating temperature

The length of the horn is fixed as 1.5 times the wavelength of sound in the material of the horn. The assembly of horn and specimen is designed for longitudinal resonance at the frequency of 20 kHz. The horn is subjected to alternating stress during operation. The analysis of the horn to determine its longitudinal natural frequency and displacement and stress along its length is discussed in Appendix 1.

4.4 PRE-COMMISSIONING TESTS

Purified sodium was transferred to the dump tank up to high level indication. The tank was cooled, cut from the transfer system and dummied. It was then positioned in the test area and connected to the piping from the cavitation test vessel.

The horn containing the test specimen was connected to the booster, the ultrasonic generator powered and satisfactory operation of the ultrasonic system confirmed. The satisfactory operation of the pneumatic system, energizing the horizontal movement of the booster-horn assembly, and the motorized screw nut assembly, for vertical motion of the booster-horn assembly, was confirmed.

The cavitation vessel was closed with the top flange and the assembly of horn and specimen lowered in to the vessel through the central opening in the flange until the collar on the

horn rested on the O ring joint in the central opening and sealed the vessel. The bellows sealed valve at the inlet of the cavitation vessel was closed and the vessel flushed with argon. Pressure hold test of the vessel was done at 0.5 bar (g) for 4 h to confirm leak tightness. The valve was then opened, the entire system flushed with argon and pressure hold test of the entire system done at 0.5 bar(g) for 4 h.

4.5 DETAILS OF TEST SPECIMENS

Figs. 4.10, 4.11 show typical test specimens. The specimens are of ~ 16 mm in diameter. The circular specimen was provided with two diametrically opposite flats of 7.5 mm width to facilitate tightening using a standard spanner. Three types of specimens were tested. Type 1 was austenitic stainless steel (SS 316L) machined from bar stock, Type 2 was austenitic stainless steel (SS 316 L) machined from bar stock and hard faced with Colmonoy5 and Type 3 was austenitic stainless steel (SS 316 L) machined from bar stock and hard faced with Stellite6. The tests were done in sodium at temperatures of 200ºC, 250ºC, 300ºC and 400ºC. At 200 ºC, three nos. of SS 316L specimens , two nos. each of Colmonoy5 hardfaced specimens and Stellite6 hardfaced specimens were tested; at 250ºC, two nos. of SS 316L specimens, three nos. of Colmonoy5 hardfaced specimens and two nos. of Stellite6 hardfaced specimens were tested; at 300ºC, three nos. of SS 316L specimens , two nos. of Colmonoy5 hardfaced specimens and one no. of Stellite6 hardfaced specimens were tested; and at 400ºC one nos. each of SS 316L, Colmonoy5and Stellite6 hardfaced specimens were tested.

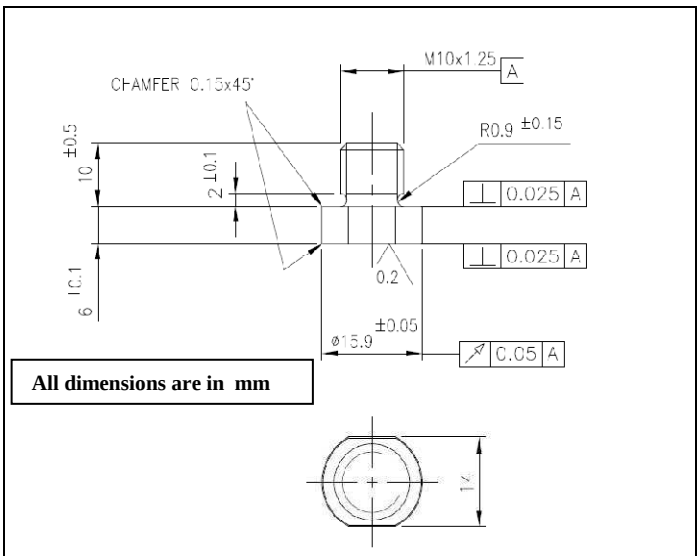

Fig. 4.10 – Cavitation Specimen – SS316L

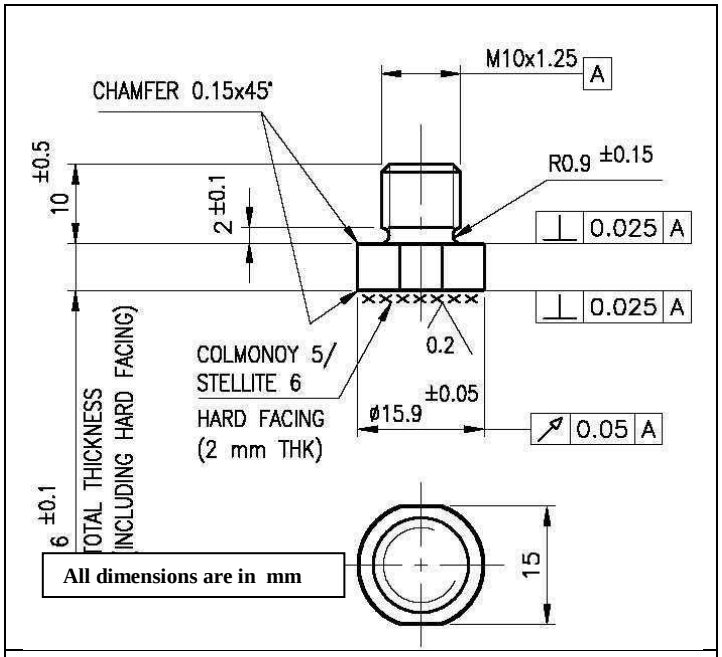

Fig. 4.11 – Cavitation Specimen – SS316L hardfaced with Colmonoy5 / Stellite6

The chemical composition of the base metal of the specimens (SS 316 L) specimens tested is shown in Table 1 (by direct reading optical emission spectrometer) [108].

Table 4.4 – Chemical composition of SS 316 L

Element	Cr	Ni	C	Mn	Mo	Si	Cu	Co	W	Va	Ti	Al
wt %	17.5 ± 0.6	10 ± 0.3	0.02 ± 0.002	1.63 ± 0.07	2.05 ± 0.02	0.38 + 0.02	0.34 ± 0.02	0.11 ± 0.01	0.08 ± 0.01	0.07 ± 0.01	< 0.08	< 0.03

4.6 PREPARATION OF SPECIMENS

The specimens were machined from SS316L, 20 mm bar stock. The circular specimen was provided with two diametrically opposite flats of 7.5 mm width to facilitate tightening using a standard spanner. The face of the specimen was polished to mirror finish (< 1 μm for SS316L and Stellite6 specimens and ~ 2.5 μm for Colomony5 specimen) so as to enable meaningful examination of the test surface (by SEM) after short duration tests. Hardness of the specimens was measured, before polishing, by selecting randomly 2 pieces from lots of ~ 15 samples. The measured hardness and other properties of the samples are shown in Table 4.5.

Table 4.5 – Properties and measured hardness of hard faced deposits

Properties	SS 316 L	Hardfacing	
		Stellite 6	Colmonoy5
Deposit thickness, mm (average)	-	2	2
Density, gm/cm^3	7.97 [109]	8.12 [110]	8.14 [111]
Hardness, Maximum value Mean + SD (measured from 2 random samples in each type using FIE, model RASNE-1 digital Rockwell hardness tester)	 96.4 HRB [112] 95.61 ± 0.77 HRB (233 VHN)	 39.4 HRC [112] 38.64 ± 0.67 (369 VHN)	 44.4 HRC [112] 40.69 ± 3.2 (393 VHN)

Typical compositions of the hard facing deposits, Colmonoy5 and Stellite6, are given in Table 4.6. Both materials were deposited in powder form by Plasma Transfer Arc Welding

(PTAW) process. Established welding procedure specification was used for deposition of the hardfacing coating [113].

Table 4.6 - Typical compositions of Colmonoy5 and Stellite6 [18]

	wt %								
Alloy	B	C	Cr	Co	Fe	Mn	Ni	Si	W
Stellite 6	-	1.0	27.0	60	< 2.5	1.0	< 2.5	1.0	5
Colmonoy5	2.5	0.65	11.5	< 0.25	4.25	-	77.10	3.75	-

4.7 SODIUM PURITY

The impurity levels present in the initial charge of sodium are :

O = 5 ppm, C = <5 ppm, Ca = < 2 ppm, B < 1 ppm, Ba < 7 ppm, Li < 0.2 ppm, Fe < 0.5 ppm, Zn < 2 ppm, U < 0.001 ppm, K < 250 ppm, Ag < 0.5 ppm, S < 10 ppm, Cl < 10 ppm, Br < 5 ppm. [114]

The system does not have a built in purification facility. However, the cover gas pressure in the system was maintained above atmospheric pressure, both during operation and when not in use, to prevent air ingress. Also, during interventions to introduce or remove the horn/specimen from the system, continuous argon purging was maintained to prevent air ingress. Although care was taken through operational procedures to maintain inert atmosphere in the facility, it was observed after several experiments (~ 50 nos.) that the impurity level in the system had increased. It is reported [22, 24] that oxygen level of 100 ppm in sodium does not have adverse effect on resistance to cavitation erosion in stainless steel. In this case the maximum expected oxygen impurity at the highest temperature operated (300ºC), assuming saturation conditions, is 100 ppm.

After the initial tests at 300ºC, the sodium in the facility was replaced with fresh charge of sodium for further tests. The dump tank in the facility was cut and removed and replaced with a new dump tank containing purified sodium. Care was taken during the experiments to maintain the purity by argon purging during system interventions and by ensuring positive cover gas pressure during operation as well as when the system was not in use.

4.8 OPERATING PARAMETERS

The following are the operating parameters for all experiments :

Frequency of operation : 20 kHz

Amplitude of operation (peak to peak) : 25μm

Power of ultrasonic generator : 3000 W

Submergence of specimen = 11 mm

Pressure of argon cover gas in cavitation vessel = 100 mbar(g).

4.9 EXPERIMENTAL PROCEDURE

The specimen is polished, cleaned using water and then with acetone, dried and weighed using an electronic balance of 0.1 mg accuracy. In the case of specimens which are to be examined by SEM during the course of the testing, the specimens are examined by SEM before the test. The specimen is assembled on the ultrasonic horn and the assembly mounted on the vibratory cavitation equipment.

Before starting the experiment, the system is checked for leak tightness by a pressure hold test. This is followed by cold purging of the entire system to expel any residual moisture. The system is then preheated and the cavitation vessel purged with argon in hot condition. The

ultrasonic horn containing the test specimen is then introduced into the cavitation test vessel with continuous argon purging to prevent air ingress. The cavitation test vessel is then filled with sodium to the required level by pressurizing the dump tank and venting the cavitation test vessel. The level of sodium in the cavitation test vessel is monitored using two nos. of resistance type level probes.

After filling, the cavitation test vessel is isolated from the dump tank. The temperature of sodium in the cavitation test vessel is then stabilized to the test temperature after which the ultrasonic horn is powered to start the experiment. The duration of a single test varies from as low as 5 min (in cases where SEM examination is planned) to as long as 2 hours.

After the prescribed test period, the ultrasonic horn is switched off, sodium dumped and the cavitation test vessel cooled to room temperature. The horn is then removed from the vessel under continuous argon purging and sealed in polythene bag in argon atmosphere (Fig. 4.12). The central opening of the cavitation test vessel is closed and both the cavitation test vessel and the dump tank are maintained under inert atmosphere to prevent any air ingress into the system.

Fig. 4.12 – Handling of horn and sample after testing and prior to sodium removal

The specimen is then removed from the ultrasonic horn, cleaned first with methyl alcohol and then in ultrasonic bath with distilled water. Care is taken to ensure that the cleaning process does not result in any erosion of the specimen by locating the specimen away from the base of the bath, where the transducers are fixed, and by suspending the specimen in the bath such that its face is away from the transducers in the bath. The specimen is then cleaned and dried.

4.10 MEASUREMENTS AND EXAMINATION AFTER TESTING

The specimen is well polished to mirror finish, cleaned and dried and weighed. Prior to start of the test the hardness of each type of specimen is measured from 2 random samples in each type using FIE, model RASNE-1 digital Rockwell hardness tester. One or two samples

(which are selected for SEM examination and roughness measurements during the course of testing) are examined using SEM before start of testing. The surface roughness before start of testing is also measured for the selected specimens using optical profilometer.

4.10.1 Weight loss measurement

The cleaned and dried specimen is weighed using an electronic balance with accuracy of 0.1 mg. The weight loss incurred in the test is estimated and the cumulative weight loss calculated. The testing time of the particular test and the cumulative testing time are also recorded.

If W_0 is the initial weight of the cavitation free specimen specimen, W_i is the weight after the ith test and t_i is the time duration of the i^{th} test, then the cumulative weight loss is given by $\Delta W = W_0 - W_i$ and the cumulative time is Σt_i. The cumulative weight loss rate, $\Delta W' = \Delta W / \Sigma t_i$,

4.10.2 SEM examination

Selected specimens are examined under a scanning electron microscope (using Obducat Camscan-3200 SEM) at various magnifications at different locations in the periphery and the central region.

4.10.3 Roughness measurement

The roughness of select few specimens after each test was measured with the objective of correlating surface roughness with cavitation damage due to weight loss. Surface roughness of the selected specimens was measured using a non-contact type optical profiler Talysurf CLI 1000. Rectangular areas, in the middle of the specimen, of dimensions 2 mm * 10 mm and 2 mm * 13 mm, in mutually perpendicular directions (x and y), were scanned. The average roughness, R_a , was computed from the scanned data. The average roughness, R_a , is defined as the

arithmetic mean deviation of the surface. It is the roughness height as calculated over the entire measured area in each of the directions, x and y. The absolute roughness is then calculated as the square root of the sum of the squares of the average roughness in the x and y directions.

CHAPTER 5

RESULTS & DISCUSSION

CHAPTER 5 – RESULTS & DISCUSSION

5.0 INTRODUCTION

This chapter presents results of various tests described in Chapter 4. A comparison is made on the cavitation performance of SS 316L, Stellite 6 and Colmonoy 5 coatings. Weight loss resulting from cavitation damage is correlated with surface damage observed after the test, hardness of the deposit and other properties of the alloys. As cavitation damage is primarily estimated from weight loss measurements, an error analysis is first presented. Data acquired from the cavitation tests are in Appendix 2.

5.1 ERROR ANALYSIS [115]

The following measured variables influence the weight loss rate :

(i) Weight of specimen

(ii) Cover gas pressure

(iii) Temperature of liquid

(iv) Sodium level in cavitation vessel

(v) Operating frequency

(vi) Amplitude of displacement

(i) Error in weight measurement

The weight is measured to accuracy of 0.1 mg. Assuming the uncertainty to be normally distributed, the standard uncertainty (calculated based on the smallest weight measured) is ,

$u_1 = \frac{0.1*10^{-3}}{2}$ = $5*10^{-5}$ g = $5*10^{-5}$ / 12.55 * 100 = $3.98*10^{-4}$ %

(ii) Error in cover gas pressure

A Bourdon pressure gage is used to measure the pressure of cover gas in the cavitation vessel. The smallest pressure change that can be read from the gage is $\pm$5 mbar. Assuming the uncertainty to be normally distributed, the standard uncertainty, $u_2 = \frac{5}{2}$ = 2.5 mbar = 2.5/100 * 100 (for cover gas pressure of 100 mbar) = 2.5%.

(iii) Error in Temperature

The temperature of sodium in the vessel is measured using K type thermocouples spot welded to the vessel. The error in temperature measurement is $\pm$ 1.5% of the reading. For a maximum temperature of 400 ºC, error = 1.5/100*400 = 6 ºC. Assuming the uncertainty to be normally distributed, the standard uncertainty, $u_4 = \frac{6}{2}$ = 3 ºC = 3/400*100 = 0.75 %

(iv) Error in sodium level

The level of sodium in the cavitation vessel is measured by a resistance type spark plug level probe. The error in level measurement is $\pm$ 1 mm. Assuming the uncertainty to be normally distributed, the standard uncertainty, $u_3 = \frac{1}{2}$ = 0.5 mm = 0.5/12 * 100 = 4.1 %. Since the absolute value of level (13 mm) is small this value is large. However, the range in the level permitted by ASTM G32 is 12$\pm$ 4 mm and this is achieved by keeping the inlet

valve 'crack' open while filling. For calculations, however, the uncertainty above is considered.

(v) Error in operating frequency

The operating frequency of 20 kHz is automatically controlled by the instrument to within $\pm$ 0.5 kHz. Assuming the uncertainty to be normally distributed, the standard uncertainty, $u_5 = \frac{0.5}{2}$ = 0.25 kHz = 0.25/20 * 100 = 1.25 %

(vi) Error in amplitude of displacement

The displacement amplitude of 50 μ is automatically controlled to within 2.5 μ. Assuming the uncertainty to be normally distributed, the standard uncertainty, $u_6 = \frac{2.5}{2}$ = 1.25 μ = 1.25/50 * 100 = 2.5 %.

Hence the combined standard uncertainty = $\sqrt{2.5^2 + 0.75^2 + 4.1^2 + 1.25^2 + 2.5^2}$ = 5.6 %

The expanded uncertainty based on a coverage factor of 2, providing a level of confidence of 95%, is 2*5.6 % = 11.2 %.

This error band is shown along with average value for weight loss measurements in the graphs.

5.2 RESULTS

5.2.1 Weight Loss

Table 5.1 gives details of the three different types of specimens employed in this study. It may be noted that hardness of the coatings is significantly higher than that of 316L material and among the two coatings Colmonoy5 has higher hardness. Further, although all the specimens

were polished to have mirror finish on the eroding surface, the absolute surface roughness of Colmonoy 5 specimens, before start of testing, is higher than that for the other two types of specimens.

Table 5.1 – Properties of specimens

Properties	SS 316 L	Hardfacing	
		Stellite 6	Colmonoy5
Deposit thickness, mm (average)	-	2	2
Hardness, Maximum value	96.4 HRB [112]	39.4 HRC [112]	44.4 HRC [112]
Mean + SD (measured from 2 random samples in each type using FIE, model RASNE-1 digital Rockwell hardness tester)	95.61 $\pm$ 0.77 HRB (233 VHN)	38.64 $\pm$ 0.67 (369 VHN)	40.69 $\pm$ 3.2 (393 VHN)
Absolute surface roughness, μm	< 1	< 1	< 2.5

The face of the specimen was polished to mirror finish (< 1 μm for SS316L and Stellite6 specimens and < 2.5 μm for Colomony5 specimen)

5.2.1.1 Austenitic Stainless Steel 316L

Cavitation tests were done in SS 316L at four temperatures viz. 200ºC, 250ºC, 300ºC and 400ºC. At 200ºC three numbers of specimens, at 250ºC two numbers of specimens, at 300ºC three numbers of specimens and at 400ºC one specimen were tested (Tables A2.1 – A2.9). Results of the weight loss measurements done on these specimens are given in Fig 5.1.

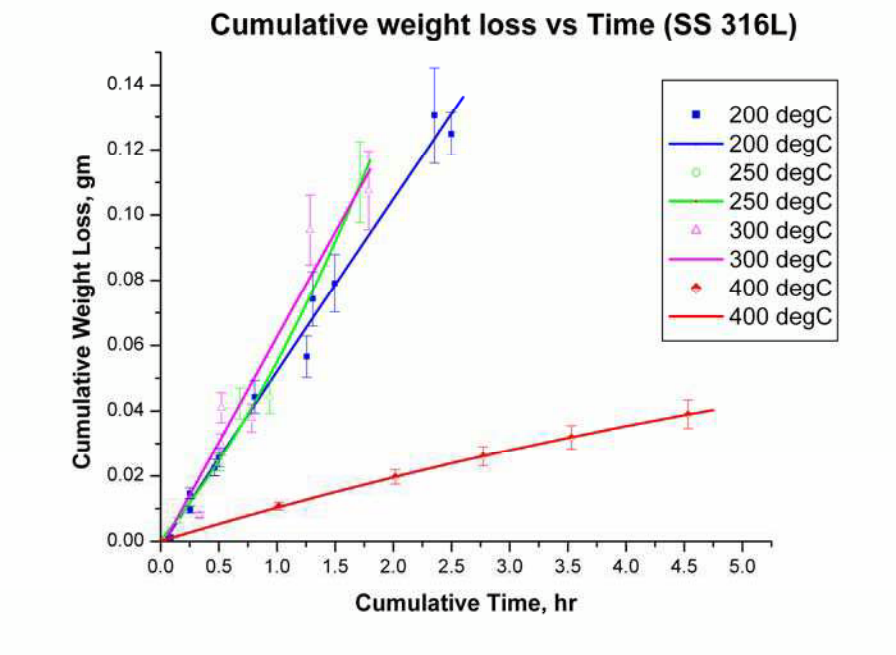

Fig. 5.1 – Cumulative weight loss vs cumulative time for SS 316L

There is a marginal increase in weight loss with increase in temperature from 200 ºC to 300 ºC. However, weight loss is significantly lower for the specimen tested at 400 ºC. Results indicate weight loss due to cavitation increases with increase in temperatures up to 300 ºC and then decreases.

For a given temperature, the variation of weight loss with duration of testing is similar to that reported by Dayer [23] although the absolute values of weight loss in the present case are smaller than that reported in [23]. This could be due to the lower peak to peak amplitude of displacement employed for the present tests (viz. 25 μm, which is the alternate peak to peak displacement permitted in ASTM G32) compared to the value of 50 μm reported in [23]. Moreover, the operating frequency of the horn in the present tests is the ASTM G32 prescribed value of 20 kHz while that used in [23] is 15.5 kHz.

Fig. 5.2 shows the variation of rate of weight loss with time and Fig. 5.3 shows the variation of Mean Depth of Penetration Rate (MDPR) rate with temperature.

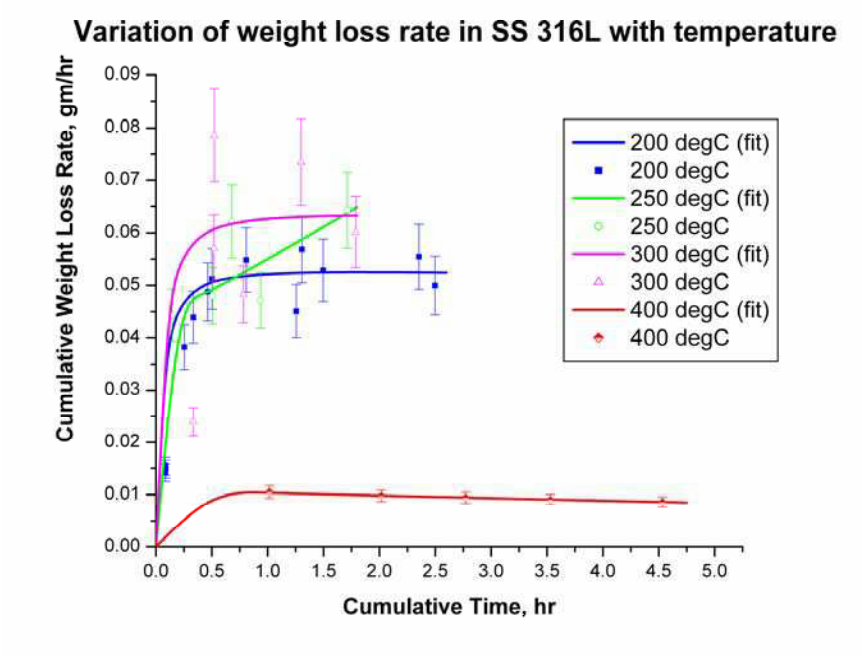

Fig. 5.2 – Cumulative weight loss rate (CWR) vs cumulative time in SS 316L

MDPR is calculated using the formula

$$\text{MDPR } (\mu / \text{hr}) = \frac{10^3 \Delta W}{(t.A.\rho)} \quad \text{------} \quad (2)$$

where ΔW= cumulative weight loss (gm) over a testing period of 't' hrs, A is the area of the specimen face (m^2) and ρ is the density (kg/m^3) of the specimen at the testing temperature.

The entire area of the specimen face is used for the calculation.

As can be seen Table 5.1 the hardness of 316L is low compared to that of the hard faced coatings. During deformation under cavitation loading SS 316L undergoes work hardening and therefore during the initial stages the surface deforms easily and high damage rate occurs

whereas with prolonged exposure the work hardening produced increases the hardness of the damaged layer and stabilizes the damage rate (Fig. 5.2).

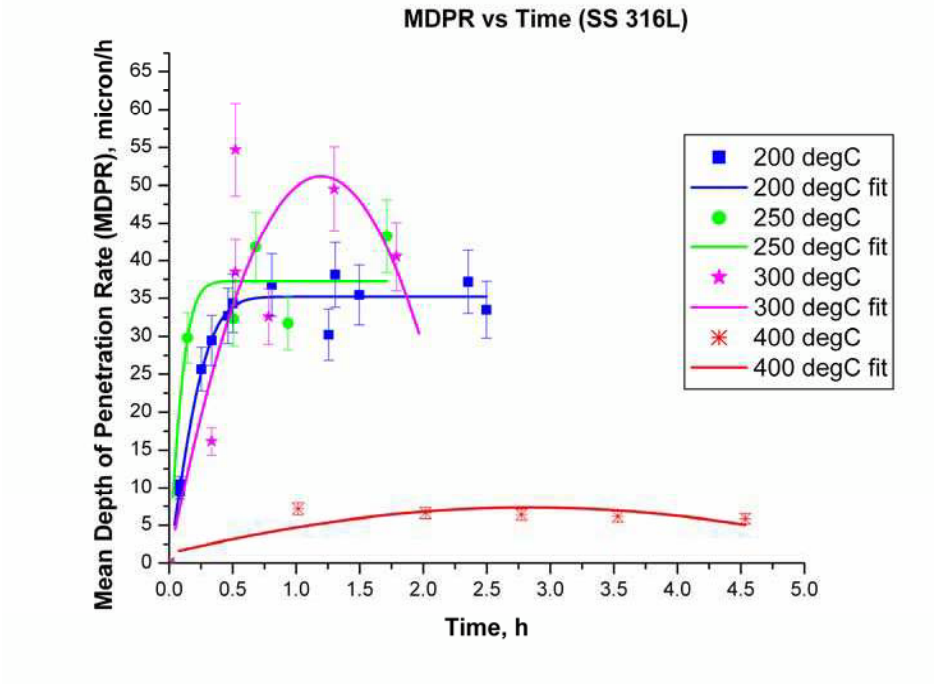

Fig. 5.3 – Mean Depth of Penetration rate (MDPR) vs cumulative time in SS 316L

It is seen from Figs. 5.2 and 5,3 that CWR and MDPR marginally increases when the temperature is raised from 200 ºC to 300 ºC and then substantially decreases on increase of temperature to 400ºC indicating that the damage rate / MDPR tends to a maximum between 300ºC and 400ºC. The MDPR curves also show that the rates at 200ºC, 250 ºC and 400 ºC have attained steady state.

Review of published literature [23, 10] on cavitation erosion tests done in sodium using vibratory device show that Dayer [23] has reported the occurrence of peak MDPR value in the temperature range 200ºC - 300ºC while Hammitt and Courbiere [10] have reported occurrence of

peak MDPR value in the range from 200ºC - 400ºC based on tests at CEA, Cadarache and three US laboratories.

5.2.1.2 Colmonoy 5 Hardfaced Coating

Cavitation erosion of Colmonoy5 in sodium was studied at four temperatures viz. 200ºC, 250ºC, 300ºC and 400ºC. At 200ºC two nos., at 250ºC three nos., at 300ºC two nos. and at 400ºC one nos. of specimen was tested (Tables A2.10 - A2.17). Fig. 5.4 shows the variation of cumulative weight loss with duration of testing for Colmonoy5. Fig. 5.5 shows the variation of rate of weight loss with time. The cumulative weight loss rate in the case of Colmonoy5 appears to be maximal between 250ºC and 300ºC. The MPDR is not shown as data for the density of Colmonoy5 at various temperatures is unavailable.

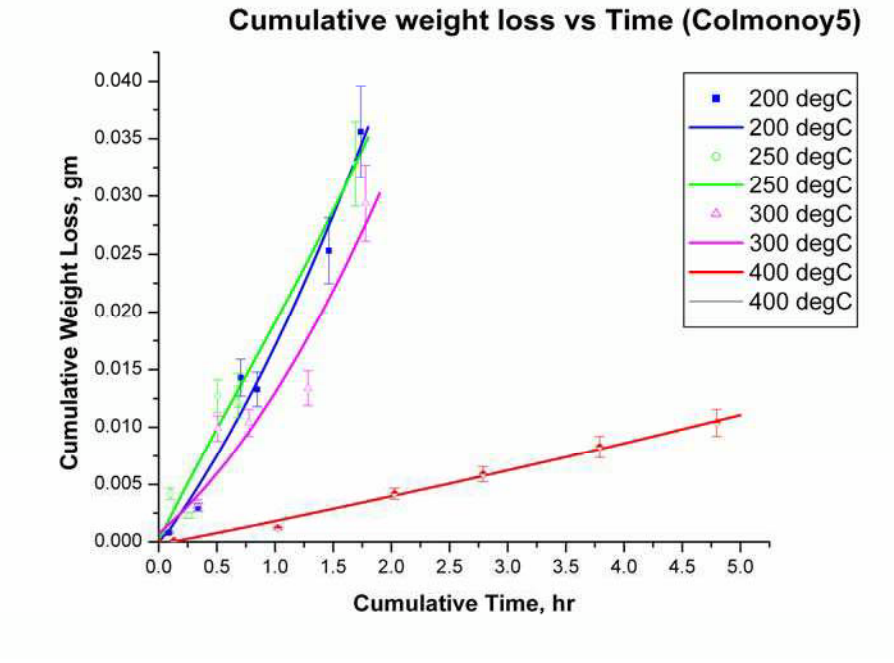

Fig. 5.4 – Cumulative weight vs cumulative time in Colmonoy5

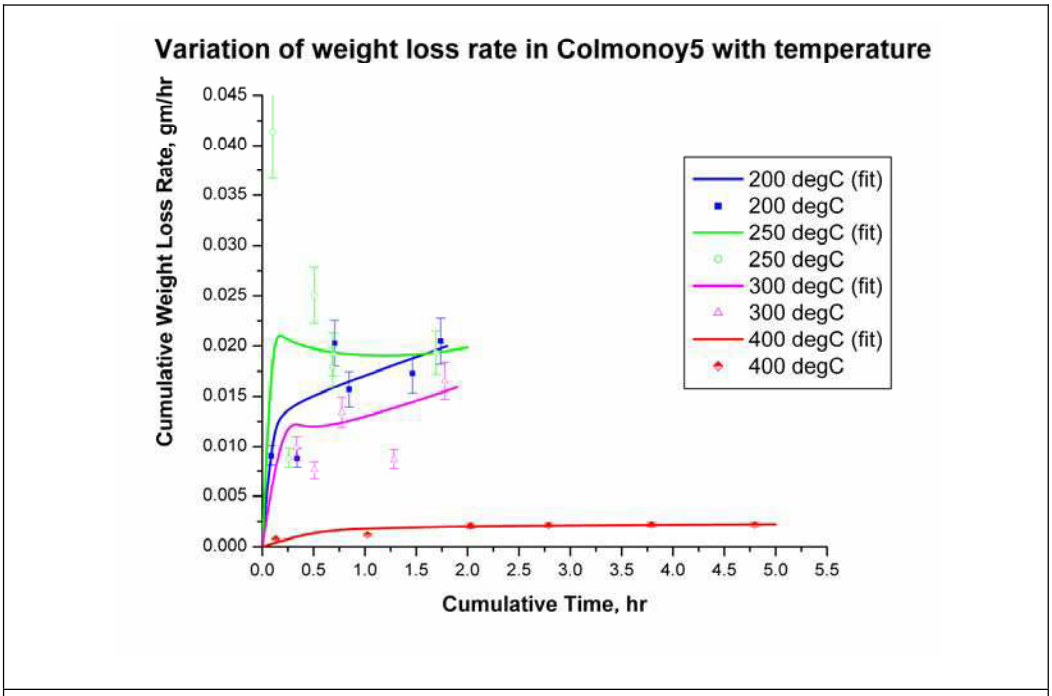

Fig. 5.5 – Cumulative weight loss rate vs cumulative time in Colmonoy5

5.2.1.3 Stellite6 Hardfaced Coating

Weight loss measurements were carried out for Stellite6 specimens subjected to cavitation test at four temperatures viz. 200ºC, 250ºC, 300ºC and 400ºC. Two specimens each were tested at temperatures of 200ºC and 250ºC and one each at 300ºC and 400ºC. (Tables A2.18 – A2.23).

Fig. 5.6 below shows the variation of cumulative weight loss vs time for Stellite6. Fig. 5.7 shows the variation of rate of weight loss with time. Although the number of data points at 300ºC is small, the peak erosion rate appears to be between 250ºC and 400 ºC. Hammitt and Courbiere [10] have reported a value close to 300ºC.

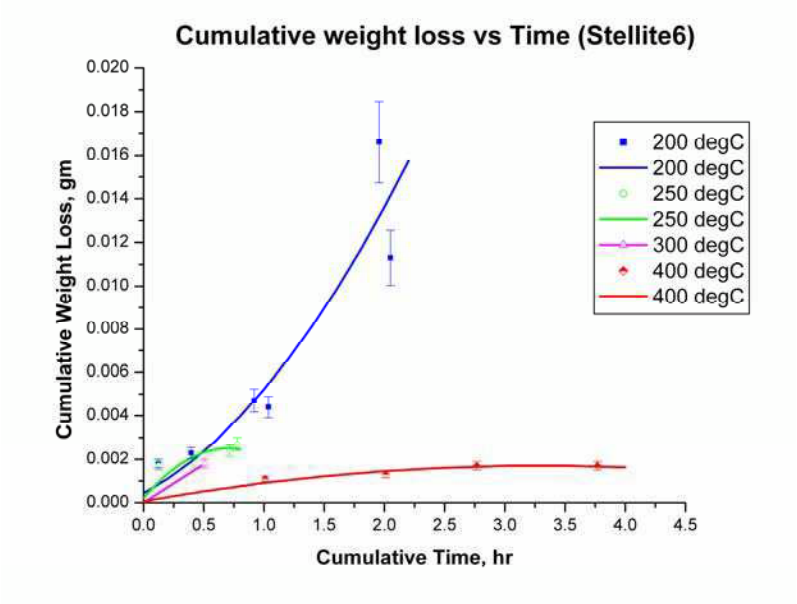

Fig. 5.6 – Cumulative weight vs cumulative time in Stellite6

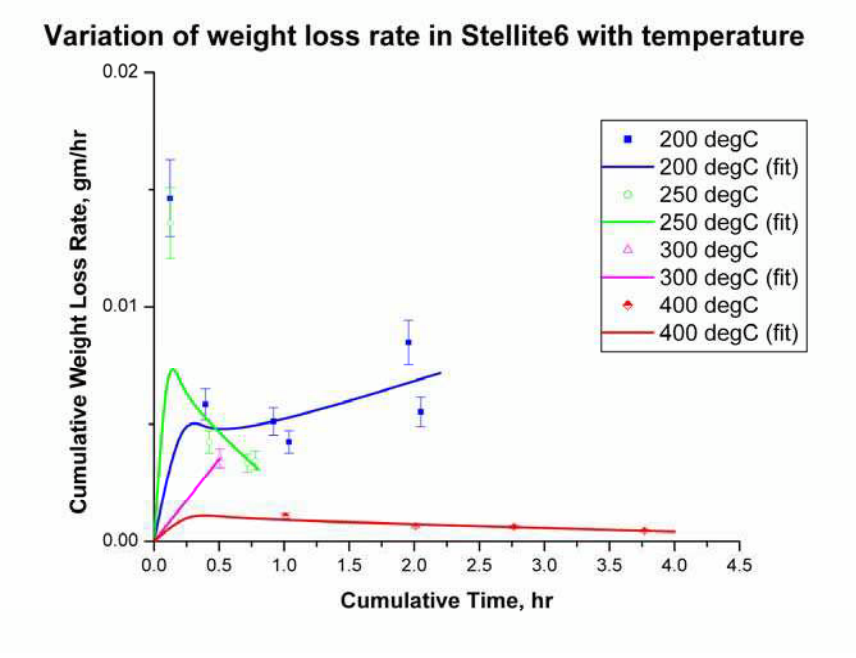

Fig. 5.7 – Cumulative weight loss rate vs cumulative time in Stellite6

5.2.1.4 Comparison between weight loss rates in SS316L, Colmonoy5 and Stellite6

Fig. 5.8 shows the comparison of the weight loss rates in SS 316L with the hardfaced specimens. Fig. 5.9 shows the comparison between weight loss rates in Colmonoy5 and Stellite6. It is evident from both figures that hard facing results in marked improvement in the cavitation damage resistance of SS 316L. It is also apparent that Stellite6 is more resistant to cavitation than Colmonoy5.

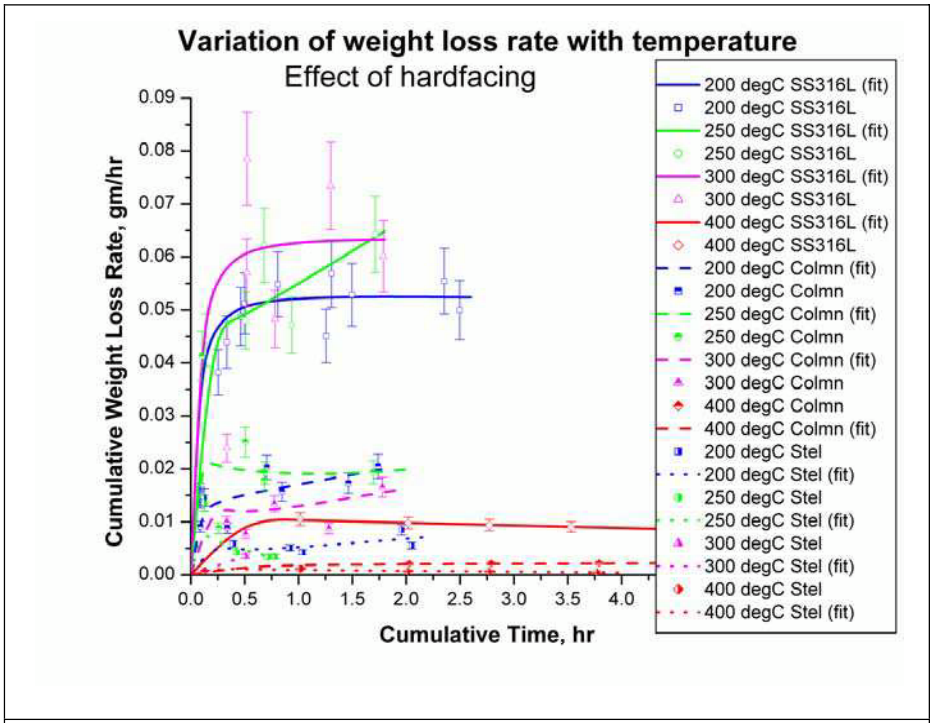

Fig. 5.8 – Comparison of cumulative weight loss rate in SS316L, Colmonoy5 and Stellite6

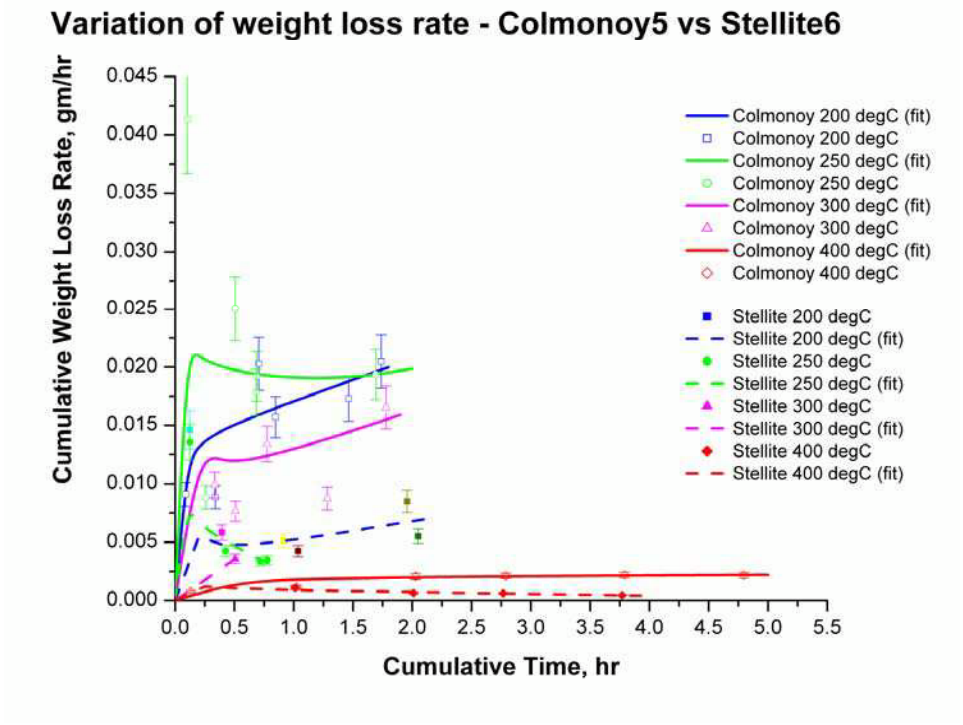

Fig. 5.9 – Comparison of cumulative weight loss rate in Colmonoy5 and Stellite6

5.2.2 Surface Damage

5..2.2.1 Austenitic Stainless Steel SS 316L

Fig. 5.10 shows the low magnification image of the specimen after testing. For short duration tests, a virtually unaffected rim is clearly visible (Fig. 5.10(a)) which is due to fluid dynamic edge effects [116, 117]. However, with extended duration the eroded area is observed to extend and cover almost the entire face of the specimen (Fig. 5.10(b)).

Fig. 5.10 (a) – SS 316 L specimen (A6) after 8 min. of testing in sodium at 250ºC

Fig. 5.10 (b) – The same specimen after 102 min. of testing in sodium at 250ºC

The presence of the undamaged rim, observed not only in stainless steel specimens but also in hardfaced specimens (Figs. 5.15, 5.16, 5.25, 5.26), is a characteristic of the bubble collapse mechanism in ultrasonic cavitation [118] . It is also seen that the damage increases from the periphery towards the central region of the specimen. The collapse of the bubbles in the periphery, initiated by the ultrasonic pressure variation, results in a propagation of the pressure wave towards the centre causing the bubbles near the centre to implode under larger pressure gradient resulting in higher damage near the centre than at the periphery. As the period of testing increases the peripheral portions also begin to show signs of erosion from the constant implosion of bubbles under the positive half of the oscillating ultrasonic pressure wave.

Also seen in Figs. 5.10 (b) is narrow annular regions in the periphery which have more damage than in the central region. This could be due to the presence of non uniform clusters of vapour bubbles on the surface of the specimen. The pattern of damaged regions of varying intensity is

similar to that reported by Dayer [23] on stainless steel specimens (Type 316 and 321) in liquid sodium using vibratory device operating at 15.5 kHz and 50 μ (peak to peak) amplitude.

Figs. 5.11 – 5.14 are the results of examination of the specimens under high magnification with a scanning electron microscope.

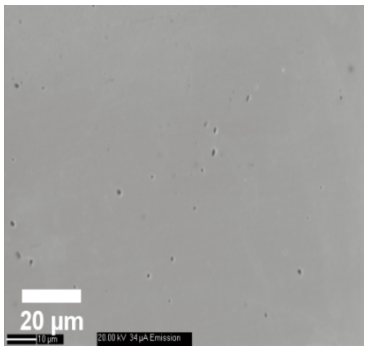

Fig. 5.11 – SEM of polished sample before test

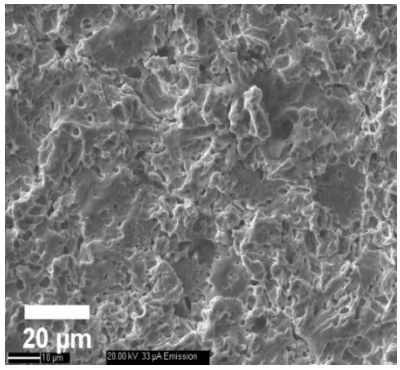

(a) Near edge

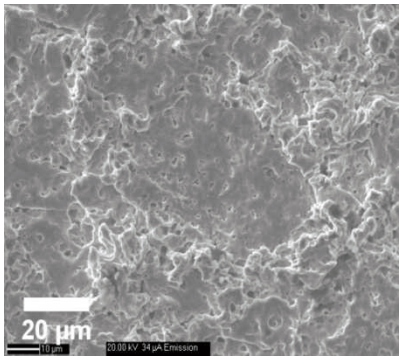

(b) Near middle

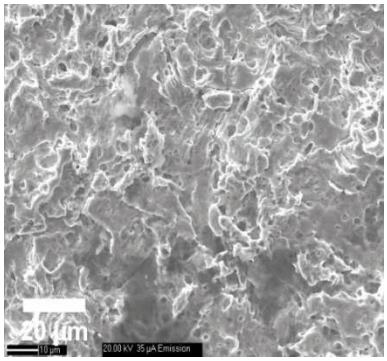

(c) Near opposite edge

Fig 5.12 – SEM of sample after 5 m 2 s

Fig. 5.11 is the SEM image of the specimen (in mirror finish condition) taken before test and Fig. 5.12 is the SEM images taken after 5 min. and 2 s. of testing in liquid sodium at 200ºC. It is seen from Fig. 5.12 to Fig. 5.14 that in SS 316L the surface damage produced is predominantly ductile with deep pits and small sized craters. Fig. 5.12(b) is the SEM image of a

region near the centre of the specimen. The features of the crater (almost circular shape and raised rim around the crater) are indicative of the crater having been formed by the impact of liquid microjet which is in fact the pre dominant damaging mechanism in vibratory cavitation damage. Figs. 5.12(a) and (c) are SEM images of regions near the periphery on either side of the central region. It is seen that at the centre the pits are smaller than those at the edges and the particles breaking off from the surface are more fine grained. These SEM images also indicate that damage is not uniform over the surface and there are alternate regions of coarse and finely eroded regions. This is possibly due to (i) variation in ultrasonic cavitation from the centre towards the periphery (ii) progressive collapse of bubbles from the outer periphery towards the centre.

Fig. 5.13 and 5.14 are some more SEM images of SS 316 L specimen early on during the testing and after prolonged exposure to cavitation. These images help in understanding the mechanism of cavitation damage in austenitic stainless steel. It is seen that during the initial exposure to cavitation shallow and wide craters with rounded ridges at the periphery are formed which on subsequent exposure develop into deep narrow pits with sharp ridges.

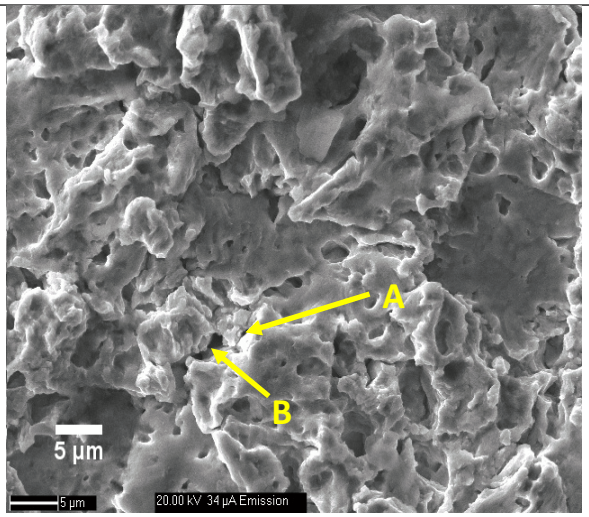

Fig. 5.13 – SEM sample of SS 316L – After cavitation in sodium (period = 5 min 2 secs, Temp = 200ºC)

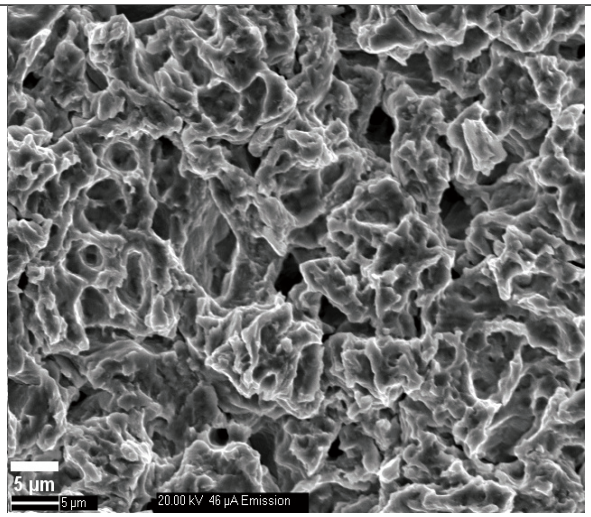

Fig. 5.14 – SEM sample of SS 316L – After cavitation in sodium (period = 141 min, Temp = 200ºC)

It is seen from Fig. 5.13 (and also reported in literature [119] that in SS 316L the accumulation of slip bands results in initiation of micro cracks (A). Plastic deformation then results in enlargement of the micro cracks and void formation. The adjacent voids coalesce leading to material removal (B). The resulting surface has the dimpled topography characteristic of damage in ductile materials. Fig. 5.14 shows the damage after prolonged exposure. It is seen that at this stage there is also material removal from the work hardened surface to produce gross pitting of the surface.

5.2.2.2 Colmonoy5 and Stellite6

Fig. 5.15 is a low magnification optical image Colmonoy5 specimen after testing in sodium at 250 ºC for 6 m 7 s. The unaffected rim, present in SS 316L and Stellite5 specimens, is visible here also.

Fig. 5.16 is a low magnification optical image of Stellite6 specimen after testing in sodium at 200 ºC for 7 m 23 s. The unaffected rim, similar to that for SS 316L specimen, is visible here.

Fig. 5.15 – Colmonoy5 (C3) after testing in sodium at 250ºC for 6 m 6 s

Fig. 5.16 – Stellite6 (S1) after testing in sodium at 200 ºC for 7 m 23 s

Fig. 5.17 to Fig.5.19 are the results of examination of the specimen under high magnification with a scanning electron microscope. While Figs. 5.17 and 5.18 are the SEM images at early stage of cavitation damage (after ~ 6 min of testing), Fig. 5.19 is the image after prolonged exposure to cavitation

Both the hardfaced coatings have a solidified dendritic microstructure. While in the case of Colmonoy5 the structure consists of borides and carbides dispersed in the interdendritic regions of a Ni base matrix phase, Stellite6 consists of interdendritic Cr rich carbides dispersed in Co rich matrix phase dendrites.

For Colmonoy 5 deposits it may be seen that damage is initiated at the interface between the hard second phase (borides or carbides) and the matrix. Figure 5.18 shows the damage at the interlamellar spacing of the eutectic mixture of matrix and hard second phase. It is observed that extended exposure to cavitation causes the removal of the hard second phase particles from the

matrix and the formation of pits as shown in Fig. 5.19. Also evident is severe deformation of the base matrix.

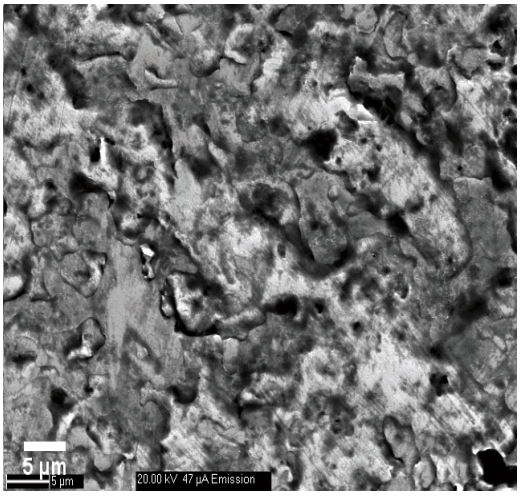

Dendrite phases and initiation of material removal at interdendritic regions

Fig. 5.17 – Colmonoy5 sample (C3) – After cavitation in sodium (period = 6 min 6 secs, Temp = 250 ºC

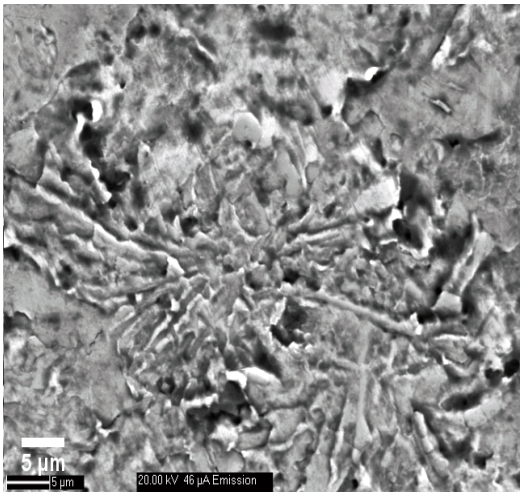

Flower like dendrite phases; material removal begins at hard interdendritic regions.

Fig. 5.18 – Colmonoy5 sample (C3) – After cavitation in sodium (period = 6 min 6 secs, Temp = 250 ºC

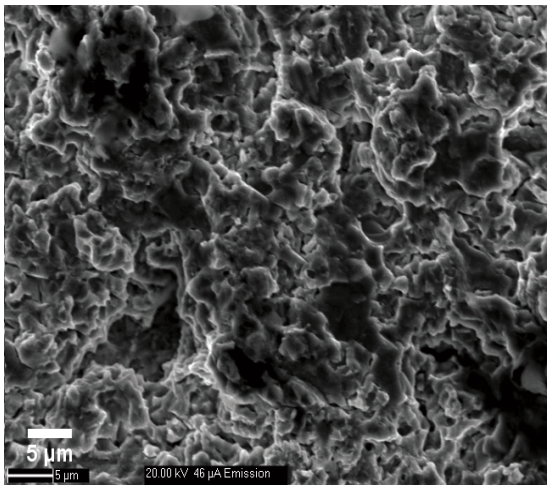

The voids are regions where the borides and carbides and portions of the base matrix are removed.

Fig. 5.19 – Colmonoy5 sample (C3) – After cavitation in sodium (period = 41 min, Temp = 250 ºC

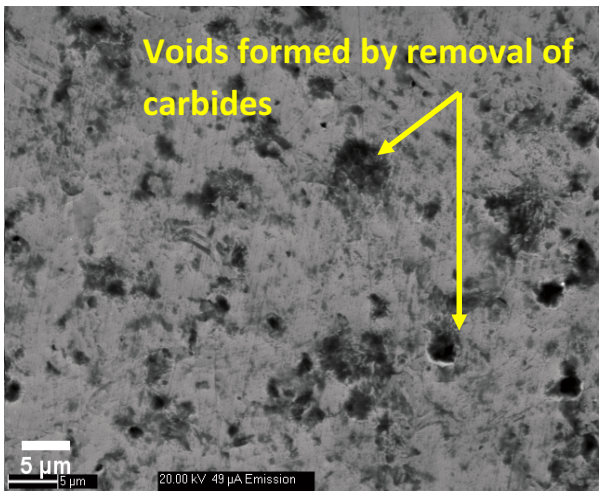

Cracks at carbide locations resulting in increased stress concentration and removal of carbide particles from these locations.
Fig. 5.20 – Stellite6 sample (S2) – After cavitation in sodium (period = 7 min 31 secs, Temp = 250 ºC

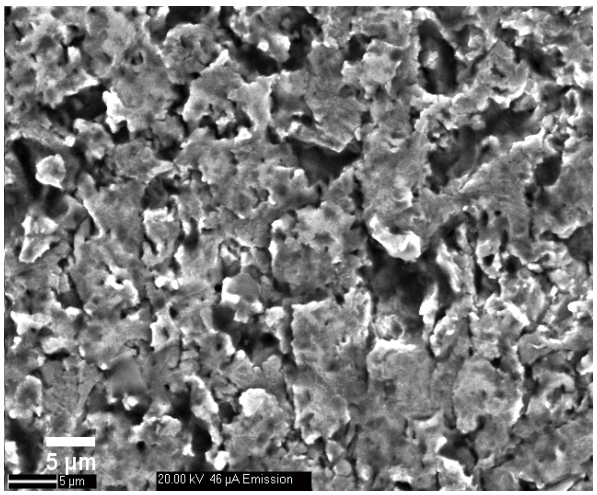

Further exposure results in damage propagation to the work hardened matrix
Fig. 5.21 – Stellite6 sample (S2) – After cavitation in sodium (period = 42 min, Temp = 250ºC

Figs. 5.20 and 5.21 are SEM images of the stellited specimen at an early stage and after prolonged exposure respectively. As in the case of Colmonoy5 deposit, damage begins in Stellite6 deposit also at the interface between carbides and the matrix. With the progress of cavitation, the carbides get dislodged from the surface initiating cracks in the work hardened matrix and subsequent weight loss. However, the deformation observed for the matrix phase is significantly different from those observed in the case of Colmonoy and the austenitic stainless steel.

5.2.3 Absolute Surface Roughness

The progression in absolute surface roughness of the three materials tested was analysed for a few specimens tested at 200 ºC. The absolute surface roughness of the selected specimens

was measured by means of a non-contact type optical profiler prior to start of testing and after every test thereafter. The results are shown in Fig. 5.22 and Fig. 5.23.

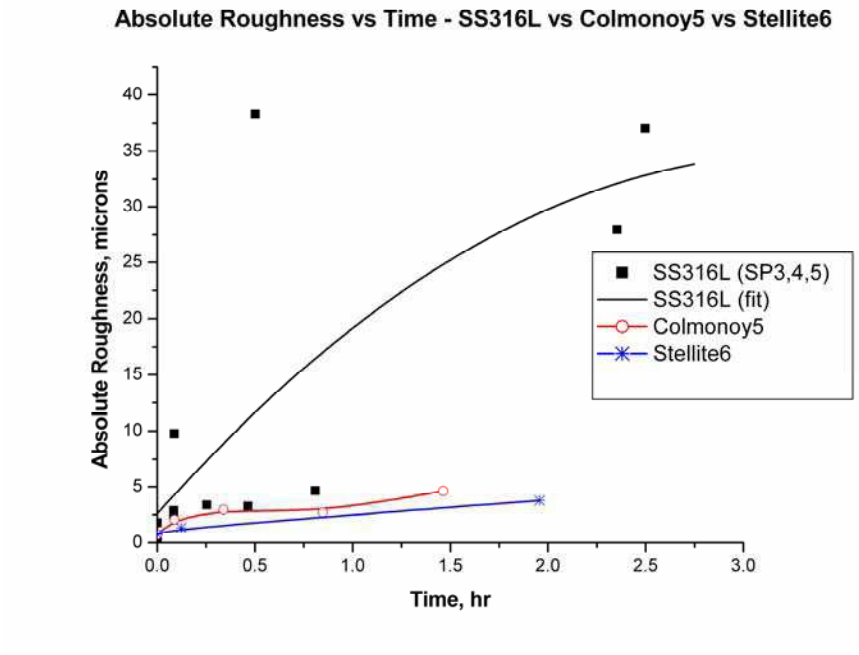

Fig. 5.22 – Progression of absolute surface roughness with cavitation damage (200 ºC)

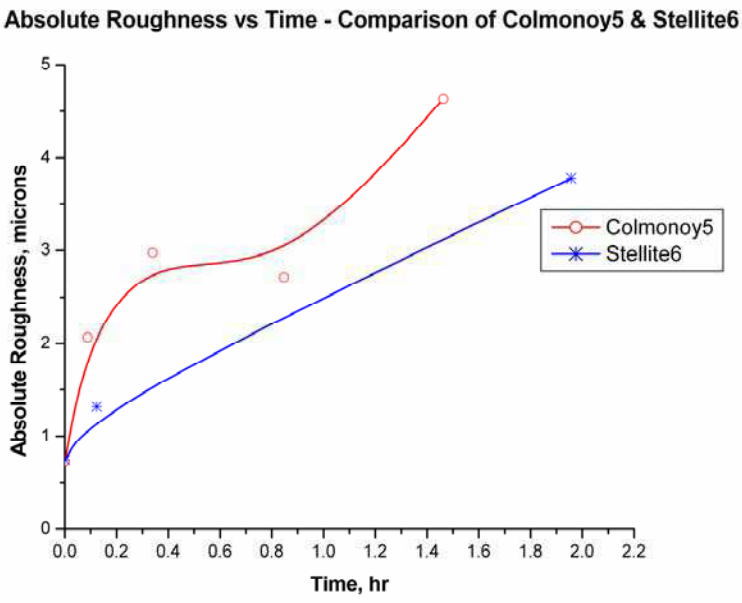

Fig. 5.23 – Comparison of progression of absolute surface roughness for Colmonoy5 and Stellite6 (200 ºC)

It is seen from a comparison of Fig. 5.22 with Fig. 5.8 and Fig. 5.23 with Fig. 5.9 that the absolute surface roughness is as much an indicator of relative ranking of resistance of materials to cavitation damage as is cumulative weight loss rate from cavitation.

Figs. 5.24 and 5.25 are plots of absolute surface roughness against cumulative weight loss rate. These figures corroborate the above conclusion that absolute surface roughness is a good indicator of cavitation damage resistance.

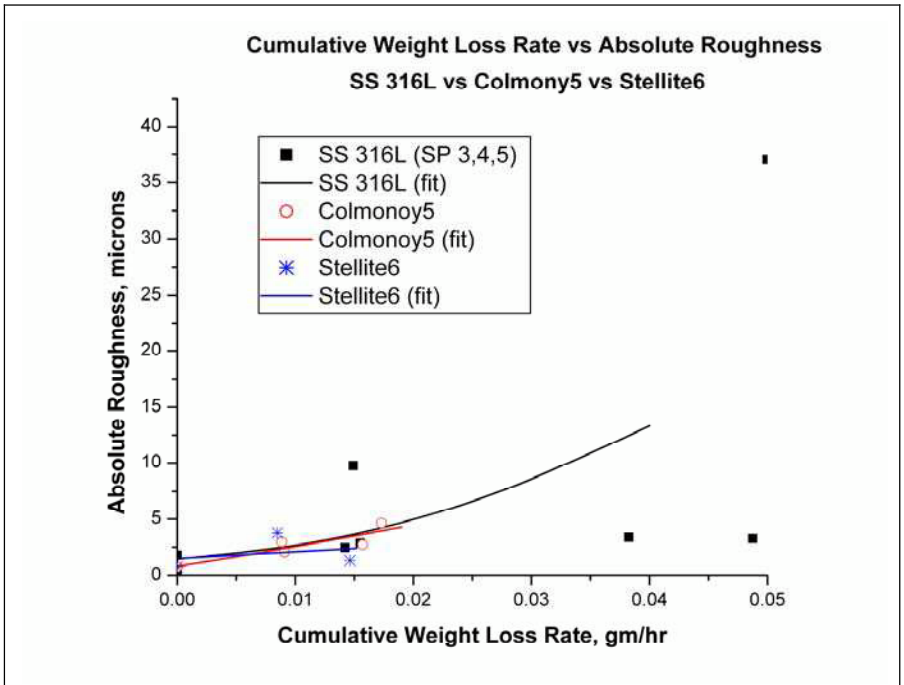

Fig. 5.24 – Comparison of absolute surface roughness and cumulative weight loss rate for all materials

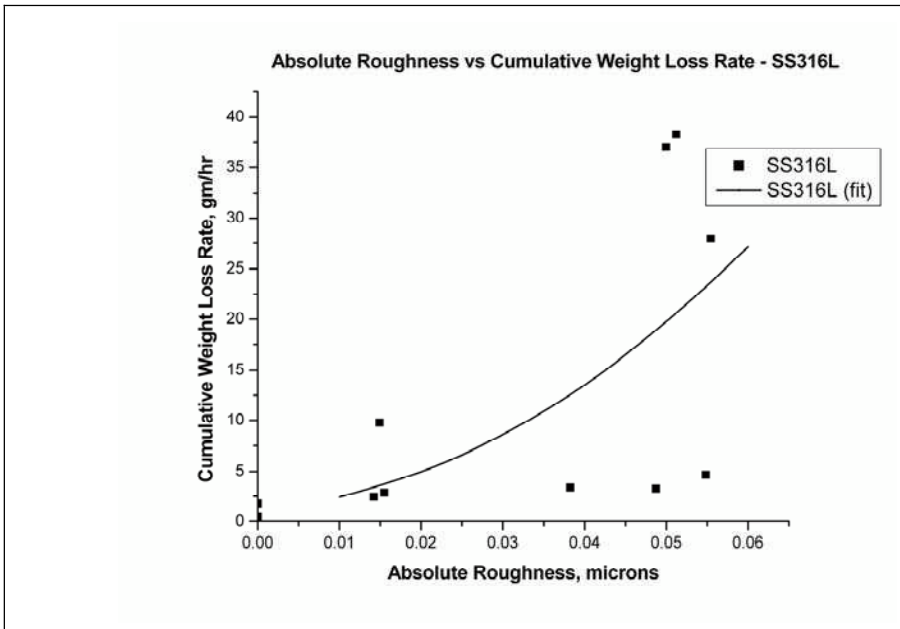

Fig. 5.25 – Comparison of absolute surface roughness and cumulative weight loss rate for SS316L

5.3 DISCUSSION

The marked reduction in the weight loss produced in the hard faced specimens compared to that produced in SS 316L may be attributed to the large variation in hardness between SS316L (HRB 95.6) and the hardfaced variants, viz.HRC 38.6 for Stellite6 and HRC 40.7 for Colmonoy5.

Hardness, however, is not the only property that affects resistance to cavitation damage. A comparison of the damage produced in Stellite6 and Colmonoy5 specimens show that although the measured hardness of Colmonoy5 is higher than that of Stellite6, the damage produced in Colmonoy5 is greater than that produced in Stellite6. This difference may be explained in terms of (i) the fracture toughness coefficient, K_{IC}, and (ii) the stacking fault energy (SFE).

As the damage during cavitation is caused by the repeating cyclic loading on the material surface due to bubble collapse, it is reasonable to expect that a material with higher fracture toughness will show better cavitation resistance than a material with lower fracture toughness. Table 5.2 gives the average (of three different temperatures, viz. room temperature, 149 ºC and 316 ºC) fracture toughness coefficients, K_{IC}, of Stellite6 and Colmonoy5 [120].

Table 5.2 – Fracture toughness coefficients of Stellite6 and Colmonoy5

Stellite6	35.6 $\pm$ 2.5 MPa $\sqrt{m}$
Colmonoy5	15.9 $\pm$ 3.0 MPa $\sqrt{m}$ 26.2 $\pm$ 2.7 MPa $\sqrt{m}$ (for another composition with increased Fe content due to dilution)
Although the chemical compositions of Stellite6 and Colmonoy5, reported in the above reference, are marginally different from that used in this work, this will not change the trend or the order of magnitude of the above values.	

It is seen that K_{IC} value for Stellite6 is higher than that of Colmonoy5; therefore although the hardness of Colmonoy5 is marginally higher than that of stellite6, the cavitation damage resistance of Stellite6 is better than that of Colmonoy5 as is evident from the experimental results.

Stacking fault energy is the energy stored in the crystal lattice due to interruption in the stacking sequence of the constituent atoms. Cavitation erosion is characterized by high strain and high strain rates of the order of $5*10^3$/s [29]. In such high strain rate processes work hardening is opposed by dynamic recovery and the stacking fault energy of the structure plays an important role in the damage process.

Colmonoy is a Ni base alloy while Stellite is a Co base alloy. Pure nickel has FCC structure while pure Co has HCP structure. The SFE of pure Ni (240 $\pm$ 50 mJ/m^2) [121] is higher than that of pure Cobalt (31 mJ/m^2) [122]. The presence of alloying elements tend to lower the SFE further.

When SFE is low (as in Stellite6) there is a greater probability for stacking faults to occur and the area of the resulting stacking fault is high [123]. The separation distance between adjacent partial dislocations is then large and the recombination of partial dislocations becomes difficult. The mobility of dislocations is thus reduced and deformation by cross slip and climb becomes difficult producing less dynamic recovery because the partial dislocations have to first recombine before cross slip can occur. This results in higher degree of strain hardening and flow stress saturation at higher strain value and planar slip then becomes the dominant deformation mechanism. On the other hand when the SFE is high as in Colmonoy5 (Ni-base matrix) cross slip occurs readily resulting in dynamic recovery, lesser degree of work hardening and saturation of flow stress at lower strain value. This is evident from the difference in the surface topography of the damaged surface as seen in Fig. 5.19 for Colmonoy 5 and Fig. 5.21, for Stellite 6 respectively.

Another mechanism that affects the damage resistance of Stellite is the change in structure of the matrix. Pure Co exists in two allotropic forms, viz low temperature HCP and high temperature FCC [124]. However, Stellite (which is a Co rich solid solution alloyed with Cr,W and C) retains its FCC phase even at lower temperatures (the alloying elements Cr and W increase the transformation temperature). Low temperature deformation under high stress induces FCC to HCP transformation depending on the SFE of the alloy and the temperature of deformation. This transformation absorbs some of the bubble collapse energy and results in work hardening of the surface thus reducing the weight loss due to cavitation damage. It is to be also noted that HCP structure has less operative slip systems when compared to FCC structure. This could also be the reason for the differences in the topography of the damage observed in Colmonoy 5 and Stellite 6 hardfaced coatings (Fig. 5.19 vis-à-vis Fig. 5.21).

Analysis of wear debris in cavitation erosion tests [124] on Stellite6 has shown that not only is the structure of the debris largely HCP but also that the volume fraction of HCP on the surface of the Stellite6 test sample is found to significantly increase during the course of the test thus giving credence to the conclusion that the cavitation damage resistance of Stellite6 is derived from the matrix and improved by the FCC to HCP transformation.

The resistance to cavitation damage in Co base alloy such as Stellite6 is therefore higher than that in Ni base alloy such as Colmonoy5.

5.3.1 Effect of temperature

The variation with temperature may be explained in terms of liquid properties. Increase in liquid sodium temperature results in (a) increase in the vapor pressure of the liquid (ii) increase in the liquid compressibility (iii) reduction in the density, surface tension, viscosity and dissolved gas content.

Increase in vapor pressure results in (i) an increase in the bubble population / increase in bubble size at the end of expansion in which tends to increase the energy transferred to the solid at the end of collapse thereby resulting in increased damage (ii) increase in back pressure at the end of collapse which tends to oppose collapse thereby resulting in reduced damage.

Increase in liquid compressibility reduces the energy transferred to the solid thereby reducing damage. Similarly reduction in density limits the transfer of energy to the solid.

Reduction in viscosity permits expansion of the bubble to a larger size and enables more complete collapse while reduction in surface tension aids expansion and opposes collapse.

Decrease in equilibrium gas content reduces the back pressure opposing collapse thereby increasing damage.

The net effect of the above factors results in the MDPR attaining a peak value at an intermediate temperature between melting point and boiling point. As mentioned earlier, peaking of MDPR, at a temperature between melting point and boiling point, in tests with ultrasonic vibratory device sodium is also reported in literature [23, 10]. It may be noted that this is also observed in tests in water wherein the peak value of MDPR occurs approximately midway between the melting point and the boiling point [125].

The effect of temperature was studied by solving the Gilmore equation (3.16) for four different temperatures, viz. 150ºC , 200ºC, 300ºC, 400ºC and 500ºC. The damaging pressure was computed using equation 3.29. The results are summarized in Table 5.3.

Table 5.3 – Effect of temperature on jet velocity and collapse pressure - From solution of Gilmore's equation

Sl. No.	Temp. ºC (K)	Vel of sound, m/s	Max radius, mm	Min. radius, μm	Jet velocity, m/s	Collapse pressure, MPa
1	150 (423)	2480	1.36	17.2	1854	4202
2	200 (473)	2460	1.35	17.1	1892	4201
3	300 (573)	2411	1.34	16.6	1995	4234
4	400 (673)	2361	1.32	17.9	1897	3846
5	500 (773)	2313	1.31	26	1390	2680

It is seen from Table 5.3 that the collapse pressure is more or less the same between 150ºC and 300ºC and decreases with further increase in temperature. In the solution of Gilmore's equation the effect of liquid properties such as density, vapor pressure, viscosity, surface tension and compressibility is accounted. However, the effect of heat transfer between the bubble contents and the liquid and the effect of dissolved gas content are not considered. Moreover, no consideration of the distribution of bubbles is made. These effects will influence the cushioning effect of surrounding bubbles on the collapse pressure and affect both the magnitude and variation in damage with temperature.

The normal operating temperature of the cold pool in PFBR is 397 ºC and the hot pool is 547 ºC. The above results indicate that for components in the cold pool the damage due to cavitation under normal operation will be lower than the maximum damage rate.

5.4 COMPARISON OF DAMAGE IN SS316L, COLMONOY5 AND STELLITE6 SPECIMENS

SS 316L(A15) – 55 min.

Colmonoy5(C3) – 41 min.

Stellite6(S3) – 46 min.

Temperature - 250ºC

Fig. 5.26 – Comparison of cavitation damage produced in SS 316L, Colmonoy5 and Stellite6

Fig. 5.26 is a comparison of SS 316L, Colmonoy5 and Stellite6 specimens after testing at 250 ºC for ~ 1 hr while Fig. 5.27 is a comparison of SS 316L, Colmonoy5 and Stellite6 specimens after testing at 400ºC for 1 hr



SS 316L	Colmonoy5	Stellite6

After testing for 1 h at 400ºC

Fig. 5.27 – Comparison of cavitation damage produced in SS 316L, Colmonoy5 and Stellite6

From the Figs. 5.26 & 5.27 the marked reduction in cavitation damage with hardfacing is evident. Also clear is the improved resistance of Stellite6 to cavitation damage vis-à-vis Colmonoy5.

CHAPTER 6

CONCLUSIONS AND SCOPE FOR FURTHER WORK

CHAPTER 6 : CONCLUSIONS AND SCOPE FOR FURTHER WORK

6.0 CONCLUSIONS

In fast reactor systems, it is often required to operate with incipient cavitation because of the need to use compact and cost effective systems. The deleterious effects of cavitation are minimised by improving the hydraulic design and limiting the progress of cavitation. In addition to improving hydraulics, proper material selection and surface treatment, such as hard facing, are also important to combat damage from cavitation and reduce maintenance frequency. Increasing life of equipment and ensuring minimal maintenance is an important goal towards achieving uninterrupted plant availability.

Austenitic stainless steel is the structural material used in fast reactors. Tribological performance can be improved wherever required using hardfacing with cobalt base or nickel base alloys. The major drawback of using Cobalt base hardfacing alloys is the formation of the isotope Co^{60} from the transmutation of Co^{59} in the radioactive reactor environment. Co^{60} is a γ emitter (1.17Mev and 1.33Mev) with a half life of 5.3 years and therefore poses difficulties during material handling when components are removed for repair / maintenance. However, Co^{60} is known to have good wear resistance. Fluid dynamic properties also influence cavitation damage and it is known that the damage produced in sodium is much more that in water.

Hence this study was carried out to establish a facility to study cavitation erosion in flowing sodium and to evaluate cavitation damage resistance of the common structural material

in the reactor (austenitic stainless steel) and the hardfaced coatings made of Stellite6 and Colmonoy5. The following are the major conclusions :

(i) A facility was designed and commissioned for evaluation of cavitation damage in materials in liquid sodium in the temperature range of 200 - 400°C using vibratory cavitation technique.

(ii) Cavitation erosion resistance of hardfaced coatings is significantly better than that of the austenitic stainless steel 316LN. Hard carbides and borides resists deformation of the surfaces during bubble collapse and this gives the cavitation erosion resistance to hardfaced coatings. In contrast, austenitic stainless steel surface deforms easily under cavitation resulting in damage. Stellite 6 hardfaced coating is more resistant to cavitation erosion than Colmonoy 5 coatings though hardness is higher for the latter. This is attributed to higher fracture toughness and lower stacking fault energy of the former. Transformation of FCC matrix phase of Stellite 6 coating to HCP under stress is also known contribute to the improved wear resistance of the alloy. All the three alloy systems show an initial increase in cavitation erosion with temperature followed by a decrease in cavitation erosion with further increase in temperature. This is similar to the variation of cavitation erosion with temperature reported in water. This variation is attributed to variation in properties of the liquid medium that influence cavitation erosion.

(iii) It is observed that the evaluation of cavitation damage resistance on the basis of roughness measurement results in a similar ranking of various materials as that from weight loss due to cavitation damage.

6.1 SCOPE FOR FURTHER WORK

The experiments in this work were done in a static facility using vibratory cavitation. The effect of flow velocity may be studied in future work to understand the effect of flowing sodium to damage in a vibratory facility. This arrangement will be more convenient to study the effect of cavitation damage in a flowing system, when compared to the alternative system comprising a venturi, especially with respect to maintaining a leak tight sealing which is very crucial for a sodium system.

In the past attempts have been made to correlate cavitation damage resistance with macroscopic material properties (such as hardness, ultimate tensile strength, yield strength, Young's modulus, etc.) with limited success. The results here show that microscopic properties like SFE and fracture toughness also influence damage resistance. However, values of these properties are more difficult to come by published literature, especially for alloys and hardfacing materials. Data analysis of pure metals, and alloys wherever published literature is available, to explore relationships between microscopic properties and erosion damage can provide more insight on the influence of these properties towards improving cavitation damage resistance.

Fluid dynamic properties also have a strong influence on the damage produced. It is therefore useful to study the influence of fluid properties on cavitation damage using a surrogate liquid by classifying whether the damage produced is due to inertial effects or thermal effects and modeling the relevant properties affecting damage

Experiments to study the effect of surface treatment methods such as nitriding, hard chrome plating, laser surface modification etc. in improving cavitation damage resistance in sodium holds promise.

Another area where further work can be carried out is in the area of theoretical modeling of bubble collapse. In Chapter 3, the collapse pressure produced during collapse of a single bubble was modelled. In reality there will be a population of bubbles of varying sizes and distributed at varying distances from the specimen surface in the cavitation zone in the cavitation zone. The collapse pressure generated by the implosion of a vapor bubble will be influenced by that produced by the surrounding bubbles; moreover the energy transferred to the specimen surface will be attenuated by the neighbouring bubbles in the vapor cluster. Modelling these effects (eg. assuming a normal distribution of bubbles in space and a Monte Carlo simulation of collapse of bubbles) will provide more insight into the collapse process.

REFERENCES

REFERENCES

1. F.G. Hammitt, Detailed cavitation flow regimes for centrifugal pumps and Head vs NPSH curves, Report no. UMICH 01357-32-I, University of Michigan, Dec. 1974.
2. S.C Chetal, V. Balasubramaniyan, P. Chellapandi, P. Mohanakrishnan, P. Puthiyavinayagam, C.P Pillai, T.K Shanmugam, C. Sivathanu Pillai, The design of the prototype fast breeder reactor, Nuclear Engineering and Design, 236 (2006), 852-860.
3. S.L Mannan, S. C Chetal, Baldev Raj, S.B Bhoje, Selection of materials for prototype fast breeder reactor, Transactions of the Indian Institute of Metals, 56 (2), 2003, pp. 155-178. ISSN 0019-493X
4. Status of liquid metal cooled fast reactor technology, IAEA-TECDOC-1083, April 1999.
5. S.G.Joshi, A.S.Pujari, R.D.Kale and B.K.Sreedhar, Cavitation studies on a model of primary sodium pump, Proceedings of FEDSM'02, The 2002 Joint US ASME European Fluids Engineering Summer Conference, July 14-18,2002 Montreal, Canada.
6. R.Bisci, G. Muret, J. Teulon, Cavitation problems in fast reactor fuel subassemblies, IWGFR specialists' meeting on 'Cavitation in sodium and studies of analogy with water as compared to sodium', April 12-16, Cadarache, France.
7. Y.S Cha, P.R Huebotter, J. Hopenfeld, A survey of LMFBR cavitation technology in the USA, IWGFR specialists' meeting on 'Cavitation in sodium and studies of analogy with water as compared to sodium', April 12-16, Cadarache, France
8. Dowson and Taylor, Cavitation in bearings, Ann. Rev. Fluid Mech. 1979.11 : 35-66.
9. Shuji Hattori, Norihiro Mikami, Cavitation erosion resistance of stellite weld overlays, Wear, 267 (2009), 1954–1960.

10. F.G Hammit, P. Courbiere, Sodium cavitation test in vibratory facility, International Working Group on Fast Reactors (IWGFR-9) - Specialists meeting on cavitation in sodium and studies of analogy with water as compared to sodium, Cadarache, France, (April 12-16, 1976).

11. Y. Iwai, T. Okada and T. Fujieda, Effects of hard chromium plating on cavitation erosion, Wear, 128(1988), 189-200.

12. T. Okada and Y. Iwai, Effects of plating on cavitation erosion, Wear, 124 (1988) 21-31.

13. Alicja Krella, Andrzej Czyzniewski, Cavitation erosion resistance of nanocrystalline TiN coating deposited on stainless steel, Wear, 265 (2008), 953-970.

14. Alicja Krella, Andrzej Czyzniewski, Cavitation erosion resistance of Cr-N coatings deposited on austenitic stainless steel at various temperatures, Wear, 265, (2008), Pages 72-80.

15. S.J Pawel, Assessment of cavitation erosion resistance of 316LN stainless steel in mercury as a function of surface treatment, Journal of Nuclear Materials, 343 (2005), 101-115.

16. M. Haijan, A. Abdollah-zadeh, S.S Rezaei-Nejad, H. Assad, S.M.M Hadavi, K. Chung, M. Shokouhimehr, Improvement in cavitation erosion resistance of AISI 316 stainless steel by friction stir processing, Applied Surface Science, 308 (2004), 184-192.

17. Kwok Chi Tat, Laser surface modification of stainless steels for cavitation erosion resistance, PhD Thesis, Dept. of Applied Physics, The Hong Kong Polytechnic University, 1998.

18. A.K Bhaduri, R. Indira, S.K Albert, B.P.S Rao, S.C Jain, S. Asokkumar, Selection of hardfacing material for components of the Indian Prototype Fast Breeder Reactor, Journal of Nuclear materials, 334 (2004), 109-114.

19. Jeffrey H. Boy, Ashok Kumar, Patrick March, Paul Willis and Herbert Herman, Cavitation and erosion resistant thermal spray coatings, Construction Productivity Advancement Research (CPAR) Program, US Army Corps of Engineers, Construction Engineering Research Laboratories, USACERL Technical Report 97/118, July 1997.

20. Ryan Sollars and Alfred D. Beitelman, Cavitation resistant coatings for high power turbines, Civil Works Hydropower R&D Program, US Army Corps of Engineers, Engineering Research and Development Centre, ERDC/CERL, TR-11-21.

21. Stanley G. Young and John C. Freche, A review of NASA research to determine the resistance of materials to cavitation damage in liquid metal environments, NASA Technical Memorandum, NASA TM X-52956

22. Stanley G. Young and James R. Johnston, Accelerated cavitation damage of steels and superalloys in liquid metals, NASA Technical Note, NASA TN D-3426.

23. N.F Dayer, Some observations on cavitation and its effects in liquid sodium, Central Electricity Generating Board, Research Division, Berkeley Nuclear laboratories, Rd/B/N3719, October 1976.

24. A. Thiruvengadam and H.S Preiser, Cavitation damage in liquid metals, prepared for National Aeronautics and Space Administration, contract, NAS 3-4172, Hydronautics, incorporated research in hydrodynamics, NASA CR-72035, Nov. 1965.

25. Sergey F. Shepelev, Status of BN-1200 project development, JSC Afrikantov OKBM (available at https://www.iaea.org/NuclearPower/Downloadable/Meetings/2015/2015-05-25-05-29-NPTDS/Russian_Projects/31_BN-1200_-_Obninsk_-_Shepelev_S.F._-_May_2015.pdf).
26. Rayleigh, Lord, (1917), On the pressure developed in a liquid during the collapse of a spherical cavity, Philosophical magazine series 6, 34:200, 94-98.
27. R.T Knapp, J.W Daily and F.G Hammitt, Cavitation, McGraw Hill, 1970.
28. Frederick G. Hammit, Charles L. Kling, Terry M. Mitchell, Edward E. Timm, Asymmetric cavitation bubble collapse near solid objects, Report no. UMICH-3371-6-I, Cavitation and multiphase flow laboratory, University of Michigan, Nov. 1970.
29. Ki Han Kim, Georges Chahine, Jean-Pierre Franc, Ayat Karimi, Advanced experimental and numerical techniques for cavitation prediction, Springer.
30. K.A Morch, On the collapse of cavity clusters in flow cavitation, Cavitation and inhomogenities in underwater acoustics, Proc. of the frst international conference, Gottingen, Federal Republic of Germany, July 9-11, 1979, pp. 95-100.
31. Y. Tomita and A. Shima, Mechanisms of impulsive pressure generation and damage pit formation by bubble collapse, Journal of Fluid Mechanics (1986), vol. 160, pp. 535-564.
32. M.S Plesset, The dynamics of cavitation bubbles, ASME Journal of Applied Mechanics, 71, pp 277-282, 1949.
33. B.E Noltingk and E.A Neppiras, Cavitation produced by ultrasonics, Proceedings of the Physical Society Section B, 63(9), pp 674-685.
34. H. Poritsky, 1952 (in F. Ronald Young, Cavitation, 2015).

35. H.G Flynn, Physics of acoustic cavitation in liquids, Physical Acoustics, Vol 1, Part B, W.P. Mason (ed.), Academic press, chap 9, p. 76, 1964.
36. C. Herring, 1941 (in [17])
37. Forrest R Gilmore, Growth or collapse of a spherical bubble in a viscous compressible liquids, Report no 26-4, Hydrodynamics laboratory, California Institute of Technology, April 1, 1952
38. Richard D. Ivany, Collapse of a cavitation bubble in viscous, compressible liquid – Numerical and experimental analysis, PhD thesis, Univ. of Michigan, April 1965.
39. A.J Stepanoff, Cavitation Properties of Liquids, ASME J. Eng. Power, 86 (1964), 195–199.
40. L.W Florschuetz and B.T Chao, On the mechanics of vapor bubble collapse, Journal of Heat Transfer, Trans. ASME, May 1965, pp. 209-220
41. H.S Preiser, A. Thiruvengadam and C.E Couchman III, Cavitation damage in liquid sodium, Technical report 285-1, NASA CR-54071, April 1964
42. Robert Hicking and Milton S Plesset, Collapse and rebound of a spherical bubble in water, The physics of fluids, vol. 7, no. 1, 1964, pp. 7-14.
43. M.S Plesset, Shock waves from cavity collapse, Philosophical Transcations A, The Royal Society, vol. 260, issue 1110, July 1966.
44. T.B Benjamin and A.T Ellis, The collapse of cavitation bubbles and the pressures produced against solid boundaries, Phil. Trans. R. Soc. A, 260, 221, 1966.
45. Charl F. Naude and Albert T. Ellis, On the mechanism of cavitation damage by non hemispherical cavities collapsing in contact with a solid boundary, Trans. ASME, Journal of Basic Engineering, D83, 1961, 648.

46. Milton S Plesset and Richard B Chapman, Collapse of an initially spherical vapor cavity in the neighborhood of a solid boundary, J. Fluid Mech. (1971), vol. 47, part 2, pp. 283-290.
47. T.M Mitchell, F.G Hammitt, Asymmetric cavitation bubble collapse, Report no. UMICH-03371-6-T, The University of Michigan, March 1971.
48. M.S Plesset and A.T Ellis, On the mechanism of cavitation damage, Trans. ASME, 77, 1055-1084, Oct. 1955.
49. Janusz Steller, Boleslaw G. Giren, International cavitation erosion test final report, 560/1519/2015, ISSN 0239-9091, Gdansk, 2015.
50. Frederick G. Hammitt, Cavitation and multiphase flow phenomena, McGraw Hill, 1980.
51. M.J. Robinson and F.G. Hammitt, Detailed damage characteristics in a cavitating venturi, project 03424-30-I, Internal report no. 30, June 1966.
52. ASTM-G32-10, Standard test method for cavitation erosion using vibratory apparatus.
53. T. Momma and A. Lichtarowicz, A study of pressures and erosion produced by collapsing cavitation, Wear 186-187 (1995) 425-436.
54. Edward Grist, Cavitation and the centrifugal pump – A guide for pump users, Taylor & Francis, 1999.
55. ASTM G134-10, Standard test method for erosion of solid materials by cavitating liquid jet.
56. Janusz Steller, International Cavitation Erosion Test and final quantitative assessment of material resistance to cavitation, Wear 233-235 (1999) 51-64.

57. A.A Collinson, The onset of cavitation in pressure dropping devices in water and sodium, IWGFR specialists' meeting on 'Cavitation in sodium and studies of analogy with water as compared to sodium', April 12-16, 1976, Cadarache, France.
58. Yves Lecoffre, Cavitation Bubble Trackers, AA Balkema, Rotterdam/Brookfield, 1999.
59. P. Courbiere, Cavitation erosion in 400°C sodium flow, IWGFR specialists' meeting on 'Cavitation criteria for designing mechanisms working in sodium application to pumps, Interatom GmbH, Federal republic of Germany, 28-29 Oct. 1985.
60. P. Courbiere and P. Lecoz, Cavitation in pumps : Research and development in France, IWGFR specialists' meeting on 'Cavitation criteria for designing mechanisms working in sodium application to pumps, Interatom GmbH, Federal republic of Germany, 28-29 Oct. 1985.
61. W. Marth, A review of the collaborative programme on the European Fast reactor (EFR).
62. Ramon Garcia, Comprehensive cavitation damage data for water and various liquid metals including correlations with material and fluid properties, PhD dissertation, University of Michigan, 1966.
63. R. Garcia and F.G Hammitt, Cavitation damage and correlation with material and fluid properties, Internal report no. 05031-11-1, The University of Michigan, Sept. 1966.
64. H.S Preiser, A. Thiruvengadam and C.E Couchman III, Cavitation damage in liquid sodium, Technical report 285-1, NASA CR-54071, April 1964.
65. F.G Hammitt, European Sodium Cavitation Research – State of the art, Report no. UMICH 01357-29-I.

66. F.G Hammitt, O.S.M Ahmed, J.B Hwang, M.K De, A. El Hasrouni and J.P Tullis, Development and calibration of wave guide acoustic probe system for bubble collapse spectrum measurement in vibratory and venturi system, Report no. UMICH 013503-4-1, Sept. 1975.

67. M.K De, Scott A. Barber, F.G Hammitt, Pressure probe calibration, Report no. UMICH 014456-1, The University of Michigan, July 1976.

68. Tsunenori Okada, Yoshiro Iwai, Shuji Hattori, Norio Tanimura, Relation between impact load and damage produced by cavitation bubble collapse, Wear 184 (1995) 231-239.

69. Soumitra Singh, Jin-Keun Choi, Georges L. Chahine, Characterization of cavitation fields from measured pressure signals of cavitating jets and ultrasonic horns, Journal of fluids engineering, Trans ASME, September 2013, vol. 135, 091302-1 to 091302-11.

70. Jean-Pierre Franc, Michel Riondet, Ayat Karimi and Georges L Chahine, Impact load measurements in an erosive cavitating flow, Journal of fluids engineering, Trans ASME, December 2011, vol. 133, 121301-1 to 121301-8.

71. Shuji Hattori, Hiroyuki Mori and Tsunenori Okada, Quantitative evaluation of cavitation erosion, Journal of fluids engineering, Trans. ASME, March 1998, vol. 120, pp. 179-185.

72. David Carnelli, Ayat Karimi and Jean-Pierre Franc, Application of spherical nanoindentation to determine the pressure of cavitation impacts from pitting tests, J. Mater. res., Vol. 27, Jan. 14, 2012, pp 91-99.

73. Jin-Keun Choi and Georges L. Chahine, Quantitaive evaluation of erosive cavitation pressure field from pits in material : fact or myth ?, Journal of physics conference series, Dec. 2015.
74. Jin-Keun Choi, Georges L. Chahine, Relationship between material pitting and cavitation field impulsive pressures, Wear 352-353 (2016) 42-53.
75. A. Thiruvengadam, On the selection of modeling materials to scale long term erosion behaviour of prototype systems, Report no, 71-1, The Catholic University of America, Jan. 1971.
76. N.S.G Rao and A. Thiruvengadam, Prediction of cavitation damage, Trans Am. Soc. Civ. Engrs., part 1, 127 (1962), 309-334.
77. A. Thiruvengadam, A Unified Theory of Cavitation Damage, ASME J. Basic Eng., 85 (1963), 365–373.
78. A. Thiruvengadam and Sophia Waring, Mechanical properties of metals and their cavitation damage resistance, Journal of Ship Research, May 1966, pp. 1-9.
79. J.M Hobbs, Experience with a 20 kc/s cavitation erosion test, symposium on erosion by cavitation or impingement, ASTM STP 408, Am. Soc. Testing Materials, Philadelphia, Pa., 1967, 159-185.
80. J.W Tichler, J.R Vanden Elsen, A.W.J de Gee, Resistance against cavitation erosion of 14 chromium steels, paper no. 69-Lub-19, Jour. Lubication technology, Trans. ASME, 1969.
81. B.C Syamala Rao, N.S.L Rao and K. Seetharamiah, Cavitation erosion studies with venturi and rotating disk in water, Paper no. 69-WA/FE 3, Jour. Basic Engineering, Trans ASME, 1969

82. F.J Heyman, Toward quantitative prediction of liquid impact erosion damage, Proc. symposium on characterization and determination of erosion resistance, ASTM, 1970.
83. Shuji Hattori and Ryohei Ishikura, Revision of cavitation erosion database and analysis of stainless steel data, Wear 268 (2010) 109-116.
84. Janusz Steller, Alicja Krella, On fractional approach to assessment of material resistance to cavitation, Wear 263 (2007), 402-411.
85. Janusz Steller, Alicja Krella, Waldemar Janicki, Towards quantitative assessment of material resistance to cavitation erosion, Wear 258 (2005) 604-613.
86. P. Veerabhadra Rao and Stanley G. Young, Universal approach to analysis of cavitation and liquid- impingement erosion data, NASA Technical paper 2061, 1982
87. P. Veerabhadra Rao and and Donald H. Buckley, Predictive capability of long-term cavitation and liquid impingement erosion models, Wear, 94 (1984) 259-274
88. R.H Richman and W.P McNaughton, Correlation of cavitation erosion behaviour with mechanical properties of metals, Wear, 140 (1990) 63-82.
89. H.G Feller and Y. Kharrazi, Cavitation erosion of metals and alloys, Wear, 93 (1984) 249-260.
90. F.C Campbell (ed.), Elements of metallurgy and engineering alloys, ASM International, Materials Park, Ohio, USA.
91. W. Bedkowski, G. Gasiak, A. Lichtarowicz, E. Macha, Correlation between cavitation erosion and random fatigue properties of selected steels, ECF-11, Mechanisms and mechanics of damage and failure : Proceedings of the 11th biennial European conference on fracture - ECF 11, Poitiers-Futuroscope, France, 3-6 September 1996, pp 1325-1330.

92. A. Karimi and W.R Leo, Phenomenological model for cavitation erosion rate computation, Materials Science and Engineering, 95 (1987), pp. 1-14.

93. N. Berchiche, J.P Franc, J.M Michel, A cavitation erosion model for ductile materials, Journal of fluids engineering, September 2002, vol. 124, pp. 601-606.

94. Y. Meged, Modelling of the initial stage in vibratory cavitation erosion tests by use of a Weibull distribution, Wear 253 (2002), 914-923

95. Arvind Jayaprakash, Jin-Keun Choi, Georges L. Chahine, Farrel Martin, Martin Donnelly, Jean-Pierre Fanc and Ayat Karimi, Scaling study of cavitation pitting from cavitating jets and ultasonic horns, Wear 296 (2012) 629-629

96. M. Szkodo, Mathematical description and evaluation of cavitation erosion resistance of materials, Journal of materials processing technology 164-165(2005) 1631-1636

97. Shuji Hattori, Kohei Maeda, Logistic curve model of cavitation erosion progress in metallic materials, Wear 268 (2010) 855-862

98. F.G Hammitt, Pump and other component cavitation comparisons between alkali liquid metals and water, Report no. UMICH-01357-34-T, Dec. 1973

99. Stanley G Young and John C. Freche, A review of NASA research to determine the resistance of materials to cavitation damage in liquid metal environments, Report no. NASA TM X-52956, 1971.

100. Stanley G. Young and James R. Johnston, Effect of cover gas pressures on accelerated cavitation damage in sodium, NASA technical note no. TN D-4235, Nov. 1967.

101. T.G. Leighton, The Acoustic Bubble, Academic press, 1974.

102. Jean Pierre Franc and Jean Marie Michel, Fundamentals of Cavitation, Kluwer Academic Publishers, 2004

103. V.A Akulichev, Pulsations of cavitation voids in High Intensity Ultrasonic Fields edited by L.D Rozenberg, Springer science + Business Media, 1971.

104. K. Vokurka, Comparison of Rayleigh's, Herring's and Gilmore's model of gas bubbles, Acustica, vol.59 (1986), pp 214-219.

105. Rana A. Fine and Frank J. Millero, Compressibility of water as a function of temperature and pressure, J. Chem. Phys. 59, 5529 (1973), doi: 10.1063/1.1679903.

106. Thermodynamic and transport properties of sodium liquid and vapor, ANL/RE-95/2.

107. J.Ross Macdonald, Some simple isothermal equations of state, Review of modern physics, vol. 38, no. 4, Oct 1966.

108. Chemical analysis report : CG no. 0511510a on Analysis of stainless steel samples dated 18th Feb. 2011, Chemical Analysis Group, IGCAR.

109. Material properties for design, Report no. PFBR/01000/DN/1000, Indira Gandhi Centre for Atomic Research (IGCAR).

110. Properties of welded stellite, document no. ID2-8000-3700, R-2, Yamatake Corporation, April 1999.

111. http://www.matweb.com/search/datasheet.aspx?matguid=3813de1a620d40cba0598409f9fc771e&ckck=1

112. Report nos. Met/lab/03/105/14 dated 11/02/2014 and Met/lab/04/106/14 dated 11/02/2014.

113. Welding Procedure Specification, no. OM/IGCAR/PISTON/WPS-03 dated 1/6/2009.

114. Chemical composition certificate from Service Central D'Analyse, Centre National de Recherche Scientifique dated 02/07/2009 and Laboratoire De Controle, Metaux Speciaux dated 06/07/2009.

115. Stephanie Bell, A beginners's guide to uncertainty of measurement, Measurement good practice guide no. 11 (issue 2), ISSN 1368-6550, National Physical Laboratory, UK.

116. Yukang Zhou and F.G Hammitt, Cavitation erosion incubation period, Wear, 86 (1983) 299-313.

117. Stanley G. Young and James R. Johnston, Effect of temperature and pressure on cavitation damage to a cobalt base alloy in sodium, NASA Technical Note no. NASA TN D-5273, (June 1969).

118. F. Ronald Young, Cavitation, Imperial College Press, 2015

119. S.M Ahmed, K. Hokkirigawa, R. Oba, Fatigue failure of SUS 304 caused by vibratory cavitation erosion, Wear 177 (1994) 129-137.

120. B.V Cockeram, Fracture toughness testing and toughening mechanisms of some commercial cobalt-free hardfacing alloys, WAPD-T-3177, Bettis Atomic power Laboratory, USDOE contract no. DE-AC11-93PN38195.

121. Winston O. Soboyejo, T.S. Srivatsan, Advanced Structural Materials: Properties, Design Optimization, and Applications, CRC Press, 2006.

122. J.R Davis (ed.), ASM speciality handbook, Nickel, Cobalt, and their alloys, ASM International, Materials Park, OH 44073.

123. Kim, Jun Ki, Ahn, Sam Yoel; Kim, Seon Jin; Oh, Young Kun; Lee, D. H., Cavitation erosion behavior of Fe and Ni base hardfacing alloys for replacing co-base stellite, Journal of the Korean Institute of Metals and Materials, 36(9) 1998, pp. 1391-1395.

124. K.C Antony, Wear resistant cobalt base alloys, Journal of metals, pp. 52-60, Feb. 1983.

125. M.S Plesset, Temperature effects in cavitation damage, Trans. ASME, Journal of basic engineering, Sept. 1972, pp. 560-566.

126. C.R Sohar, A. Betzwar-Kotas, C. Gierl, B. Weiss, H. Danninger, Gigacycle fatigue behavior of a high chromium alloyed cold work tool steel, International Journal of Fatigue 30 (2008) 1137-1149.

127. Element reference, ANSYS release 17.1 documentation

APPENDIX 1

ANALYSIS OF HORN

APPENDIX 1 - ANALYSIS OF HORN

This appendix discusses the analysis of the ultrasonic horn to determine (i) the longitudinal natural frequency of the horn, and (ii) to understand the variation of displacement and stress along the length of the horn

A 1.1 Horn Geometry

The stepped horn used for the experiment is shown in Fig. A1.1. The material of the horn is high carbon steel HCHC AISI D2. The maximum dimension of the top of the horn is 24.8 mm. This end is fixed to the booster of the ultrasonic machine by means of internal threads (1/2" * 20 UNF). The major portion of the horn is of circular cross section of diameter 15.8 mm. The specimen to be tested is threaded to the bottom end of the horn which is provided with internal threads (M10 * 1.25). A circular disc of 40 mm diameter is provided at a distance of 189.5 mm from the top of the horn. During operation this disc is pressed against O ring seal on the top of the cavitation vessel and thus seals the sodium in the vessel from the atmosphere. In order to ensure effective sealing and stress free operation of the horn the disc is located at a nodal point.

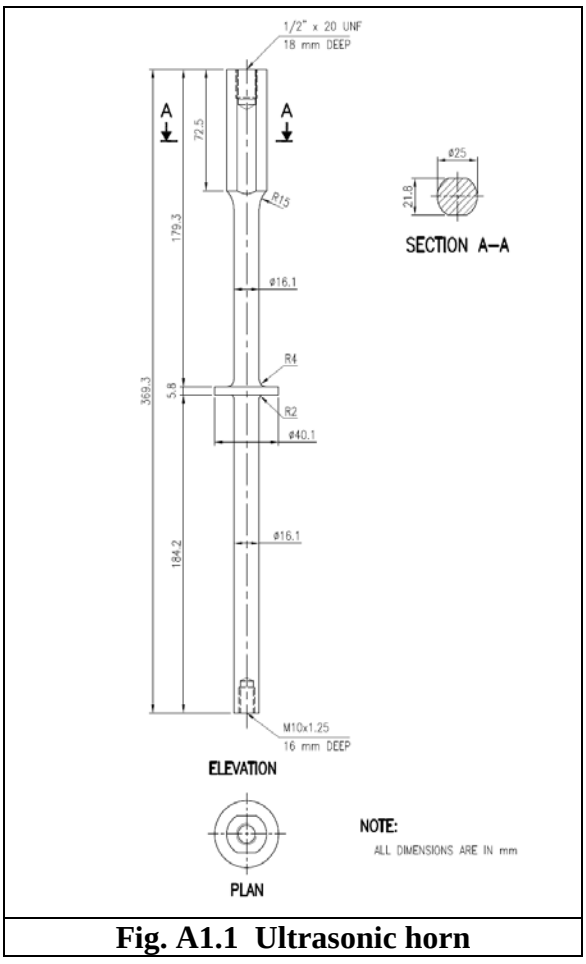

Fig. A1.1 Ultrasonic horn

The horn was analysed for stress and deflection along its length during operation at the driving frequency of 20 kHz.

This section discusses the modeling and analysis of the horn.

A 1.2 Material property

The horn material, HCHC, AISI-D2 tool steel is assumed to be isotropic in nature. Properties of the material are : Density, $\rho = 7800 kg/m^3$, modulus of elasticity, $E = 2\times10^{11}$ N/m^2, endurance strength = 580 MPa at 10^{10} cycles [126].

A 1.3 FEM Model

The horn is modeled in ANSYS using 2 noded 3D beam element (BEAM188) which has six degrees of freedom at each node. These include translations in the x, y, and z directions and rotations about the x, y, and z directions. This element is well-suited for linear, large rotation, and/or large strain nonlinear applications also [127]. The horn along with the specimen of 6 mm thickness is modelled as an integral unit. The accuracy of the model is dependent on the element type, degree of discretization and the fidelity of the boundary conditions. The number of elements was optimized to be 210 based on convergence test.

A 1.4 Boundary conditions

The top of the horn is fixed to the booster of the ultrasonic device and energized at 20 kHz in the longitudinal direction. A parametric study was done for different values of the displacement (zero to peak) at the booster tip (i.e horn top)

Hence the following boundary conditions are used :

At top of horn : u_z = 5.5 μm, 9.5 μm, 10 μm and 11 μm (zero to peak displacement)

$$u_x = u_y = 0$$

The damping coefficient is taken as 2%.

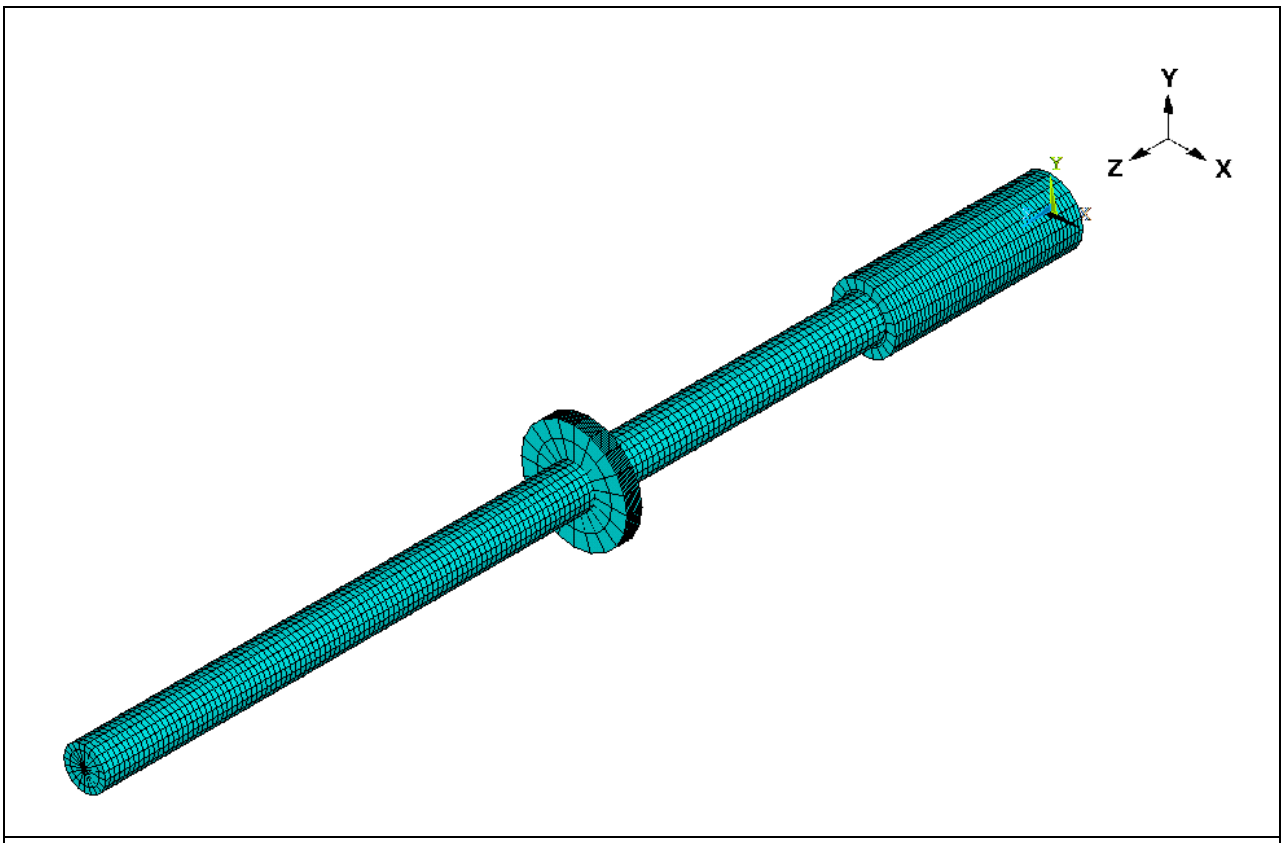

Fig. A 1.2 Model of horn

A 1.5 Analysis

The first step is to find out the longitudinal natural frequency of the horn that is closest to the driving frequency of 20 kHz. To reduce computational effort mode extraction is carried out in the frequency range 19 – 21 kHz using Block Lanchoz option. The next step is to do harmonic analysis to determine the displacement and stress along the length of the horn.

A 1.6 Results

A 1.6.1 Natural Frequency

The natural frequency of the horn closest to the driving frequency is 20713 Hz.

A 1.6.2 Nodal Displacement

The displacement and principal stress in longitudinal direction, calculated at 20.5 kHz, are given in Table A1.1 below. The applied frequency of the ultrasonic generator is 20 $\pm$ 0.5 kHz. Hence the frequency closest to the natural frequency of the horn is used for the analysis.

Table A1.1 – Displacement and stress along the length of horn

Displacement at top of horn (zero to peak), μm	**Displacement at bottom of horn (zero to peak), μm**	**Longitudinal stress, MPa**
5.5	13.35	68
9.5	23.07	118
10	24.28	124
11	26.71	136

It is seen that with a driving displacement of 11 μm at the top of the horn, the displacement at the bottom is marginally above 50 μm. The maximum stress in this case, along the centre line of the horn, occurs at the junction of the uniform diameter of 16 mm and the disc of 40 mm diameter. This is because of the large stress concentration at this location.

It may also be seen from Fig. A1.3 that the disc of 40 mm diameter is located at a nodal point.

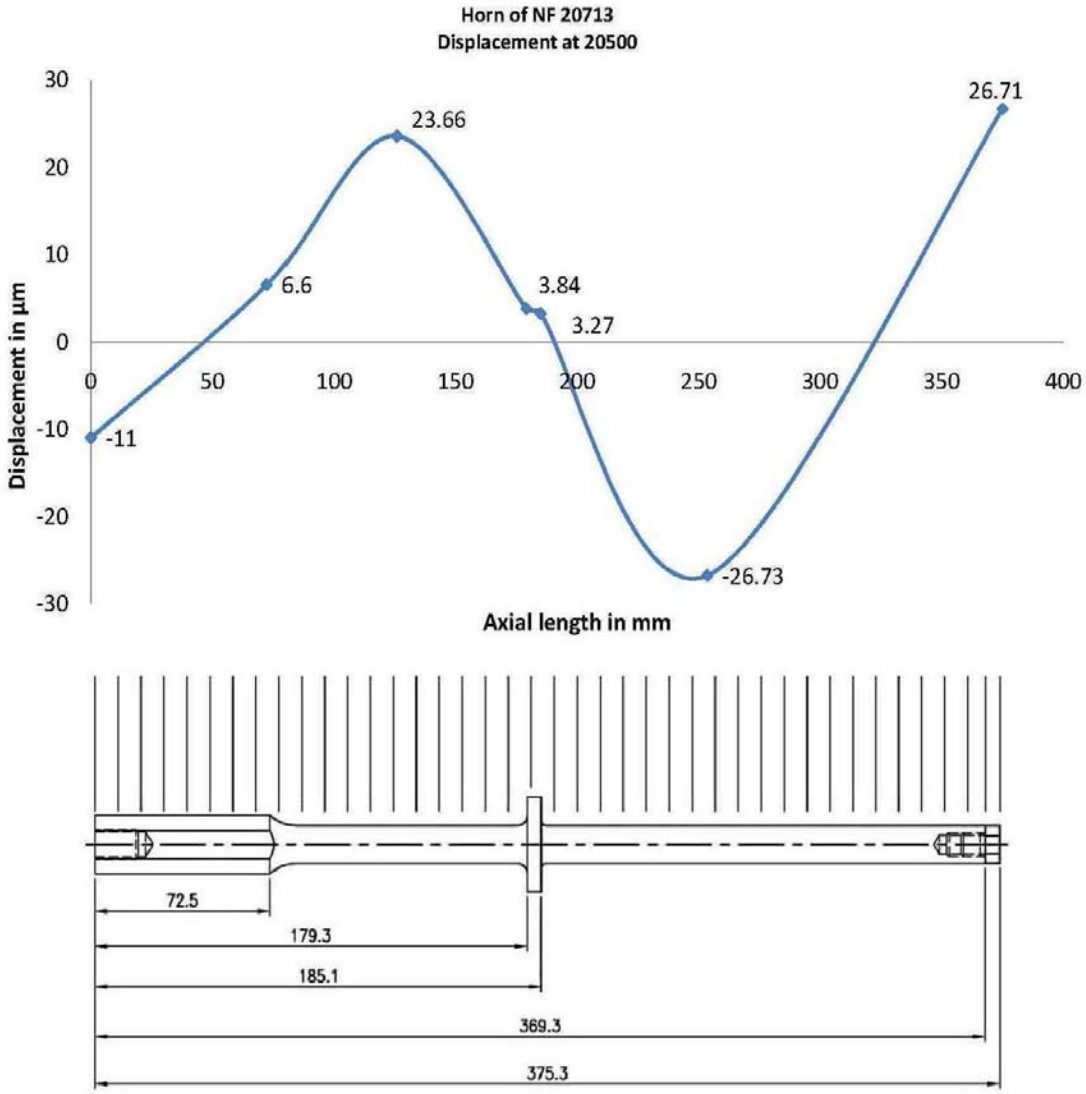

Fig. A1.3 Displacement along the length of the horn

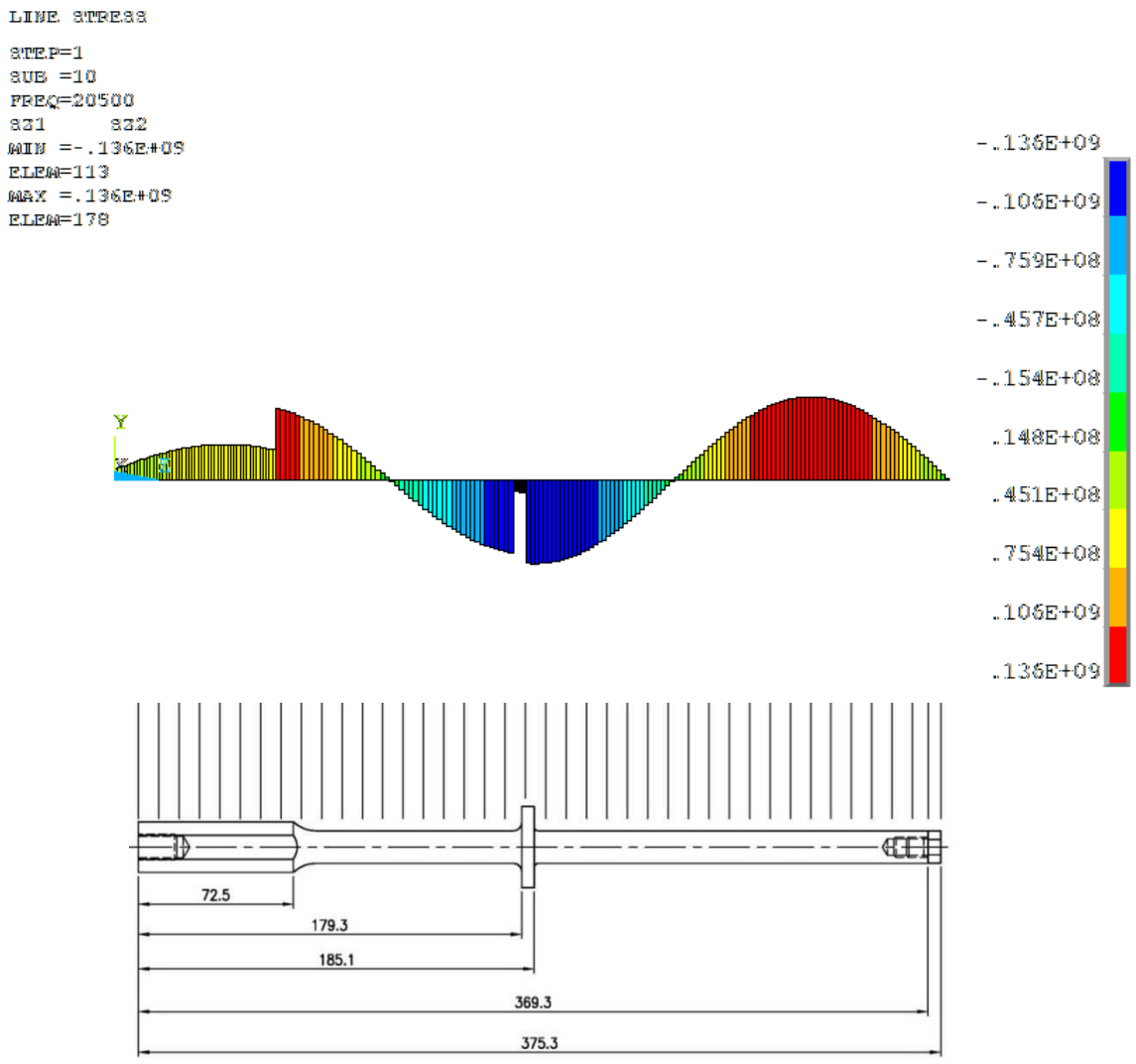

Fig. A1.4 Stress along the length of the horn

APPENDIX 2

RESULTS OF WEIGHT LOSS MEASUREMENTS FROM CAVITATION EROSION TESTING

APPENDIX 2 – RESULTS OF WEIGHT LOSS MEASUREMENTS FROM CAVITATION EROSION TESTING

Material : SS 316L

Table A2.1 – SP3 (SS316L) tested at 200 ºC

Sl. No.	Specimen no. / Test Temperature ºC	Time S	Cumulative Time		Weight g	Cumulative weight loss, g	Cumulative weight loss, g/hr
	SP3 / 200		s	h			
1		0	0	0	14.1549	0	-
2		302	302	0.08389	14.1536	0.0013	0.01550
3		903	1205	0.334722	14.1402	0.0147	0.04392
4		601	1806	0.50167	14.1292	0.0257	0.05123
5		1103	2909	0.80806	14.1106	0.0443	0.05482
6		1796	4705	1.30694	14.0806	0.0743	0.05685
7		3768	8473	2.35361	14.0244	0.1305	0.05545

Table A2.2 – SP4 (SS316L) tested at 200 ºC

Sl. No.	Specimen no. / Test Temperature ºC	Time s	Cumulative Time		Weight g	Cumulative weight loss, g	Cumulative weight loss, g/hr
	SP4 / 200		s	h			
1		0	0	0	12.8577	0	-
2		304	304	0.08444	12.8565	0.0012	0.01421
3		609	913	0.25361	12.8480	0.0097	0.03825
4		3608	4521	1.25583	12.8011	0.0566	0.04507

Table A2.3 – SP5 (SS316L) tested at 200 ºC

Sl. No.	Specimen no. / Test Temperature ºC	Time s	Cumulative Time		Weight g	Cumulative weight loss, g	Cumulative weight loss, g/hr
	SP5 / 200		**s**	**h**			
1		0	0	0	13.2563	0	-
2		314	314	0.08722	13.255	0.0013	0.01490
3		1355	1669	0.46361	13.2337	0.0226	0.04874
4		3718	5387	1.49639	13.1772	0.0791	0.05286
5		3604	8991	2.4975	13.1315	0.1248	0.04997

Table A2.4 – A6 (SS316L) tested at 250 ºC

Sl. No.	Specimen no. / Test Temperature ºC	Time s	Cumulative Time		Weight g	Cumulative weight loss, g	Cumulative weight loss, g/hr
	A6 / 250		**s**	**h**			
1		0	0	0	12.6665	0	-
2		520	520	0.14444	12.6601	0.0064	0.04431
3		1931	2451	0.68083	12.6242	0.0423	0.06213
4		3716	6167	1.71306	12.5564	0.1101	0.06427

Table A2.5 – A15 (SS316L) tested at 250 ºC

Sl. No.	Specimen no. / Test Temperature ºC	Time s	Cumulative Time		Weight g	Cumulative weight loss, g	Cumulative weight loss, g/hr
	A15 / 250		**s**	**h**			
1		0	0	0	13.9151	0	-
2		1822	1822	0.50611	13.8908	0.0243	0.04801
3		1551	3373	0.93694	13.8709	0.0442	0.04717

Table A2.6 – A10 (SS316L) tested at 300 ºC

Sl. No.	Specimen no. / Test Temperature ºC	Time	Cumulative Time		Weight g	Cumulative weight loss, g	Cumulative weight loss, g/hr
	A10 / 300		**s**	**h**			
1		0	0	0	14.0176	0	-
2		1203	1203	0.33417	14.0096	0.008	0.023940
3		1613	2816	0.78222	13.9798	0.0378	0.048324
4		3621	6437	1.78806	13.9101	0.1075	0.060121

Table A2.7 – A12 (SS316L) tested at 300 ºC

Sl. No.	Specimen no. / Test Temperature ºC	Time s	Cumulative Time		Weight g	Cumulative weight loss, g	Cumulative weight loss, g/hr
	A12 / 300		**s**	**h**			
1		0	0	0	13.8367	0	-
2		1820	1820	0.50556	13.7957	0.041	0.081098

Table A2.8 – A14 (SS316L) tested at 300 ºC

Sl. No.	Specimen no. / Test Temperature ºC	Time s	Cumulative Time		Weight g	Cumulative weight loss, g	Cumulative weight loss, g/hr
	A14 / 300		**s**	**h**			
1		0	0	0	13.9769	0	-
2		1874	1874	0.52056	13.9472	0.0297	0.057054
3		2804	4678	1.29944	13.8815	0.0954	0.073416

Table A2.9 – A22 (SS316L) tested at 400 ºC

Sl. No.	Specimen no. / Test Temperature ºC	Time s	Cumulative Time		Weight g	Cumulative weight loss, g	Cumulative weight loss, g/hr
	A22 / 400		s	h			
1		0	0	0	13.7917	0	-
2		3655	3655	1.01528	13.7810	0.0107	0.010539
3		3607	7262	2.01722	13.7720	0.0197	0.009766
4		2718	9980	2.77222	13.7656	0.0261	0.009415
5		2730	12710	3.53056	13.7598	0.0319	0.009035
6		3612	16322	4.53389	13.7527	0.039	0.008602

Material : Colmonoy5

Table A2.10 – SP6 (Colmonoy 5 hardfacing)) tested at 200 ºC

Sl. No.	Specimen no. / Test Temperature ºC	Time s	Cumulative Time		Weight, g	Cumulative weight loss, gm	Cumulative weight loss rate, g/h
	SP6 / 200		s	h			
1		0	0	0	14.0431	0	
2		317	317	0.08806	14.0423	0.0008	0.009085174
3		903	1220	0.33889	14.0401	0.003	0.008852459
4		1829	3049	0.84694	14.0298	0.0133	0.015703509
5		2218	5267	1.46306	14.0178	0.0253	0.017292576

Table A2.11 – C8 (Colmonoy 5 hardfacing)) tested at 200 ºC

Sl. No.	Specimen no. / Test Temperature ºC	Time s	Cumulative Time		Weight, g	Cumulative weight loss, gm	Cumulative weight loss rate, g/h
	C8 / 200		s	h			
1		0	0	0	13.4791	0	
2		2538	2538	0.705	13.4648	0.0143	0.020283688
3		3719	6257	1.7381	13.4435	0.0356	0.020482659

Table A2.12 – C3 (Colmonoy 5 hardfacing)) tested at 250 ºC

Sl. No.	Specimen no. / Test Temperature ºC	Time s	Cumulative Time		Weight, g	Cumulative weight loss, gm	Cumulative weight loss rate, g/h
	C3 / 250		s	h			
1		0	0	0	12.8714	0	
2		366	366	0.1017	12.8672	0.0042	0.041311475
3		2109	2475	0.6875	12.8582	0.0132	0.0192

Table A2.13 – C2 (Colmonoy 5 hardfacing) tested at 250 ºC

Sl. No.	Specimen no. / Test Temperature ºC	Time s	Cumulative Time		Weight, g	Cumulative weight loss, gm	Cumulative weight loss rate, g/h
	C2 / 250		s	h			
1		0	0	0	13.4214	0	
2		936	936	0.26	13.4191	0.0023	0.008846154
3		1529	2465	0.6847	13.4092	0.0122	0.017817444
4		3630	6095	1.6931	13.3886	0.0328	0.019373257

Table A2.14 – C10 (Colmonoy 5 hardfacing) tested at 250 ºC

Sl. No.	Specimen no. / Test Temperature ºC	Time s	Cumulative Time		Weight, g	Cumulative weight loss, gm	Cumulative weight loss rate, g/h
	C10 / 250		s	h			
1		0	0	0	13.5785	0	
2		1824	1824	0.5067	13.5658	0.0127	0.025065789

Table A2.15 – C7 (Colmonoy 5 hardfacing) tested at 300 ºC

Sl. No.	Specimen no. / Test Temperature ºC	Time s	Cumulative Time		Weight, g	Cumulative weight loss, gm	Cumulative weight loss rate, g/h
	C7 / 300		s	h			
1		0	0	0	13.5328	0	
2		1200	1200	0.3333	13.5295	0.0033	0.0099
3		1592	2792	0.7756	13.5224	0.0104	0.013409742
4		3610	6402	1.7783	13.5034	0.0294	0.016532334

Table A2.16 – C1 (Colmonoy 5 hardfacing) tested at 300 ºC

Sl. No.	Specimen no. / Test Temperature ºC	Time s	Cumulative Time		Weight, g	Cumulative weight loss, gm	Cumulative weight loss rate, g/h
	C1 / 300		s	h			
1		0	0	0	13.5462	0	
2		1832	1832	0.5089	13.5423	0.0039	0.007663755
3		2786	4618	1.2828	13.535	0.0112	0.008731052

Table A2.17 – C12 (Colmonoy 5 hardfacing) tested at 400 ºC

Sl. No.	Specimen no. / Test Temperature ºC	Time s	Cumulative Time		Weight, g	Cumulative weight loss, gm	Cumulative weight loss rate, g/h
	C12 / 400		s	h			
1		0	0	0	13.5645	0	
2		471	471	0.1308	13.5644	0.0001	0.000764331
3		3222	3693	1.0258	13.5633	0.0012	0.001169781
4		3608	7301	2.0281	13.5603	0.0042	0.002070949
5		2738	10039	2.7886	13.5586	0.0059	0.002115749
6		3608	13647	3.7908	13.5562	0.0083	0.002189492
7		3621	17268	4.7967	13.5541	0.0104	0.002168172

Material : Stellite6

Table A2.18 – S1 (Stellite6 hardfacing) tested at 200 ºC

Sl. No.	Specimen no. / Test Temperature ºC	Time s	Cumulative Time		Weight, g	Cumulative weight loss, gm	Cumulative weight loss rate, g/h
	S1 / 200		s	h			
1		0	0	0	14.2844	0	
2		443	443	0.1231	14.2826	0.0018	0.01462754
3		976	1419	0.3942	14.2821	0.0023	0.005835095
4		1888	3307	0.9186	14.2797	0.0047	0.00511642
5		3737	7044	1.9567	14.2678	0.0166	0.008483816

Table A2.19 – S5 (Stellite6 hardfacing) tested at 200 ºC

Sl. No.	Specimen no. / Test Temperature ºC	Time s	Cumulative Time		Weight, g	Cumulative weight loss, gm	Cumulative weight loss rate, g/h
	S5 / 200		s	h			
1		0	0	0	14.0841	0	
2		3733	3733	1.0369	14.0797	0.0044	0.004243236
3		3646	7379	2.0497	14.0728	0.0113	0.005512942

Table A2.20 – S3 (Stellite6 hardfacing) tested at 250 ºC

Sl. No.	Specimen no. / Test Temperature ºC	Time s	Cumulative Time		Weight, g	Cumulative weight loss, gm	Cumulative weight loss rate, g/h
	S3 / 250		s	h			
1		0	0	0	14.1987	0	
2		1529	1529	0.4247	14.1969	0.0018	0.004238064
3		1274	2803	0.7786	14.196	0.0027	0.003467713

Table A2.21 – S2 (Stellite6 hardfacing) tested at 250 ºC

Sl. No.	Specimen no. / Test Temperature ºC	Time s	Cumulative Time		Weight, g	Cumulative weight loss, gm	Cumulative weight loss rate, g/h
	S2 / 250		s	h			
1		0	0	0	14.1167	0	
2		451	451	0.1253	14.115	0.0017	0.013569845
3		2126	2577	0.7158	14.1143	0.0024	0.003352736

Table A2.22 – S23 (Stellite6 hardfacing) tested at 300 ºC

Sl. No.	Specimen no. / Test Temperature ºC	Time s	Cumulative Time		Weight, g	Cumulative weight loss, gm	Cumulative weight loss rate, g/h
	S23 / 300		s	h			
1		0	0	0	14.1598	0	0
2		1822	1822	0.5061	14.158	0.0018	0.003556531

Table A2.23 – S17 (Stellite6 hardfacing) tested at 400 ºC

Sl. No.	Specimen no. / Test Temperature ºC	Time s	Cumulative Time		Weight, g	Cumulative weight loss, gm	Cumulative weight loss rate, g/h
	S17 / 400		s	h			
1		0	0	0	14.1582	0	
2		3636	3636	1.01	14.1571	0.0011	0.001089109
3		3605	7241	2.0114	14.1569	0.0013	0.00064632
4		2721	9962	2.7672	14.1565	0.0017	0.000614334
5		3611	13573	3.7703	14.1565	0.0017	0.000450895